공학박사학위논문

Lithium Storage Mechanisms and Performance Improvements of Vanadium-based Metal Oxide Electrodes for Lithium-ion Batteries

리튬 이온 전지용 바나듐계 금속 산화물 전극의

리튬 저장 메커니즘 및 성능 향상

2017 년 2 월

서울대학교 대학원

화학생물공학부

이 정 범

PREFACE

This dissertation is submitted for the degree of Doctor of Philosophy in Engineering at Seoul National University. The research described herein was conducted under supervision of Professor Seung M. Oh in the Department of Chemical and Biological Engineering, Seoul National University, between March 2011 and December 2016.

This work is to the best of my knowledge original, except where the citations are made to previous works. Neither this nor any substantially similar dissertation has been or is being submitted for any other degree or other qualification at any other university.

Part of this work has been presented in the following publications:

Jeong Beom Lee, Oh B. Chae, Seulki Chae, Ji Heon Ryu, and Seung M. Oh*, Amorphous Vanadium Titanates as a Negative Electrode for Lithium-ion Batteries, *Journal of Electrochemical Science and Technology*, **2016**, *7(4)*, 1–10.

Jeong Beom Lee, Janghyuk Moon, Oh B. Chae, Jae Gil Lee, Ji Heon Ryu, Maenghyo Cho, Kyeongjae Cho, and Seung M. Oh*, Unusual Conversion-type Lithiation in $LiVO_3$ Electrode for Lithium-Ion Batteries, *Chemistry of Materials*, **2016**, *28*, 5314–5320.

Jeong Beom Lee, Seulki Chae, Hyejeong Jeong, Hong Seo Hwang, Jiwon Jung, Ji Heon Ryu, and Seung M. Oh*, Electrochemical conversion of CuV_2O_6 into metallic Cu and $LiVO_3$ with highly reversible lithium storage, *submitted*.

ABSTRACT

Lithium Storage Mechanisms and Performance Improvements of Vanadium-based Metal Oxide Electrodes for Lithium-ion Batteries

Jeong Beom Lee

Department of Chemical and Biological Engineering

Seoul National University

Lithium-ion batteries (LIBs) are the most important energy storage devices in modern society and they are being utilized in various applications from portable devices to large scale energy storage for vehicles and grids. In order to be qualified in these applications, LIBs should have higher energy density and power capability. To further increase the performance of LIBs, transition metal oxides have been studied as alternatives of graphite which has been conventionally used as a negative electrode material. Lithium storage in the transition metal oxides can be divided into two types; insertion and conversion reaction. In the insertion-type metal oxides, Li^+ ions are stored in the interstitial sites during charge (lithiation) and reversibly released during discharge (delithiation). Because this insertion-type of Li^+ storage does not accompany large structural distortion, it is highly stable and thus suitable for batteries with long cycle life. However, its reversible capacity is rather limited due to the finite amount of Li^+ storage sites in the metal oxide. On the other hand, there are no limited sites for Li^+ ions to reside in the conversion-type metal oxides. Because of this reason, these metal oxides show much larger Li^+ storage capacity. Upon lithiation, metal and oxygen bonds are broken and Li^+ and oxygen form new bonds

to generate lithium oxide (Li_2O) and nano-sized metallic compounds. However, they generally have a large hysteresis during cycles and relatively high redox potentials, which limit the increment of energy density.

In this work, the shortcomings of metal oxides stated above are improved with vanadium-based metal oxides. First, amorphous vanadium titanate (*a*VTO) is examined to enlarge the specific capacity of insertion-type metal oxides. *a*VTO are synthesized in nano-sized particles (< 100 nm) flocculated to form secondary particles. The V^{5+} ions in *a*VTO are found to occupy tetrahedral sites, whereas the Ti^{4+} ions show five-fold coordination. Both are uniformly dispersed at the atomic scale in the amorphous oxide matrix, which has abundant structural defects. The first reversible capacity of *a*VTO electrode (295 mA h g^{-1}) is larger than that observed with the physically mixed electrode (1:2 aV_2O_5 | $aTiO_2$, 245 mA h g^{-1}). The discrepancy seems to be due to the homogeneous mixing of V^{5+} and Ti^{4+} ions in atomic scale, which induces four-coordinated V^{5+} ions in *a*VTO. This unique structure affects the chemical potential of Li^+ storage sites by modifying either electronic band structure or generating more structural defects to serve as Li^+ storage sites. Li/*a*VTO cells show a large irreversible capacity in the first cycle. Prepared under nitrogen (*a*VTO-N), the population of surface hydroxyl groups is greatly reduced. These groups irreversibly produce highly resistive inorganic compounds (LiOH and Li_2O) leading to increased irreversible capacity and electrode resistance. As a result, the material prepared under nitrogen shows higher Coulombic efficiency and rate capability. Secondly, lithium metavanadate ($LiVO_3$) is lithiated by a conversion reaction near 0.0 V, which is much lower potential for conversion-type metal oxides. The electrochemical, spectroscopic studies and first-principle calculations performed on the lithiation mechanism of $LiVO_3$ consistently propose that a two-phase insertion-type lithiation proceeds in the early stage of lithiation; $LiVO_3$ transforms into a rock-salt structured Li_2VO_3. The

continuing single-phase Li^+ insertion into the tetrahedral sites in the above rock-salt Li_2VO_3 produces a more Li-rich phase ($Li_{2.5}VO_3$), which is highly distorted because of the unfavorable Li^+ insertion into the tetrahedral sites to be vulnerable to lattice break-down. Hence, a two-phase (nucleation/growth type) conversion reaction is followed along with a structural disintegration; the $Li_{2.5}VO_3$ phase decomposes into metallic vanadium and Li_2O. To determine the factors facilitating the conversion reaction of $LiVO_3$, electrochemical and theoretical analysis are performed and the results of which are then compared to those observed with V_2O_5, which is not lithiated by the conversion reaction at 25°C. The results show that the quasi-equilibrium potential for the conversion reaction is more positive for $LiVO_3$ (thermodynamically more feasible). Also, the conversion reaction is kinetically more facilitated for $LiVO_3$ due to faster solid-state diffusion of mobile ionic species during the two-phase growth stage of metallic vanadium and lithium oxide (Li_2O) in the conversion process., Furthermore, copper vanadate (CuV_2O_6), which generates Cu/$LiVO_3$ nanocomposite during the first cycle, is demonstrated as a negative electrode material that can further enhance the cycle life of $LiVO_3$ electrode. The Li/CuV_2O_6 cell shows a high cycle retention, which seems to due to the beneficial roles offered by the metallic copper, which plays as a buffer against the volume change of electrode component and as an electron conducting channel.

Keywords: Lithium-ion batteries, Negative electrodes, Transition metal oxides, Amorphous vanadium titanate, Lithium metavanadate, Copper metavanadate

Student number: 2011-22929

TABLE OF CONTENTS

LIST OF FIGURES

LIST OF TABLES

CHAPTER 1. INTRODUCTION

Modern society is built on fossil fuels. As can be seen from the unstable supply of resources and the global climate change, it is obvious that this energy production and consumption system based on the fossil fuels is no longer sustainable.[1,2] Many organizations over the world have warned that if this energy system continues, serious environmental damages may occur in the near future. Therefore, it is the time for us to move forward to the environmental friendly energy system. In order to do so, many researchers and engineers endeavor to develop advanced technologies to make renewable sources such as solar and wind power, which have less effects on the environment, more efficient for practical use. The ratio of energy produced from renewable sources is gradually increasing in the energy portfolio worldwide with their efforts.

In this forthcoming energy paradigm, the most important and frequently-used form of energy will be electricity. Electricity is the most appropriate form of energy for modern and future society because it is easy to distribute, access, control, and combine with information technologies (IT). Furthermore, the energy collected from the solar and wind power are transformed mostly into the electrical energy. However, because they are renewable but inconsistent, an installation of electric energy storage system is an inevitable choice for the stable supply of electricity generated from renewable sources. Besides, the electric energy storage system is necessary to utilize the electric energy, which should be consumed at the same time it is generated, more efficiently.[3]

For these reasons, electric energy storage is increasingly important in the industry, from small electronic devices to large-scale applications including transportations, electricity generation, transmission, distribution and consumption. There are numerous types of energy storage systems, such as fly wheel, pumped hydro, and other systems.[3] Among others, to convert energy in the form of chemical energy in a device called a battery is the most effective way to store electricity in a compact volume and mass.[4]

Lithium-ion battery (LIB) has developed into the most preferred battery system for mobile devices since its debut in 1991.[5] All of this became possible thanks to the successful utilization of stable intercalation chemistry of Li^+ ions in both postive and negative electrodes. This reversible redox behavior, which is called rocking chair mechanism, could be attained from lithium cobalt oxide ($LiCoO_2$, LCO) and graphite, which react with Li^+ ions at 3.9 V and 0.1 V (*vs.* Li/Li^+), respectively.[6] Two electrode materials, which have a large gap of redox potentials in between, as well as electrolytes, which can endure these potentials, made it possible to fabricate batteries with superior energy density compared to other rechargeable batteries.[5]

Because of its high energy density, LIB has been and will be the most promising electrical energy storage device. However, it gets even more challenging as the applications of LIBs will be further diversified. Particularly, they are getting more importance in the automobile and electric power industry than ever before. Both non-governmental organizations (NGOs) and governments are pushing the industry with several regulations to produce cars with high fuel efficiency and low emission, hence the vehicles with internal combustion engine (ICE) are replaced by electric-powered ones such as hybrid and battery electric vehicles (xEVs). Since the inside volume of a car is limited, it is a natural consequence to select LIBs for its power source. Moreover, LIBs are taking an essential role in electric power industry as an energy storage system (ESS), especially in a smart

grid which aims to improve efficiency of energy infrastructure including power generation from renewable sources.

In order for this battery system to meet the requirements of highly demanding devices mentioned above, it is necessary to develop new electrode materials to push beyond the limits of conventional materials and have properties which exactly coincide with their end-use applications. Several intrinsic properties of graphite, the most popular negative electrode material, hinders the increment energy and power density of LIBs. One reason is its low specific capacity which is 372 mA h g^{-1}.[7] Moreover, the working potential of graphite is so close to that of Li metal that Li plating is highly probable under high-rate charging, which frequently leads to severe safety problems such as internal shortage by dendritic Li metal.[8]

To further enhance the performances of LIBs, transition metal oxides have been proposed as alternatives for negative electrode materials. The Li^+ storage mechanism in transition metal oxides can be divided into two types: insertion and conversion. In the insertion reaction, Li^+ ions are stored in the well-defined interstitial sites of crystalline structures or in the structural defects of the amorphous phase.[9–11] Because Li^+ can reside at sites which already exist in the structure, the original framework of the materials is maintained during the charge and discharge cycles. This process of insertion results in a low volumetric change and stable cycle life. In contrast to the insertion-type materials that have a fixed number of Li^+ storage sites, metal oxides which store Li^+ through the conversion-type reaction have benefits especially in their large specific capacity. There is no limitation in the number of Li^+ storage sites in conversion-type materials because the original framework of metal oxides is destroyed during lithiation. Simultaneously, co-injected electrons with Li^+ ions reduce transition metal ions into the metallic states, resulting in the cleavage of metal-oxygen bonds and the formation of metal nanoparticles

and lithium oxide (Li_2O, lithia) matrix.[12–14] Because of these reasons, the possibility of a conversion reaction, which is related to its redox potential, strongly depends on the transition metal ions.

This work consist of two parts and each part analyzes different metal oxides that contain vanadium ions as a major component. In Section 4.1, amorphous vanadium titanate (*a*VTO) is proposed as a novel negative electrode material which shows an increased specific capacity by insertion-type lithium storage in amorphous structure. The atomic structure and composition of the material are analyzed with spectroscopic techniques and has examined how it affects the electrochemical performance of *a*VTO. Moreover, the amount of surface hydroxyl groups, which are related to its Coulombic efficiency and rate performance, is reduced by manipulating atmospheric condition during precipitation. In Section 4.2, lithium metavanadate ($LiVO_3$) is examined as a negative electrode material that shows large specific capacity with a reversible conversion-type lithium storage. Note that there were no conversion reaction of vanadium oxides that has ever been reported. Lithium storage mechanism of $LiVO_3$ are analyzed comprehensively by using electrochemical, spectroscopic techniques and *ab-initio* simulation and compared with V_2O_5 which does not undergo conversion reaction at ambient temperature. In addition, copper vanadate (CuV_2O_6), which is converted into nanocomposites of Cu and $LiVO_3$ during cycling, is introduced to further improve the electrochemical performance of $LiVO_3$ electrodes.

CHAPTER 2. BACKGROUND

2.1. Overview on lithium-ion batteries (LIBs)

2.1.1. Basic principles and components of LIBs

Four major components of lithium-ion batteries are positive electrode, negative electrode, electrolyte and separator. During discharging process, oxidation occurs on the negative electrode and reduction occurs on the positive electrode. The generated charge carriers (Li^+ ions/electrons) upon the oxidation move from the negative electrode to the positive electrode. Li^+ ions transport through the electrolyte and electrons move through the external circuit and deliver electric energy to the equipment. Since the redox reactions on each electrodes are highly reversible, this battery system is rechargeable. Reverse reactions occur during charging process. The positive electrode is oxidized to release Li^+ ions to the electrolyte and electrons to the external circuit. At the same time, the negative electrode is reduced to uptake Li^+ ions from the electrolyte and electrons from the external circuit. The reaction that Li^+ ions repeatedly transfer between the positive and negative electrodes is called rocking-chair mechanism.[15] In general, charging process should be done prior to discharging because both electrodes are in discharged state when the cell is first assembled. On the aspect of negative electrode, it uptakes Li^+ ions during charging and releases Li^+ ions during discharging. Thus, in this dissertation, the term of lithiation

and delithiation will refer to charging (reduction) and discharging (oxidation) process, respectively.

Both electrodes consist of four components; active materials, conductive carbon additives, polymeric binder and current collectors. Active materials uptake/release Li^+ ions during charge and discharge, conductive carbon additive and current collector collect the electrons and transfer them from/to external circuit and the polymeric binder adheres all those components. Electrolytes conduct Li^+ ions between the two electrodes while separator insulates the electron transfer between them.

2.1.1.1. Positive electrode materials

Transition metal oxides or phosphates that contain Li^+ ions are generally utilized for the positive electrode. $LiCoO_2$, which has a layered structure, is one of the most frequently used positive electrode materials in the commercialized cells.[16] Lately, other metal ions such as nickel, manganese or aluminum are substituted to further enhance the various properties including specific capacity, stability and economic feasibility.[17,18] Spinel structured metal oxides, $LiMn_2O_4$ and $LiNi_{0.5}Mn_{1.5}O_4$, and olivine structured metal phosphates, $LiFePO_4$, are also developed as alternatives.[19–21]

2.1.1.2. Negative electrode materials

Graphite played an essential role in the commercialization of lithium-ion batteries. Before the development of the graphite, lithium metal was used as a negative electrode. Li metal has benefits in its low working potential and large specific capacity, however, dendritic Li plating and unstable surface film formation have made it difficult to be applied in commercial batteries.[6] Graphite offers stable Li^+ intercalation and de-intercala-

tion chemistry which enabled the successful application of rocking-chair mechanism described in the previous section. Recent progress on the negative electrode materials will be further reviewed in Section 2.2.

2.1.1.3. Electrolytes

Non-aqueous electrolyte solutions, or organic electrolyte, are employed in LIBs to fully utilize the wide potential range of the electrode materials. Electrolytes are so closely linked to the safety of the batteries that they should satisfy various requirements; high ionic conductivity, high chemical and electrochemical stability and wide range of operational temperature. Electrolyte solutions are formulated by dissolving appropriate amount of lithium salts in the mixture of organic solvents. Typically used lithium salt is lithium fluorophosphate ($LiPF_6$). The mixture of cyclic carbonates such as ethylene carbonate (EC) and propylene carbonate (PC) and linear carbonates such as dimethyl carbonate (DMC), diethyl carbonate (DEC) and ethylmethyl carbonate (EMC) are used as organic solvents.[22] Because the working potential of the negative electrode materials such as graphite exceeds the electrochemical stability window (ESW) of the electrolyte, the electrolyte is decomposed on the electrode to form thin film, which is called solid-electrolyte interphase (SEI).[23,24] The SEI significantly affect the cell performances especially in cycle life, safety and stability. To improve the various properties of SEI, additives such as vinylene carbonate (VC) and fluoroethylene carbonate (FEC) are dissolved in the electrolyte solution.[25,26]

2.1.1.4. Separators

Separators insulate the electron transfer between the positive and negative electrodes through the inside of the cell and thus play a critical role in the safety. When they fail to

block contact between the two electrodes, large amount of current flow inside the cell, which can lead to the thermal runaway. Separators are made of porous polymer films which are made of polypropylene (PP) or polyethylene (PE). In order to increase their mechanical and thermal stability, these films are stacked up and coated with electrochemically stable metal oxides such as alumina.[6]

2.1.2. Characteristics and general requirements of LIBs

2.1.2.1. Energy density and power density of LIBs

The energy density (E) of LIBs is the amount of energy that can be stored within unit volume and mass and obtained from the product of cell voltage (V_{cell}) and capacity (Q) as shown in Equation 2-1.[6] Therefore, it is necessary to construct a cell with high cell voltage and large capacity in order to increase the energy density of the battery.

$$E = V_{cell} \times Q \qquad \textbf{Equation 2-1}$$

Meanwhile, the cell voltage of LIBs is determined by the potential difference between the positive and negative electrodes as described in Equation 2-2.

$$V_{cell} = V_{positive} - V_{negative} \qquad \textbf{Equation 2-2}$$

The capacity is the total amount of charge delivered per unit volume or mass and expressed as the product of current (i) and time (t) (Equation 2-3).

$$Q = i \times t \qquad \textbf{Equation 2-3}$$

The power of LIBs is the amount of energy that can be delivered per unit time and expressed as the product of cell voltage (V_{cell}) and current (i) as shown in Equation 2-4.[6] Therefore, the faster the reaction rate inside, the more power can be derived from the cell.

$$P = i \times V_{cell}$$ **Equation 2-4**

General requirements of battery components regarding these characteristics can be described as follows: (i) Electrode materials with high capacity; In order to increase the energy density of the cell, electrode materials should have an ability to store large amount of Li^+ ions and electrons reversibly. (ii) Electrode materials with high conductivity; Electrode materials should have high conductivity for both Li^+ ions and electrons to facilitate faster redox reaction rate and thus have a high power capability. (iii) Highly Li^+ conductive electrolytes; (iv) High chemical and electrochemical stability during cycles.[6] Since the cell voltage of batteries is determined by Equation 2-2, it is better for the negative electrodes to have low reaction potential in addition to the general requirements of electrode materials for developing the cell with high energy density.

2.1.2.2. Efficiency

Efficiency of the cell can be divided into two categories; energy efficiency and Coulombic efficiency. Energy efficiency of the batteries is the ratio between the input energy during charge and output energy during discharge and thus it is mostly influenced by the polarization of potential upon charge and discharge, which is known as voltage hysteresis. However, Coulombic efficiency, which shows the reversibility of charge storage reactions, affects cycle life of the cell, since there are limited amount of charge carriers (Li^+ ions) in LIBs. In the same context, it is extremely important to maximize the Coulombic efficiency on the negative electrode. Irreversible reaction on the negative electrode are caused by various reasons mostly from reductive decomposition of electrolytes, phase transition of active materials or electrode degradation. In both cases, Li^+ ions are irreversibly consumed and cannot participate in charge storage afterwards and lead to capacity

fading. Furthermore, the irreversible reactions on negative electrodes trigger various problems in the cell, as shown in Figure 1.

2.2. Negative electrode materials

2.2.1. Lithium metal

The remarkable features of Li metal among the other negative electrode materials are the lowest standard electrode potential (-3.04 V *vs.* NHE) and the largest specific capacity (3,860 mA h g^{-1}).[5] Because of these superior properties, Li metal is considered as an ultimate goal of the negative electrode. Industrial application of the electrode, however, has been suspended, because it has several intrinsic problems that potentially cause safety issues. First, uneven mass transfer of Li^+ ions lead to dendritic growth Li metal on the surface, which can damage separator to short-circuit the cell. Second, continuous electrolyte decomposition on Li metal can produce dead lithium. Li metal undergoes severe volume change during charge/discharge, which provokes cracks of SEI (solid-electrolyte interphase) and exposure of unpassivated metal surface. Electrolytes are continuously decomposed on the newly exposed surface resulting in a thick film on the surface, which can block the electron and Li^+ transfer and produce isolated Li metal. The isolated Li metal, as known as dead lithium, not only reduce the capacity of negative electrode, but also trigger safety problems. In order to mitigate the problems, many efforts have been made in recent studies to coat polymer or inorganic film on the surface of Li metal.[27]

2.2.2. Carbonaceous materials

2.2.2.1. Graphite

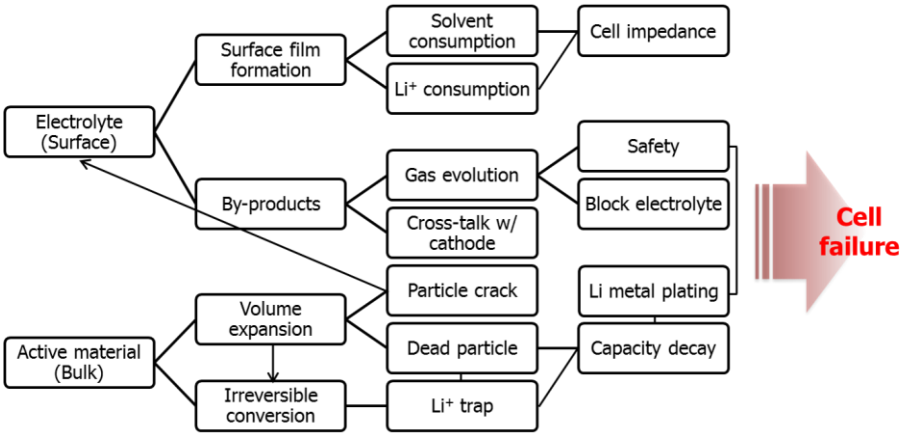

Figure 1. The origins and the consequences of irreversible reactions on the negative electrodes.

Graphite consists of parallel graphene sheets which are bound to each other with the interaction of π bonds. During charging (lithiation), Li^+ ions can be intercalated into the layer between the graphene sheets as is written in Equation 2-5. Lithiation in graphite occurs with the gradual Li^+ intercalation in graphene layers, which is called staging.[28] At the end of lithiation, graphite forms a composition of LiC_6, which shows a theoretical capacity of 372 mA h g^{-1}.

$$C_n + x\,Li^+ + x\,e^- \leftrightarrow Li_xC_n \qquad \textbf{Equation 2-5}$$

2.2.2.2. Non-graphitic carbon (Amorphous carbon)

The non-graphitic carbons, or amorphous carbon, consists of small hexagonal networks of carbon without long-range order. Strong crosslinking between the networks make the structure in amorphous phase.[29] Since there exist a wide range of possible sites in which the lithium ion can be stored, having different local structures and energies, the notable features of the non-graphitic carbon are a sloping voltage curve and enlarged specific capacity compared to the graphite. It is also observed that there exists an irreversible capacity loss, resulted from the Li^+ ions trapped in the structure and/or reacted with functional groups on the surface of carbon during the first cycle.[7]

2.2.3. Alloying materials

One of the most promising alternatives for the negative electrode is Li-alloying metals. The redox reaction of Li-alloying metals proceeds as described in the following equation:[30]

$$M + x\,Li^+ + x\,e^- \leftrightarrow Li_xM \qquad \textbf{Equation 2-6}$$

There are a lot of metals which can form alloy with lithium. Among them, Si-based compounds, such as Si and SiO_x, are most popular due to its higher specific capacity, 3579 mA h g^{-1} for $Li_{15}Si_4$, and its reasonable cost.[31]

However, they undergo severe volume expansion during lithiation which deteriorate the composite electrode including pulverization and lead to cell failure. In order to overcome these severe volume change during cycles, many researches have provided various solutions: (i) reduction of particle size and introduction of porous structure,[32,33] (ii) construction of composites with active/inactive metals or intermetallic alloys,[34,35] (iii) fabrication of composite electrodes with strongly adhesive binders.[36,37]

2.2.4. Transition metal oxides

2.2.4.1. Insertion-type metal oxides

2.2.4.1.1. Insertion reaction mechanism

In the insertion reaction, Li^+ ion storage occurs in well-defined interstitial sites of crystalline structures or in the structural defects of the amorphous phase.[7,9] The original metal-oxygen framework of the materials is maintained during lithiation and delithiation, because Li^+ ions can reside at sites which already exist in the structure. During this process of Li^+ insertion, transition metal ions work as redox center, which uptake electrons from the electric circuit (lithiation) or release electrons to the electric circuit (delithiation) for the charge compensation. The reaction can be written as follows:

$$MO_n + x\,Li^+ + x\,e^- \leftrightarrow Li_xMO_n \qquad \textbf{Equation 2-7}$$

Since the sites for Li^+ ions are limited, insertion materials generally has smaller Li^+ storage capacity compared to other types of materials. However, insertion-type reaction, which is relatively stable, results in a low volumetric expansion and stable cycle life.[9–11]

2.2.4.1.2. Insertion-type metal oxides for negative electrodes

Ti-based oxides such as lithium titanate ($Li_4Ti_5O_{12}$, LTO)[10,38,39] and titanium oxides (TiO_2)[40–42] are most popular insertion-type negative electrodes. Here, Li plating is unlikely even under high-current charging because their working potential (1.5 – 1.8 V *vs*. Li/Li^+) is much higher than that of Li metal. This high-current performance of TiO_2 is, however, largely offset by the limited specific capacity (< 200 mA h g^{-1}). Their latent specific capacity cannot be fully utilized because of the irreversible changes to inactive phases upon deep charging.[43] $Li_4Ti_5O_{12}$ has been applied in commercial use for high-power applications such as power tools and hybrid electric vehicles (HEV). Its lattice structure does not alter upon Li^+ storage as known as a zero-strain material[38] and its working potential is high enough to operate within the electrochemical stability window of the electrolyte solution, LTO shows a superior stability during cycles. However, it has a theoretical capacity of 175 mA h g^{-1}, which limits its application by reducing the energy density of the full-cell.

2.2.4.2. Conversion-type metal oxides

2.2.4.2.1. Conversion reaction mechanism

In contrast to the insertion-type materials that have a fixed number of storage sites, metal oxides which store Li^+ ions through a conversion reaction have merits especially for their enlarged specific capacity because the original framework of metal oxides is destroyed during lithiation.[14] At the same time, metal ions are reduced into their elemental

states with the cleavage of metal-oxygen bonds and Li^+ ions form new bonds with oxygen and generate lithium oxide (Li_2O) matrix.[12–14] Since the nano-sized metal and lithium oxide (Li_2O) are generated after lithiation, the reverse reaction (delithiation) becomes feasible because the contact area between the two components is large and solid-state diffusion length is short.[14,44,45] The conversion reaction can be expressed as follows:

$$MO_2 + 4\,Li^+ + 4\,e^- \leftrightarrow M + 2\,Li_2O \qquad \textbf{Equation 2-8}$$

The specific capacity of conversion-type oxides, which is determined by the oxidation state of metal ions (for example, four Li^+ ions/electrons per formula unit of $M(IV)O_2$ as shown in Equation 2-2), is generally larger than that of the insertion-type oxides. However, conversion-type metal oxides have a severe volume change and poor cycle performance.

2.2.4.2.2. Atomic number – redox potential relationship

The experimentally observed potentials for conversion reaction from the previous reports, which are the transient values combining the thermodynamic value (equilibrium potential for conversion reaction) and polarization (kinetic value), show a rough linear relationship to atomic number for the 3d transition metal oxides (Figure 2). This feature can be explained on the basis of thermodynamic consideration. The thermodynamic reduction potential of early transition metal ions is lower (more negative) than that for the later transition metal ions.[6] The similar trend can also be noticed from the bond dissociation energies calculated from Equation 2-9 and Equation 2-10 (Figure 3).[46]

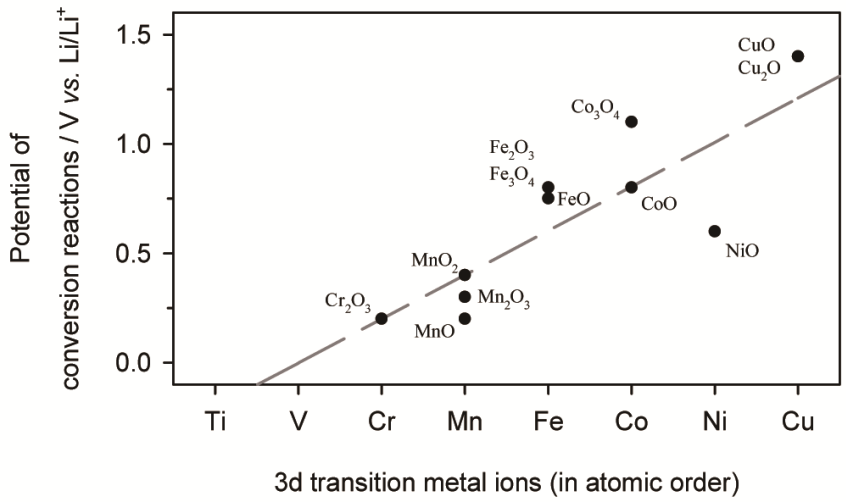

Figure 2. The empirical values and their regression curve of conversion potentials of 3d transition metal oxides.[14]

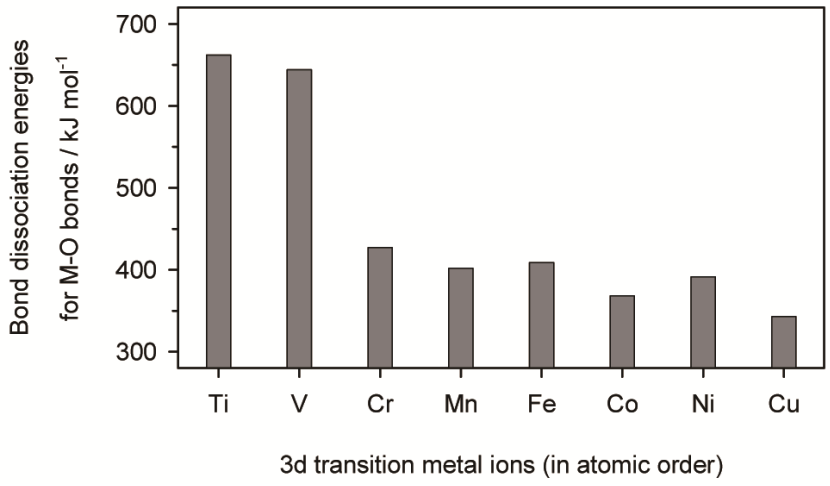

Figure 3. Bond dissociation energies of M—O bonds calculated from the Equation 2-10.

$$M + O \rightarrow MO$$ **Equation 2-9**

$$\Delta H_f = \Delta H_f(M) + \Delta H_f(O) - \Delta H_f(MO)$$ **Equation 2-10**

Thus, the conversion-type lithiation is not thermodynamically favored for the early transition metal oxides. Meanwhile, the conversion reaction is kinetically hindered due to a large activation barrier for the diffusion/rearrangement of mobile species such as Li^+, M^{n+} and O^{2-} ions.[47] In short, in the case of early transition metal oxides (for example, titanium oxides and vanadium oxides), the conversion reaction is not thermodynamically favored and kinetically hindered. As is seen in Figure 2, the potential for conversion reaction for titanium oxides and vanadium oxides is not appeared at > 0.0 V (vs. Li/Li^+), but seems to locate at < 0.0 V.

2.2.4.2.3. Conversion-type metal oxides for negative electrodes

Conversion reaction can occur in the most of latter transition metal oxides such as Fe_2O_3, CoO, Co_3O_4, MnO_2, etc.[12,48–50] They are lithiated at the relatively high working potential as seen in Figure 2 and delithiated with a large voltage hysteresis over 0.8 V upon charge/discharge. Because of these reasons, their energy density is rather limited in spite of their large specific capacity. Thus, a large voltage hysteresis and a high redox potential should be overcome in order to increase the energy density of full-cell applications.

CHAPTER 3. EXPERIMENTAL

3.1. Synthesis of materials

3.1.1. Amorphous vanadium titanates (*a*VTO, *a*VTO-N)

Amorphous vanadium titanates (*a*VTO) were synthesized by a precipitation method. In detail, 2.5 g of vanadium oxide sulfate hydrate ($VOSO_4 \cdot xH_2O$, Alfa Aesar) and 2.5 g of titanium oxide sulfate sulfuric acid hydrate ($TiOSO_4 \cdot xH_2O+H_2SO_4$, Alfa Aesar) were dissolved in 250 ml of distilled water. Then, the precursor solution was dropped into a gas (air or nitrogen)-purged urea solution to obtain precipitates.[51] In this process, the reaction temperature was fixed at 60°C and ammonia solution was dropped into the solution to maintain the solution pH at 7. The precipitate obtained under air and nitrogen atmosphere was named *a*VTO and *a*VTO-N, respectively. The resulting precipitates were centrifuged and washed with distilled water, which was followed by drying at 80°C for overnight and additional drying at 300°C under vacuum for 2 h. For comparison purpose, amorphous vanadium pentoxide (aV_2O_5) and titanium oxide ($aTiO_2$) were also synthesized with the same procedure being used for *a*VTO.

3.1.2. Lithium metavanadate ($LiVO_3$)

$LiVO_3$ was prepared by a solid-state reaction. Lithium carbonate (Li_2CO_3, Sigma Aldrich) and vanadium pentoxide (V_2O_5, Sigma Aldrich) were mixed in stoichiometric

quantities (1: 1 in *mol.* ratio) in an agate mortar. The mixture was put into a platinum crucible and annealed at 750°C for 4 h in air. After cooling down to room temperature, the prepared $LiVO_3$ was crushed in an agate mortar and ball-milled for 1 h to make particles small and uniform in size.

3.1.3. Copper vanadate (CuV_2O_6)

Copper vanadate (CuV_2O_6) was prepared via a solid-state method. Copper (II) oxide (CuO, Sigma Aldrich) and vanadium pentoxide (V_2O_5, Sigma Aldrich) were mixed in stoichiometric quantities (1: 1 in *mol.* ratio) using planetary ball-mill at 300 rpm for 1 h. The mixture was pelletized and put into an alumina crucible and annealed at 600°C for 48 h in air. After cooling down to room temperature, the prepared CuV_2O_6 was crushed in an agate mortar and ball-milled for 5 minutes to make particles small and uniform in size.

3.2. Electrochemical analysis

3.2.1. Electrode fabrication

3.2.1.1. Amorphous vanadium titanates (*a*VTO, *a*VTO-N), amorphous TiO_2 (*a*TiO_2) and amorphous V_2O_5 (*a*V_2O_5)

To prepare the composite electrodes of *a*VTO, *a*VTO-N and other materials (*a*TiO_2, *a*V_2O_5) for controlled experiments, the synthesized metal oxides, Super-P, styrene-butadiene rubber (SBR) and carboxymethyl cellulose (CMC) (80: 10: 5: 5 in *wt.* ratio) were mixed in agate mortar and dispersed in distilled water. The slurry was then coated on a

copper foil (LS wire) with doctor blade in drying room. The composite electrodes were punched and dried at 120°C for overnight in vacuum.

3.2.1.2. Lithium metavanadate ($LiVO_3$)

To prepare composite electrodes of $LiVO_3$ and crystalline V_2O_5 (Sigma Aldrich), the active material, Super-P, and polyvinylidenefluoride (PVdF) (8: 1: 1 in *wt.* ratio) were mixed in an agate mortar and dispersed in N-methyl pyrrolidone (NMP). The slurry was then coated onto a copper foil (LS wire) with a doctor blade in a dry room. The composite electrodes were punched and dried at 120°C overnight in vacuum.

3.2.1.3. Copper vanadate (CuV_2O_6)

CuV_2O_6 electrodes for comparison of electrochemical properties with $LiVO_3$ were fabricated with same procedure with that of $LiVO_3$ electrodes. CuV_2O_6 electrodes for cycle retention test was fabricated with polyacrylate lithium salt (LiPAA) binder. Lithium hydroxide (LiOH, ACS reagent > 98.0 %) and poly(acrylic acid) (PAA, average Mv ~450,000) were dissolved in distilled water with stoichiometric ratio of 1: 1 to make a LiPAA binder solution. To prepare the composite electrodes of CuV_2O_6, CuV_2O_6 were mixed with Super-P and dispersed in the LiPAA binder solution. The active material, Super-P, LiPAA (80: 10: 10 in *wt.* ratio) were then coated on a copper foil (LS wire) with doctor blade in a drying room. The composite electrodes were punched and dried at 120°C for overnight in vacuum.

3.2.2. Cell fabrication

With the composite electrodes, 2032-type coin cells were fabricated in an argon-filled dry box. Lithium foil and trilayered polypropylene-polyethylene membrane (PP-

PE-PP, Celgard 2320) were used as a counter electrode and a separator, respectively. As a lithium conducting electrolyte, 1.0 *M* $LiPF_6$ was dissolved in ethylene carbonate (EC) and dimethyl carbonate (DMC) (1: 2 in *vol.* ratio).

3.2.3. Galvanostatic charge/discharge

Electrochemical analysis of materials were conducted using a WBCS 3000 battery cycler (Wonatech Co., Ltd.) at 25°C (normal condition) and 60°C (elevated temperature). For the electrochemical study of amorphous vanadium titanates (*a*VTO, *a*VTO-N) and amorphous TiO_2 and V_2O_5, galvanostatic lithiation and de-lithiation cycling was performed at a current density of 100 mA g^{-1} over the potential range of 0.8 – 3.0 V (*vs.* Li/Li^+). The current density was varied from 50 mA g^{-1} to 1,000 mA g^{-1} for the rate capability test. For the electrochemical study of lithium metavanadate ($LiVO_3$), crystalline V_2O_5 and copper vanadate (CuV_2O_6), galvanostatic lithiation and de-lithiation was performed in a constant current-constant voltage (CC-CV) mode at a current density of 100 mA g^{-1} over the potential range of 0.005 – 3.0 V (vs. Li/Li^+). For complete lithiation, an additional constant-voltage step was added at 0.005 V until current decayed to 10 mA g^{-1}.

3.2.4. Potentiostatic intermittent titration technique (PITT)

Potential intermittent titration technique (PITT) and electrochemical voltage spectroscopy (EVS) measurement were employed to analyze the type of reactions during lithiation in $LiVO_3$. The cell potential was decreased stepwise by 50 mV and the current was continuously monitored until it decayed to a preset threshold value.

3.2.5. Electrochemical impedance spectroscopy (EIS)

ac impedance measurement was performed to examine the kinetic properties of $Li/LiVO_3$ and Li/V_2O_5 cells during conversion reaction using CHI 660E (CH Instrumetns, Inc.). Measurements were performed for the $Li/LiVO_3$ and Li/V_2O_5 cells with state of charge (SOC) 60% in the frequency range of 0.005 Hz − 100 kHz with an ac amplitude of 5 mV. The spectra were fitted with an equivalent circuit to obtain the impedance parameters.

3.2.6. Galvanostatic intermittent titration technique (GITT)

For the galvanostatic intermittent titration technique (GITT), a sequential current pulse of 10 mA g^{-1} was applied for 1 h to measure the closed-circuit voltage (CCV) and turned off for 2 h to obtain the quasi-open-circuit voltage (QOCV) at 60°C. The internal resistance was calculated from the difference between the CCV and QOCV in each current pulse.

3.3. Material characterization

3.3.1. Electron microscopy

3.3.1.1. Transmission electron microscopy (TEM)

Energy Dispersive X-ray Spectroscopy (EDS) mapping to observe the distribution of titanium and vanadium ions in *a*VTO and *a*VTO-N was obtained by using a scanning transmission electron microscope (STEM, Tecnai F20). Transmission electron microscopy (TEM) images and selected area electron diffraction (SAED) patterns of cycled $LiVO_3$ and CuV_2O_6 were obtained with the JEOL JEM-2100F and an acceleration voltage of 200 kV. The cycled $Li/LiVO_3$ and Li/CuV_2O_6 cells were disassembled and the active

materials were dispersed in dimethyl carbonate (DMC) solvent by using the Branson 5210 ultrasonicator.

3.3.1.2. Field-emission scanning electron microscopy (FE-SEM)

The particle morphology and size of synthesized oxides were examined using a field-emission scanning electron microscopy (FE-SEM, JEOL JSM-6700F). For the images of post-mortem analysis of the $LiVO_3$ electrodes, cycled $Li/LiVO_3$ cells were disassembled and the electrodes were washed with dimethyl carbonate (DMC) solvent in an Ar-filled glove-box. For the cross sectional images, washed electrodes were crosscut by an Ar ion beam polisher (SM-09010, JEOL) at a constant power of 0.5 W (5 kV and 0.1 mA) under vacuum ($<2.0 \times 10^{-4}$ Pa).

3.3.2. Spectroscopic analysis

3.3.2.1. X-ray diffraction (XRD)

X-ray diffraction (XRD) patterns of synthesized oxides were obtained using D8-Bruker diffractometer equipped with Cu Kα radiation (1.54056 Å) operated at 40 kV and 40 mA. *Ex-situ* XRD patterns of $LiVO_3$ and CuV_2O_6 electrodes were measured with a Rigaku D/Max-3C diffractometer (Cu-Ka radiation source) operated at 50 kV and 200 mA. After the measurement, the XRD patterns were calibrated with the characterizing XRD peak of the current collector, Cu foil, of the electrodes.

3.3.2.2. Synchrotron X-ray absorption spectroscopy (XAS)

X-ray absorption spectroscopy (XAS) data of titanium K-edge (E_0 = 4966 eV), vanadium K-edge (E_0 = 5465.1 eV) and copper K-edge (E_0 = 8979 eV) were obtained using transmission mode with a ring current of 320–400 mA at 3.0 GeV at the Pohang Light

Source (PLS). A Si (111) monochromator crystal was used with detuning to 70% in intensity to eliminate the high-order harmonics in case of Ti and V, 80 % in intensity for Cu. Energy calibration for Ti, V and Cu K-edge was carried out using Ti, V and Cu metal foil, respectively. Electrodes used for the *ex-situ* analysis were prepared with different state of lithiation. Cells were disassembled and the electrodes were washed with dimethyl carbonate (DMC) solvent in an Ar-filled glove-box and sealed with Kapton tape to prevent exposure to air.

3.3.2.3. X-ray photoelectron spectroscopy (XPS)

The X-ray photoelectron spectroscopy (XPS) data were collected in an ultra-high vacuum multipurpose surface analysis system (Sigma probe, Thermo, UK) operating at base pressure of $<10^{-10}$ mbar. The photoelectrons were excited by an Al Kα (1486.6 eV) anode operating at a constant power of 100 W (15 kV and 10 mA). For post-mortem XPS analysis, *a*VTO and *a*VTO-N electrodes were prepared by embedding the powder onto a copper foil, with which the interferences coming from the conductive carbon (Super-P) and the polymer binder (SBR-CMC) can be eliminated. The cycled cells were disassembled and the electrode samples were washed with dimethyl carbonates (DMC) in an argon-filled glove box. They were then transferred to XPS instrument without air exposure. The binding energy was calibrated from the hydrocarbon contamination using the C 1s peak at 285.0 eV.

3.3.2.4. Fourier Transform Infrared spectra (FT-IR)

Fourier Transform Infrared spectra (FTIR) transmission spectra for *a*VTO and reference oxides and Fourier Transform Infrared spectra (FTIR)-Attenuated Total Reflectance (ATR) spectra for *a*VTO and *a*VTO-N were measured with a Bruker Vertex 80V

IR spectrometer in vacuum to eliminate the adsorbed water on the surface. The samples for transmission spectra were pelletized with potassium bromide (KBr). The sample for ATR measurement were prepared by slurry coating on copper foil with 8:2 weight ratio of active material and polyvinylidenefluoride (PVdF). PVdF binder was used to minimize the interference of functional groups of binder.

3.3.3. Other techniques

3.3.3.1. Inductively-coupled plasma (ICP)

Atomic ratio of Ti and V in *a*VTO and *a*VTO-N was measured by inductively-coupled plasma (ICP) technique using Optima-4300 DV installed at the National Center for Inter University Research Facilities (NCIRF) in Seoul National University.

3.3.3.2. Brunauer-Emmett-Teller (BET)

The BET surface area and BJH adsorption average pore size of *a*VTO and *a*VTO-N were measured from the nitrogen adsorption isotherm using Micromeritics analyzer ASAP 2010.

3.4. Computation methods

Ab-initio calculations on the lithiation process in $LiVO_3$ were performed using the density functional theory (DFT) with the spin-polarized generalized gradient approximation (GGA) and the Perdew-Burke-Ernzerhof functional for the exchange correlation. The projector augmented wave (PAW) method and a plane wave basis set implemented in the Vienna *ab-inito* simulation package (VASP) were used. A plane-wave basis with an energy cutoff of 400 eV was used and the appropriate numbers of k-points were used,

depending on the size of the unit cells. All geometric relaxations were performed until all forces of the system converged within 0.05 eV $Å^{-1}$. The kinetic of 500 eV and reciprocal-space k-point meshes of 4 × 4 × 4 using the Monkhorst-Pack scheme were included in all calculation. For the *ab-initio* molecular dynamics simulation, the k-point was only sampled at the gamma point. All geometric relaxations were performed until all forces of the system converged within 0.01 eV $Å^{-1}$. The calculated voltage upon lithiation was predicted with the standared approach. More detailed procedure is stated along with the simulation results.

CHAPTER 4. RESULTS AND DISCUSSION

4.1. Insertion-type lithium storage in amorphous vanadium titanate (*a*VTO) and its performance improvements

As introduced in the Section 2.2.4.1, lithium titanate ($Li_4Ti_5O_{12}$, LTO) and titanium oxides (TiO_2) have superior stability and power performance, which offset by the limited specific capacity (LTO; ~175 mA h g^{-1}, TiO_2; ~200 mA h g^{-1}).[39,41,42] In case of TiO_2, its theoretical specific capacity, 335 mA h g^{-1}, cannot be fully utilized because of irreversible changes to inactive phases upon charging over 0.5 mol of Li^+.[43]

As a way to prevent or mitigate the irreversible phase transitions, TiO_2 has been prepared in nanostructures or amorphous phases. It implies that the irreversible phase transitions can be suppressed by introducing disorders; for instance, structural defects such as vacancies and void spaces on the surface of nanostructured materials, or in the bulk of amorphous materials.[52] The amorphization of electrode materials has also been proven as an effective way to increase the Li^+ storage sites and to facilitate solid-state Li^+ diffusion.[52,53] This is very likely because the structural defects (vacancies and void spaces) can serve as Li^+ storage sites, which is well-known for hard carbons.[7,54] In addition, solid-state Li^+ diffusion can be facilitated through the abundant void spaces in amorphous materials.[11] Recent studies have demonstrated that several amorphous materials can be successfully applied in Na^+ ion batteries.[55,56] These results also imply that the amorphous

framework provides storage sites and diffusion channels large enough even for Na^+ ions which are larger than Li^+ ions in size.

The previous studies revealed that the rate performance of TiO_2 electrode can be improved to a degree by amorphization, but the specific capacity cannot be dramatically enlarged compared to other amorphized metal oxides.[57–59] The capacity limitation can be understood by considering the following fact. Because lithiation proceeds via co-injection of Li^+ ions and the equivalent amount of electrons, electrode materials should carry both Li^+ storage sites and electron storage sites (redox centers). Even if Li^+ storage sites (vacancies and void spaces) can be increased by amorphization in TiO_2, the electron accepting capability cannot be enlarged through amorphization because the redox center is the metal Ti ions in TiO_2. In this work, to increase the specific capacity of amorphous TiO_2 ($a$$TiO_2$), a mixed oxide containing Ti and V ions was prepared with the expectations based on the previous literatures that suggested V^{5+} ions in amorphous V_2O_5 ($a$$V_2O_5$) can uptake more electrons than Ti^{4+} ions in $a$$TiO_2$ at > 1.0 V.[60,61] If this is the case in the mixed oxide prepared in this work, V^{5+} ions can show a higher electron accepting ability as a redox center compared with Ti^{4+} ions. The net results will be an increase of specific capacity. The other affirmative reports on the role of V^{5+} ions are that homogeneous mixing of V^{5+} and Ti^{4+} ions in the oxide matrix can produce a larger number of structural disorders that can play as additional Li^+ storage sites.[62,63]

In order to introduce V^{5+} ions into $a$$TiO_2$, amorphous vanadium titanate (aVTO) was synthesized by using a simple precipitation method. The followings were examined with the synthesized aVTO: (i) If the V and Ti ions in aVTO are homogeneously mixed in an atomic scale instead of physical mixture of $a$$V_2O_5$ and $a$$TiO_2$. (ii) How the oxidation state and local structure around the V and Ti ions in aVTO differ from those in their respective oxide ($a$$V_2O_5$ and $a$$TiO_2$). (iii) How the Li^+ storage sites and redox centers in aVTO differ

from those in their respective oxide. Another objective of this work was to decrease the surface impurities such as surface hydroxyl groups and residual water, which are known to cause side reactions to lower Coulombic efficiency and to increase electrode resistance.[64,65] Note that, in this work, the amorphous materials were synthesized by a precipitation method without high temperature heat-treatment, such that high population of surface hydroxyl groups and residual water is unavoidable. The effects of these impurities on the electrode performance of *a*VTO were examined. As a way to remove these impurities, the synthetic atmosphere was changed from air to nitrogen with a great success. The effects that the reaction atmosphere has on the impurity population and electrode performances were examined.

4.1.1. Material characterization

4.1.1.1. Bulk properties of the amorphous vanadium titanate (*a*VTO)

Figure 4a and b show the FE-SEM images taken from the synthesized *a*VTO powder. Its size was approximately several microns, composed of small primary particles of <100 nm in size, resulting in a large surface area as shown in Table 1. This morphology of *a*VTO powder is advantageous in high-power applications by providing the short Li^+ diffusion path within the bulk material and the wide contact area with the electrolyte solution.[53,66–68] Figure 4c-e shows the STEM and EDS mapping, which illustrates that titanium and vanadium are homogeneously dispersed within the nano-sized primary particles. The ICP measurement reveals that the atomic ratio of titanium and vanadium is close to 1: 1. The XRD pattern and FFT pattern obtained from the *a*VTO powder was featureless, indicative of amorphous nature of the synthesized powder (Figure 5).

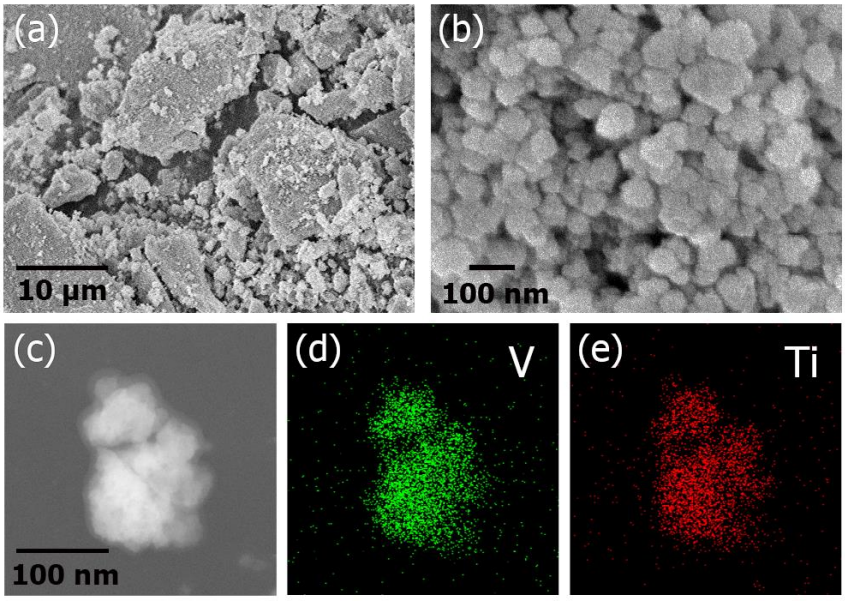

Figure 4. (a) and (b); FE-SEM images of *a*VTO, (c); STEM image of *a*VTO, and (d) and (e); EDS mapping for vanadium and titanium.

Table 1. BET surface area and BJH adsorption average pore diameter of *a*VTO and *a*VTO-N.

	*a*VTO	*a*VTO-N
BET surface area / $m^2 g^{-1}$	54.39	62.77
BJH adsorption average pore diameter / nm	8.48	16.37

4.1.1.2. Local structures and valence states of metal ions in *a*VTO

Synchrotron X-ray absorption fine structure (XAFS) gives us the information on local structures (< 10 Å) of selected atomic species in materials. Thus, when two materials are physically mixed, one cannot affect the local structures (< 10 Å) of the other. However, the cross interaction is possible in the atomic scale mixing. The metal valence and local structure of metal ions in *a*VTO and physically mixed aV_2O_5 + $aTiO_2$ were observed and compared by using X-ray absorption near-edge structure (XANES) spectra (Figure 6) and extended X-ray absorption fine structure (EXAFS) spectra (Figure 7). The appearance of main edge of vanadium, which is a common feature for crystalline vanadium pentoxide (cV_2O_5),[69] signifies that the vanadium valence is 5+ for both *a*VTO and aV_2O_5 (Figure 6a). Meanwhile, the titanium valence is 4+ in both *a*VTO and $aTiO_2$ because the main edge appears like the crystalline titanium oxide ($cTiO_2$). The local structure of V^{5+} in *a*VTO and aV_2O_5 was analyzed from the data shown in Figure 6 and Figure 7. The pre-edge of vanadium K-edge does not appear if the local symmetry of V^{5+} is octahedral. With a decrease in local symmetry from octahedron, the pre-edge of vanadium K-edge becomes stronger due to a formally forbidden dipole transition from vanadium 1s orbital to oxygen 2p states hybridized with 3d orbital.[70] As is seen in Figure 6a, the orthorhombic V_2O_5 (cV_2O_5) shows a strong pre-edge since vanadium ions are located in the five-coordinated (VO_5) square pyramidal sites,[61] which is far less symmetric compared to octahedral six-coordination. This strong pre-edge peak is also observed in both aV_2O_5 and *a*VTO, implying that the local structure of V^{5+} is not octahedral. The detailed local structure can be estimated from the V − O shell depicted in Figure 7a. As seen in the figure, the local structure of vanadium ions is far different between *a*VTO and aV_2O_5; tetrahedral coordination in *a*VTO and square pyramidal coordination in aV_2O_5. The V − O peak of orthorhombic V_2O_5 (cV_2O_5) is small in intensity and divided into two (black

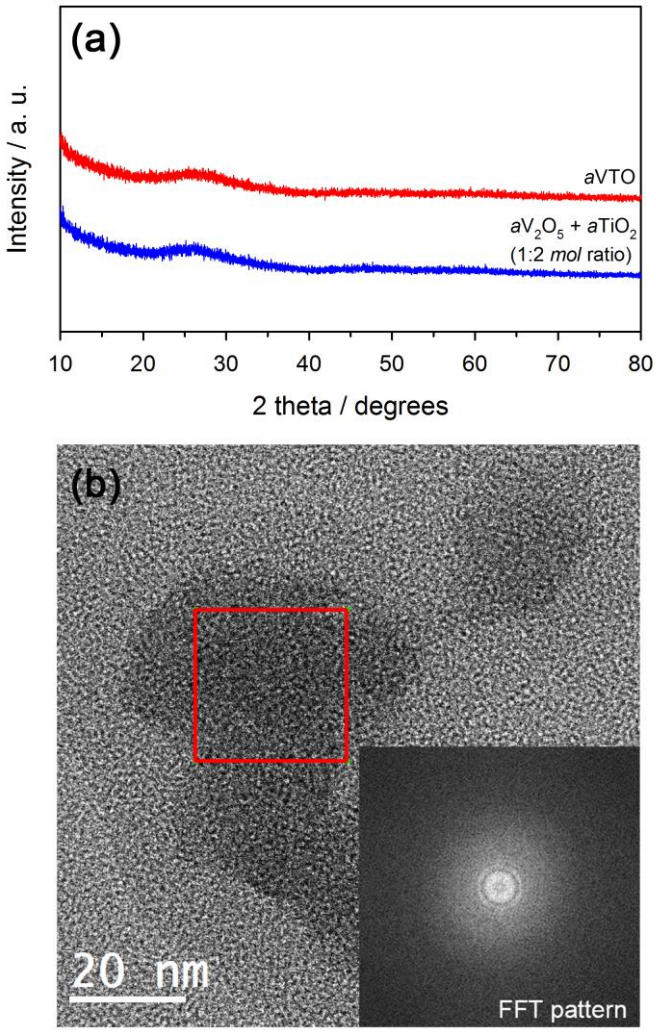

Figure 5. (a) X-ray diffraction (XRD) pattern of *a*VTO powder and aV_2O_5 + $aTiO_2$ (1:2 *mol* ratio) powder dried at 300ºC under vacuum. (b) HR-TEM image of *a*VTO; the inset shows the FFT pattern of *a*VTO.

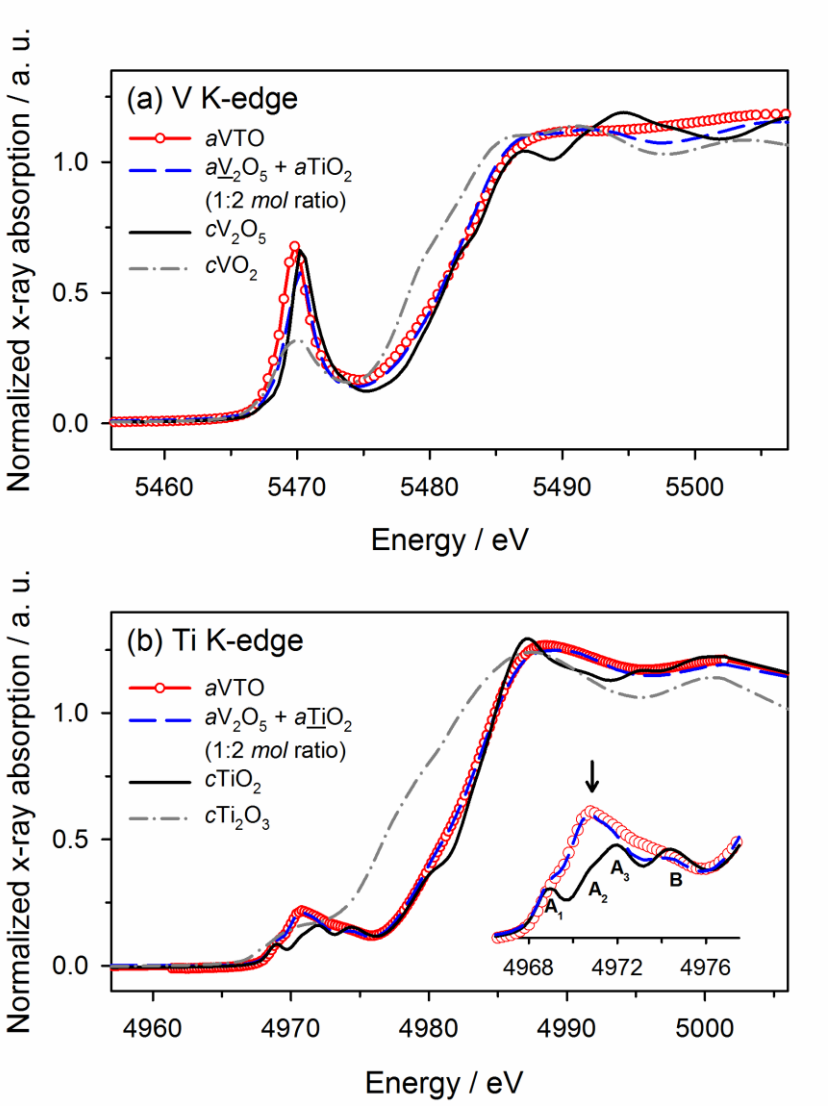

Figure 6. X-ray absorption near-edge structures (XANES) data for *a*VTO and some reference oxides: (a); vanadium K-edge and (b); titanium K-edge. XANES data for amorphous V_2O_5 and TiO_2 are taken from physically mixed *a*TiO_2 + *a*V_2O_5 electrode.

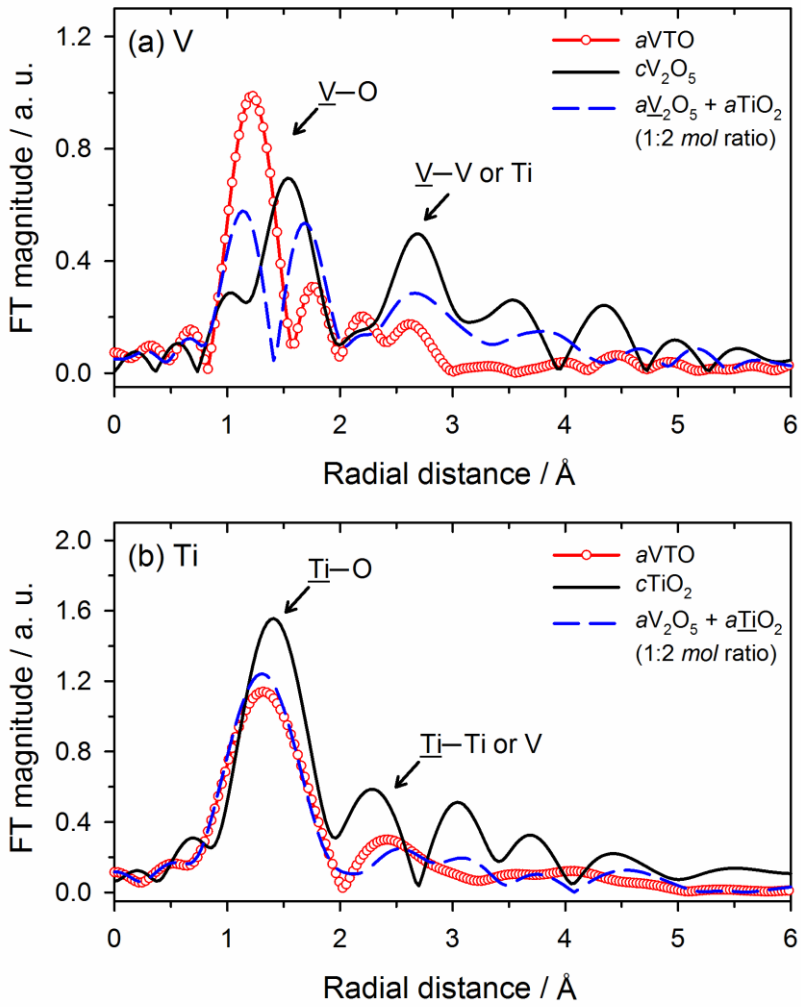

Figure 7. Fourier transformed extended X-ray adsorption fine structures (EXAFS): (a); vanadium K-edge and (b); titanium K-edge for *a*VTO and reference oxides. EXAFS data for amorphous V_2O_5 and TiO_2 are taken from physically mixed $aTiO_2$ + aV_2O_5 electrode.

line), which must be due to the fact that V − O shell is composed of one short V = O bond (1.07 Å) and four long V − O bonds (1.53 Å) (five-coordinated square pyramidal sites as shown in Figure 7a). *a*V_2O_5 also shows a similar V − O shell comprising a short V = O bond and long V − O bonds even if the intensity of the former is stronger than the latter (blue line), illustrating that the local structure of V^{5+} in *a*V_2O_5 is not far different from that for *c*V_2O_5 (five-coordination). However, the local structure of V^{5+} in *a*VTO is not five-coordination as evidenced on the EXAFS data in Figure 7a. Namely, the V − O shell gives an intensified single peak at 1.20 Å, which corresponds to a tetrahedral symmetry around the V^{5+} ions.[71] To confirm the tetrahedral coordination in *a*VTO, the EXAFS data obtained from $LiVO_3$, in which the V^{5+} ions are known to be located in tetrahedral sites, is compared with that obtained from *a*VTO. As is seen in the figure, the EXAFS data of *a*VTO is quite similar to that of $LiVO_3$, ensuring the tetrahedral coordination of vanadium ions in *a*VTO.

The different V^{5+} local structure between *a*VTO (four-coordination) and *a*V_2O_5 (five-coordination) is an indication that *a*VTO is not a physical mixture of *a*V_2O_5 and *a*TiO_2, rather the V^{5+} and Ti^{4+} ions are homogeneously mixed in atomic scale. This feature of *a*VTO can be confirmed on the FTIR data in Figure 8. The physically mixed *a*V_2O_5 + *a*TiO_2 sample shows a sharp peak at 1,000 cm^{-1}, which corresponds to V = O bond in the elongated octahedral (or square pyramidal) structure. On the contrary, *a*VTO shows no V = O peak around 995 – 1028 cm^{-1}, indicating that the local structure around V^{5+} ions in *a*VTO is far different from that of *a*V_2O_5. Meanwhile, *a*VTO gives a weak shoulder around 950 – 980 cm^{-1}, which comes from Ti–O–V bonds as proposed in the literature.[72] This result strongly evidences that the homogeneous dispersion of vanadium and titanium ions in *a*VTO generates Ti–O–V bonds.

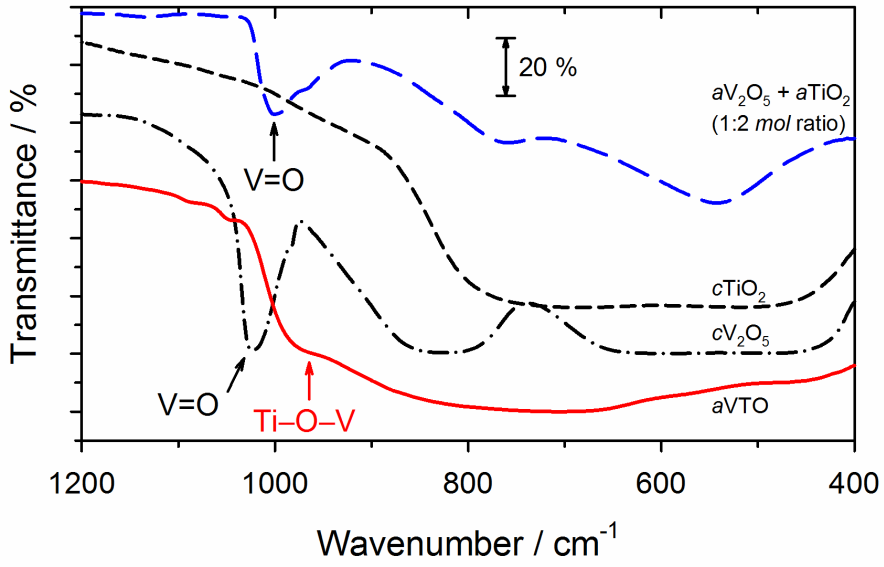

Figure 8. Fourier Transform Infrared spectra (FTIR) measured in vacuum for KBr pelletized *a*VTO, *c*V_2O_5, *c*TiO_2 and a physical mixture of *a*V_2O_5 and *a*TiO_2.

The local structure of Ti^{4+} in *a*VTO and *a*TiO_2 was also analyzed. The titanium pre-edge peaks from the crystalline (anatase) TiO_2 (*c*TiO_2) appear at 4969.2 eV, 4970.8 eV, 4972.0 eV and 4974.4 eV, which have been named A_1, A_2, A_3 and B as shown in the inset of Figure 6b.[73] The former three (A_1, A_2 and A_3) are due to the dipole transitions to titanium 4p states hybridized with titanium 3d orbitals that are split into t_{2g} and e_g band, respectively.[73] As shown in Figure 6b, the A_2 and A_3 peaks from *a*TiO_2 and *a*VTO are much stronger than that for *c*TiO_2, implying that the regular TiO_6 octahedron, which is dominant in anatase TiO_2, is distorted to form an irregular five-fold coordination (TiO_5) in both *a*TiO_2 and *a*VTO.[57,74,75] This feature can be ascertained from the radial distribution obtained from the Fourier transformation of EXAFS spectra shown in Figure 7b. The Ti − O bond in *c*TiO_2 is located at 1.41 Å, but this peak is shifted to 1.35 Å for *a*TiO_2 and *a*VTO. This observation coincides with the XANES spectra that suggest an irregular five-fold coordination for Ti^{4+} in *a*TiO_2 and *a*VTO. That is, the Ti − O bond length is shorter for five-coordination (*a*TiO_2 and *a*VTO) compared to the six-coordination (*c*TiO_2). In short, it is demonstrated that *a*VTO is composed of atomic scale homogeneous mixing of irregular TiO_5 and tetrahedral VO_4, rather than the physical mixture of two separate oxides by X-ray absorption fine structures (XAFS) and Fourier transformed infrared (FTIR) spectroscopy.

4.1.2. Electrochemical properties and *ex-situ* analysis

4.1.2.1. Galvanostatic lithiation/delithiation

The galvanostatic lithiation and de-lithiation voltage profiles of the Li/*a*VTO cell are shown in Figure 9a. The Li/*a*VTO cell shows a sloping voltage profile, which is the

characteristic feature for amorphous electrodes, and gives a reversible capacity of 295 mA h g^{-1} in the first cycle.

Note that this value is much larger than those of LTO (175 mA h g^{-1}) and anatase TiO_2 (168 mA h g^{-1}) and even amorphous TiO_2, which shows a slightly larger capacity compared to that of anatase TiO_2 (Figure 9c). The mechanically mixed *a*V_2O_5 and *a*TiO_2 electrode, which were mixed in 1: 2 (mole ratio) to simulate the atomic ratio (1: 1) in *a*VTO, delivers a reversible capacity of 245 mA h g^{-1} in the first cycle (Figure 9b). Note that the reversible capacity of *a*VTO electrode is larger than that of the mixture electrode, and the voltage profile is somewhat different to each other in the first lithiation.

4.1.2.2. Valence state change of metal ions in *a*VTO during lithiation/delithiation

The redox behavior of two redox centers (V and Ti) in *a*VTO and *a*V_2O_5 + *a*TiO_2 electrodes was compared using *ex-situ* XANES spectra. Figure 10a and Figure 11a show the normalized titanium and vanadium K-edge XANES spectra obtained from *a*VTO, *a*TiO_2 and *a*V_2O_5 after the first lithiation (0.8 V) and forthcoming de-lithaition (3.0 V). To obtain the relationship between the metal valence and absorption energy, XANES data were obtained from some reference oxides; crystalline titanium oxides (*c*TiO_2 and *c*Ti_2O_3) and vanadium oxides (*c*V_2O_5, *c*VO_2 and *c*V_2O_3), the metal valence of which is the formal value (for example, 4+ for *c*TiO_2 and *c*VO_2). The valence of transition metal ions in amorphous oxides were calculated on the basis of the assumption that the metal valence has a linear relation with the position of main absorption edge. Therefore, the electron energy at the half-height of the main absorption edge was taken and plotted along with the estimated metal valence of the reference oxides. Note that the shape and position of main edge depend on not only the metal valence but also the local structure and coordination

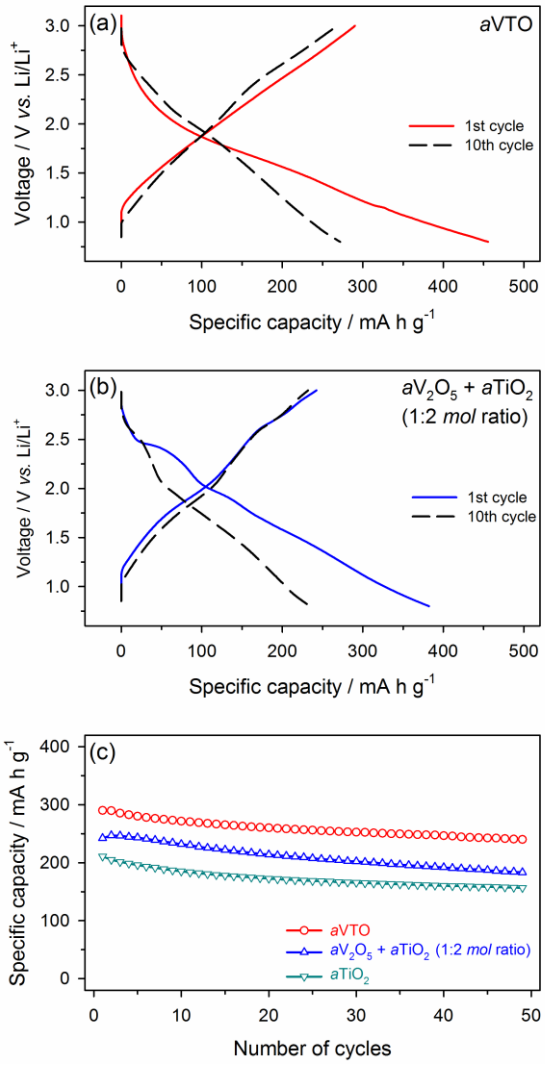

Figure 9. (a); The lithiation/de-lithiation voltage profile obtained from Li/*a*VTO cell, (b); lithiation/de-lithiation voltage profile obtained from Li/*a*V_2O_5 + *a*TiO_2 (physical mixture in 1: 2 mol ratio) cell, and (c); cycle performance of Li/*a*VTO, Li/*a*V_2O_5 + *a*TiO_2 and Li/*a*TiO_2 cells.

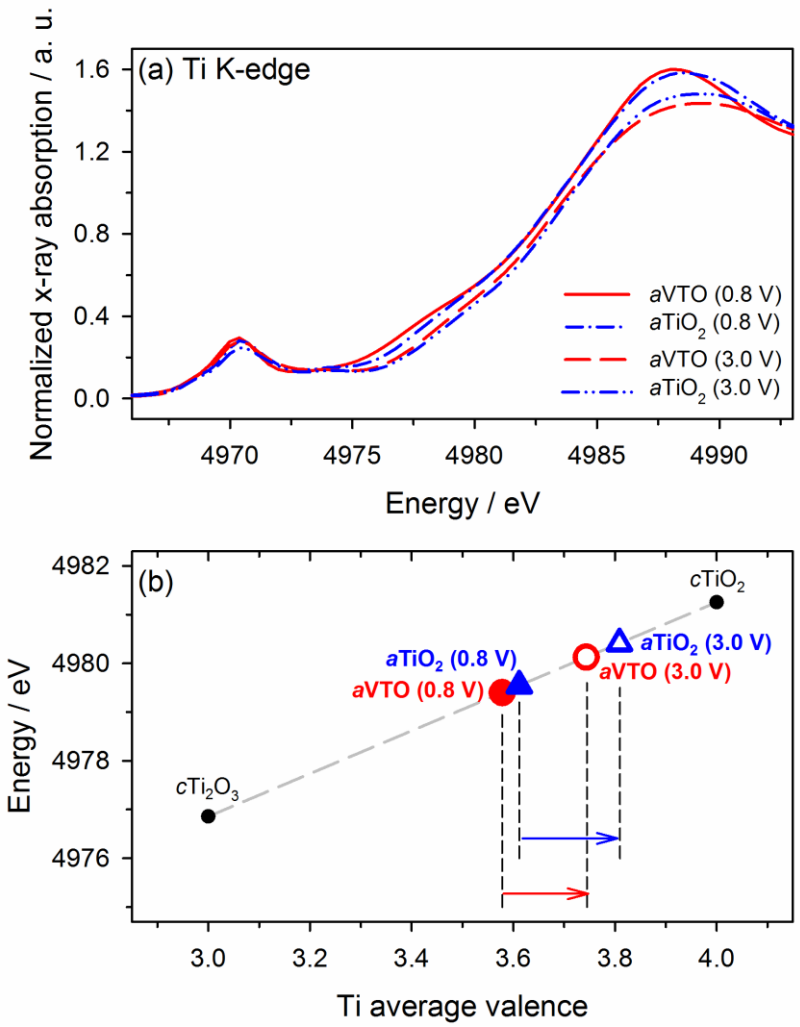

Figure 10. (a); *Ex-situ* XANES spectra of titanium K-edge for *a*TVO, *a*TiO_2 and *a*V_2O_5 electrode, which were obtained at fully lithiated state (0.8 V *vs.* Li/Li^+) and fully de-lithiated state (3.0 V) in the first cycle. (b); the metal valence change upon the first lithiation, which was derived from (a).

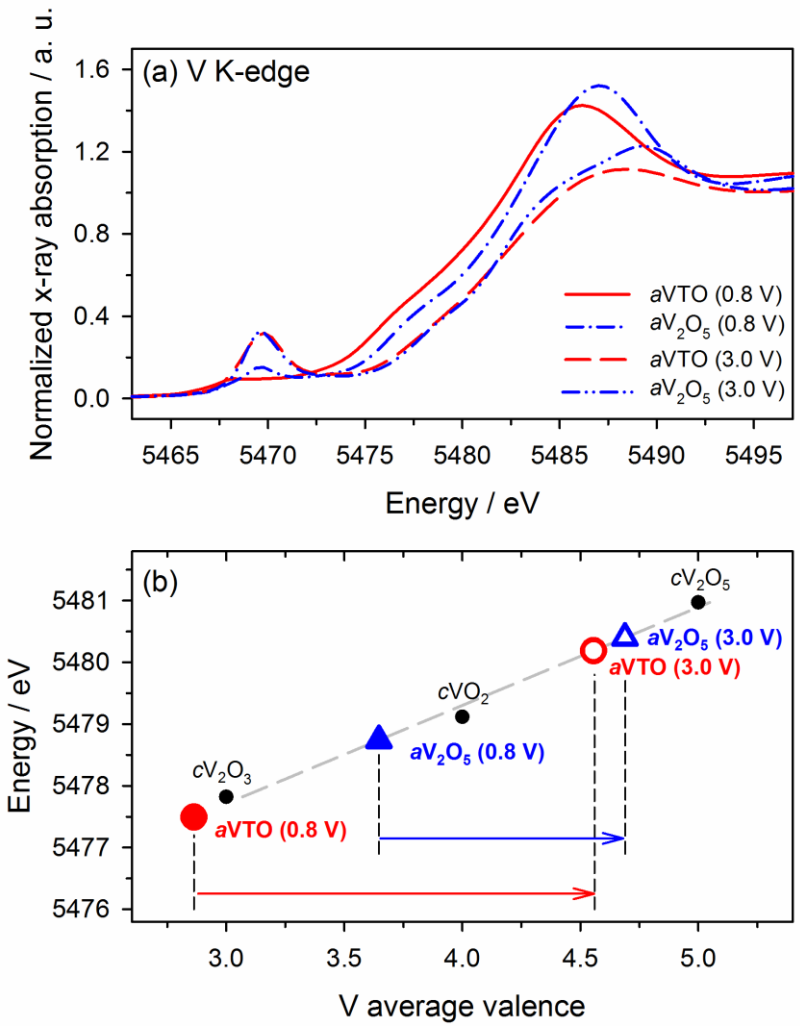

Figure 11. (a); *Ex-situ* XANES spectra of vanadium K-edge for *a*TVO, *a*TiO_2 and *a*V_2O_5 electrode, which were obtained at fully lithiated state (0.8 V *vs.* Li/Li^+) and fully de-lithiated state (3.0 V) in the first cycle. (b); the metal valence change upon the first lithiation, which was derived from (a).

of metal ions, the calculated values could be crude estimates. As is seen in Figure 10b, the Ti valence in *a*VTO changes from 3.58+ to 3.74+. A similar change is observed with *a*TiO_2 (from 3.61+ to 3.81+), illustrating that the redox behavior of Ti ions is comparable for *a*VTO and *a*TiO_2. The redox behavior of V ions in *a*VTO and *a*V_2O_5 is also examined. As is seen in Figure 11b, the V valence in *a*VTO changes from 2.7+ to 4.6+, whereas it changes from 3.6+ to 4.7+ for *a*V_2O_5. Clearly, the oxidation state of V ions in *a*VTO is lower (2.7+) compared with that for *a*V_2O_5 (3.6+) upon lithiation, illustrating that the electron accepting ability of V^{5+} ions as a redox center is higher for those in *a*VTO.

4.1.2.3. Origin of the extra capacity delivered in *a*VTO

As shown in Figure 9, the first reversible specific capacity of *a*VTO (295 mA h g^{-1}) is larger than that of the physically mixed oxide (*a*V_2O_5 + *a*TiO_2) (245 mA h g^{-1}). V K-edge spectra in Figure 11 suggest that the extra capacity (ca. 50 mA h g^{-1}) delivered by *a*VTO can be attributed to the increased electron accepting ability of the V^{5+} ions in *a*VTO. The apparent difference between *a*VTO and *a*V_2O_5 is the local structure; the V^{5+} ions in *a*VTO are four-coordinated, but five-coordinated in *a*V_2O_5. The experimental data suggest that the difference in local structure of V^{5+} ions induced by homogeneous mixing of Ti and V affected the chemical potential of Li^+ storage sites of the material. Namely, *a*VTO should carry both Li^+ storage sites and redox centers for lithiation. Both are limiting factors for overall Li storage capacity. Hence, this phenomena based on two different aspects which are electronic structure (electron accepting ability) and atomic structure (extra Li^+ storage sites) modification. First, if *a*VTO has plenty Li^+ storage sites (structural defects), which is likely since it is amorphous, the number of redox centers (number of electrons to be stored) determines the overall Li storage capacity. That is, if the overall capacity is limited by the number of redox centers, the change of electronic band structure

in *a*VTO introduced by modification of local geometry or homogeneous mixing of cations can enlarge the Li storage capacity. The similar phenomena can be observed from the Co^{3+} ions having a different redox behavior depending on their surrounding environments in spinel $LiMn_{2-x}Co_xO_4$ and layered $LiCoO_2$.[76] Considering that the V or Ti substitution in TiO_2 and V_2O_5 may alter the electronic band structures of their original framework,[77,78] it is a natural consequence that V ions in V−Ti−O structure have a different redox behavior with that of V_2O_5. However, because of difficulty in analyzing band structure of amorphous materials, it is still unclear why the V ions in *a*VTO show a higher electron accepting ability. The second possibility is the reverse case. Here, if the number of Li^+ storage sites is smaller than that of redox centers, the overall capacity is decided by the former. If this is the case in *a*VTO, the larger specific capacity of *a*VTO over the mixed electrode (aV_2O_5 + $aTiO_2$) can be accounted for by the generation of extra Li^+ storage sites (structural defects) by the addition of V^{5+} ions into the $aTiO_2$ matrix. This possibility has been proposed in previous literature.[62,63]

4.1.3. Performance improvements of *a*VTO via modification of synthetic atmosphere

4.1.3.1. Poor initial Coulombic efficiency of *a*VTO

As shown voltage profiles in Figure 9a and differential capacity plots in Figure 12, the Li/*a*VTO cell shows a large irreversible capacity in the first cycle, which diminishes in the forthcoming cycles. The major irreversible reactions take place at <2.0 V as indicated by an arrow in Figure 12. Two possibilities exist for the irreversible reactions; electrolyte decomposition, and Li reaction with residual water or surface hydroxyl groups. The former possibility is discarded because the electrolyte decomposition is commonly

observed at 0.7 – 0.8 V (*vs*. Li/Li^+). The latter possibility seems to be more probable because the amorphous samples can carry residual water and surface hydroxyl groups since they were prepared by drying at 300°C under vacuum. The following irreversible reactions can be assumed:[64,65]

$$H_2O + 2Li^+ + 2e^- \rightarrow LiOH + \frac{1}{2}H_2 + Li^+ + e^- \rightarrow Li_2O + H_2$$

Equation 4-1

$$OH + 2Li^+ + 2e^- \rightarrow LiOH + Li^+ + e^- \rightarrow Li_2O + \frac{1}{2}H_2$$

Equation 4-2

4.1.3.2. Surface analysis of *a*VTO

This is validated on the XPS spectra obtained from the *a*VTO electrode before and after lithiation (Figure 13a). The O 1s spectra obtained before lithiation were deconvoluted into three peaks. The peak at 530.7 eV is assigned to the bulk oxygen of amorphous metal oxides. The O 1s photoelectrons at 532.7 eV and 534.0 eV come from the oxygen in hydroxyl groups and adsorbed water on the metal oxide surface, respectively.[79] The presence of hydroxyl and bulk-trapped water can also be observed in FTIR-ATR spectra shown in Figure 14.

The O 1s spectra obtained after lithiation (Figure 13b) were fitted with four peak according to the reported binding energies; Li_2O at 528.5 eV, LiOH at 531.5 eV, Li_2CO_3 and oxygen atoms doubly bound to carbon atoms at 532 eV and oxygen bound to carbon with a single bond at 533.5 eV.[80,81] A large amount of Li_2O and LiOH is found on the surface of lithiated *a*VTO. Clearly, the surface hydroxyl groups and residual water in *a*VTO are converted into Li_2O and LiOH according to the above irreversible reactions, which appear as the irreversible capacity in Figure 9a and Figure 12.

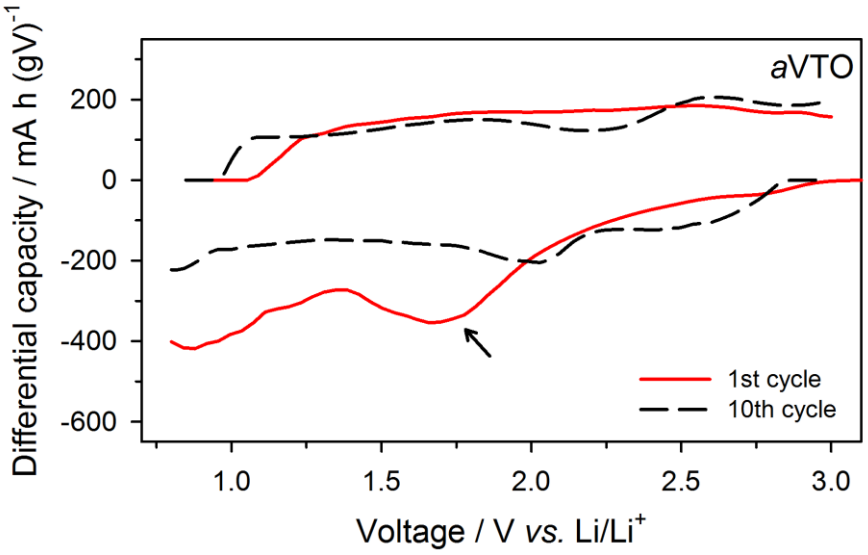

Figure 12. Differential capacity plots derived from the lithiation/de-lithiation voltage profile of Li/*a*VTO cell.

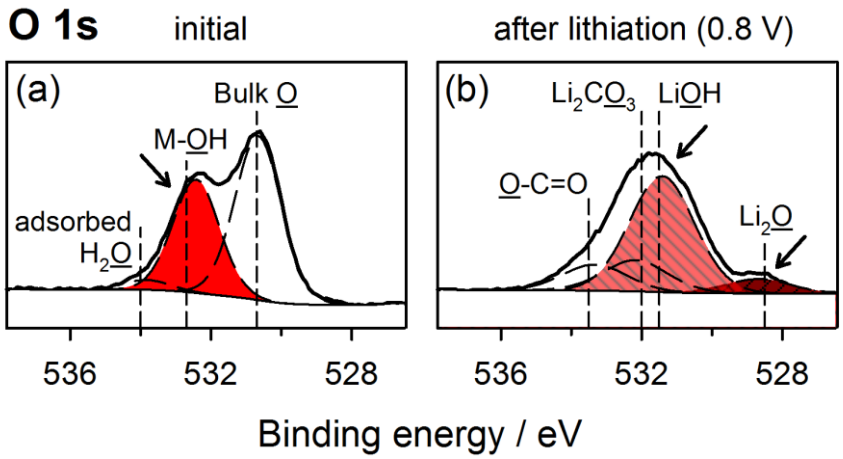

Figure 13. X-ray photoelectron spectra (XPS) of oxygen 1s: (a); *a*VTO in the initial open circuit voltage (OCV) state, (b); *a*VTO after lithiation down to 0.8 V.

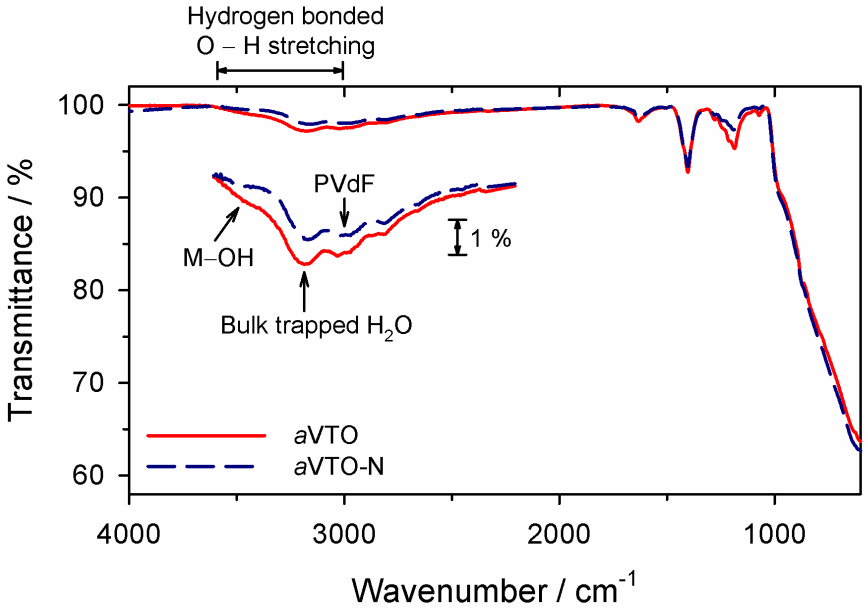

Figure 14. Fourier Transform Infrared (FTIR)-Attenuated Total Reflectance (ATR) spectra measured in vacuum for *a*VTO and *a*VTO-N with PVdF binder.

4.1.3.3. Influences of the surface hydroxyl groups and the bulk-trapped water on electrolyte solution

Meanwhile, it might be concerned that hydroxyl groups and residual water decompose the electrolyte, because it is well known that water in electrolytes can hydrolyze lithium hexafluorophosphate ($LiPF_6$) to produce hydrogen fluoride (HF). Thus, it is likely that both bulk-trapped water and surface hydroxyl groups can hydrolyze $LiPF_6$. To validate this possibility, a control experiment was performed, in which 0.1 g of powder samples that were dried overnight at 120°C in vacuum were stored in 5 ml of 1 *M* $LiPF_6$ in EC: DMC (1: 2) electrolyte for 3 days. Then, HF concentration in the electrolyte was measured by an acid-base titration. As shown in the Figure 15, the used electrolyte (1 *M* $LiPF_6$ in EC: DMC) contains about 32.3 ppm of HF (bare electrolyte). The electrolytes that were stored with the oxide samples (*a*VTO or *a*VTO-N) at 25°C for 3 days show a comparable HF concentration (33.0 ppm). However, HF concentration was 365 ppm in the electrolyte stored after adding 100 ppm water. These results illustrate that HF is generated by the hydrolysis of $LiPF_6$, but neither the surface hydroxyl groups nor bulk-trapped water participate in the hydrolysis reaction.

4.1.3.4. Characteristics of amorphous vanadium titanate synthesized under N_2 atmosphere

The morphology and bulk properties of *a*VTO-N are very similar to those of *a*VTO (Figure 16 to Figure 19) even if the surface area is larger for *a*VTO-N (Table 1). The metal valence is not changed even if the reaction atmosphere is changed from air to nitrogen (Figure 18). On the other hands, the population of surface hydroxyl groups is much smaller than that in *a*VTO as shown in the O 1s XPS spectra obtained from the pristine *a*VTO-N electrode (Figure 20a). The major O 1s photoelectrons are emitted from the

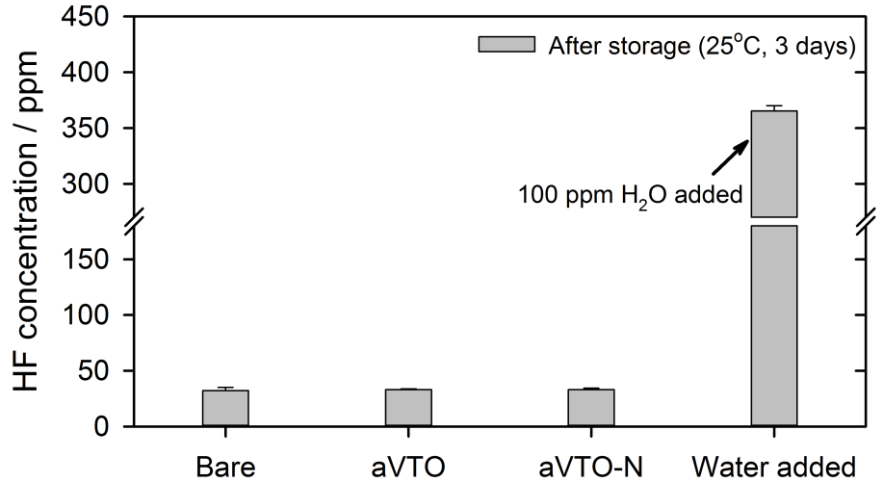

Figure 15. Hydrogen fluoride (HF) concentration in the electrolyte after storage of *a*VTO, *a*VTO-N electrodes and 100 ppm of water at 25°C for 3 days

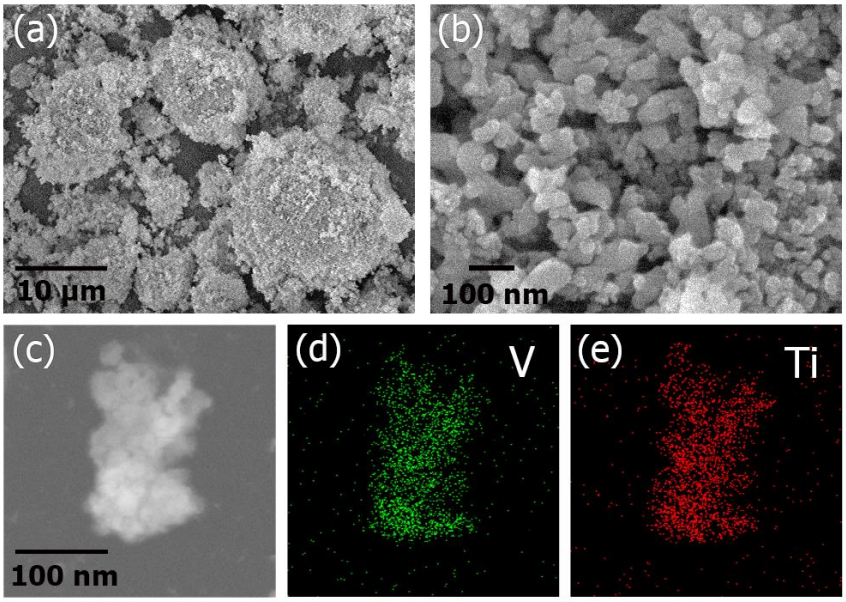

Figure 16. (a) and (b); FE-SEM images of *a*VTO-N, (c); STEM image of *a*VTO-N, and (d) and (e); the EDS mapping for vanadium and titanium.

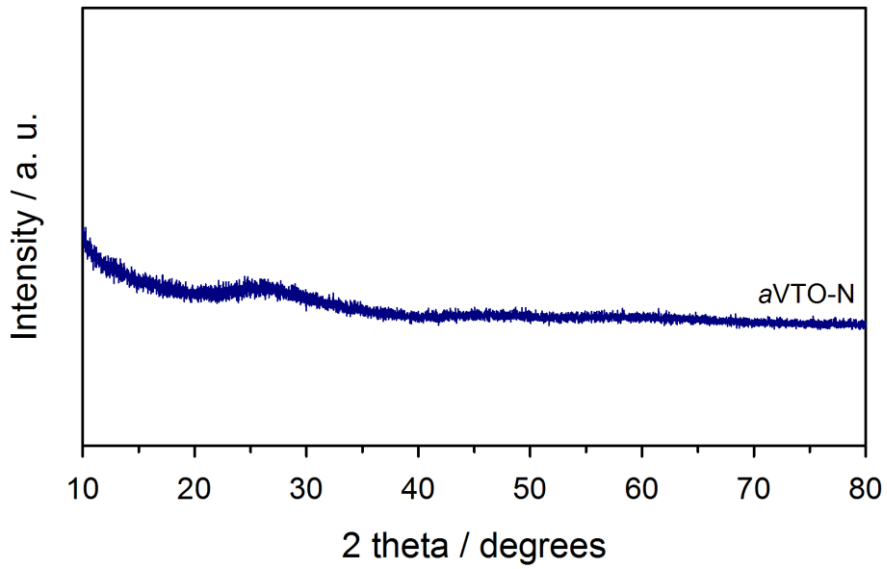

Figure 17. X-ray diffraction (XRD) pattern of *a*VTO-N powder dried at 300ºC under vacuum.

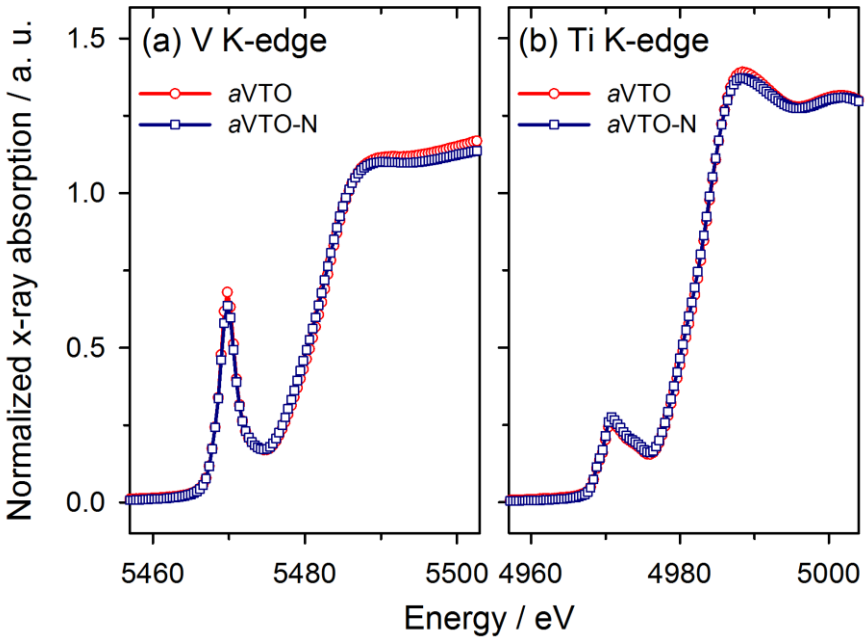

Figure 18. Comparison of the X-ray absorption near-edge structures (XANES) data for *a*VTO and *a*VTO-N: (a); vanadium K-edge and (b); titanium K-edge.

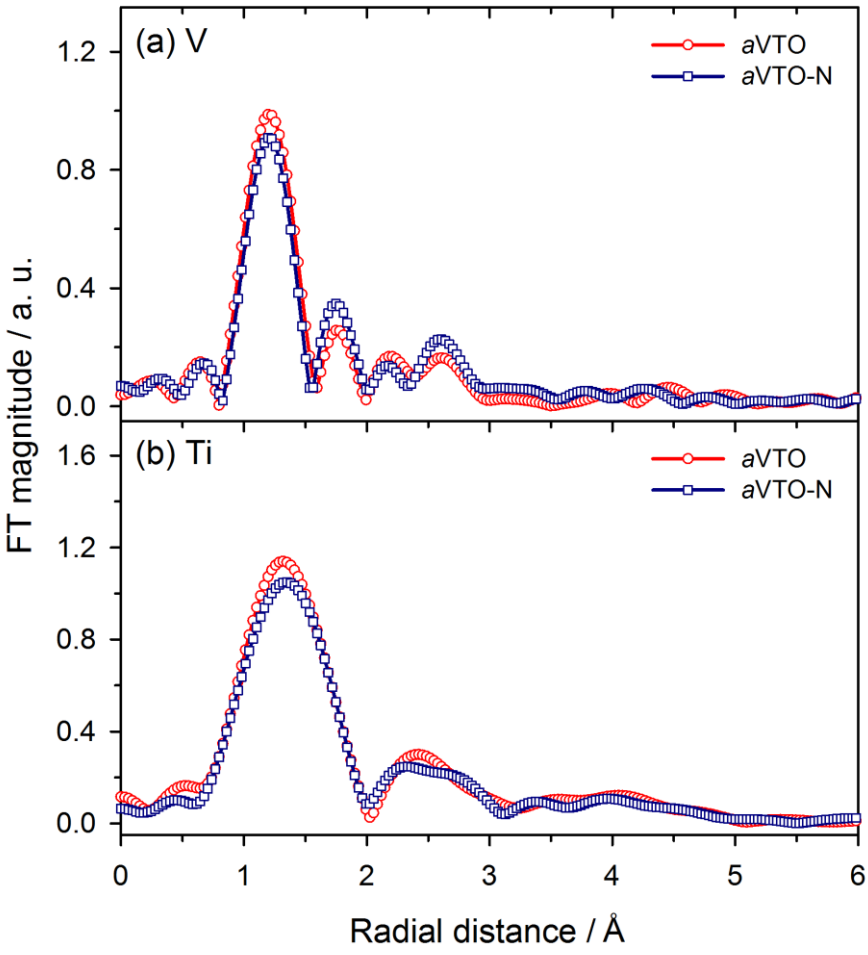

Figure 19. Comparison of the Fourier transformed extended X-ray adsorption fine structure (EXAFS): (c); vanadium K-edge and (d); titanium K-edge for *a*VTO and *a*VTO-N.

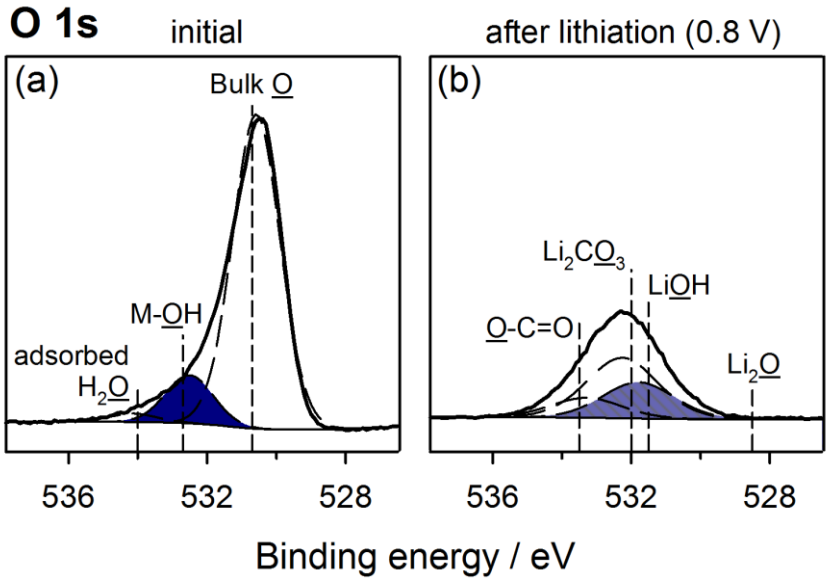

Figure 20. X-ray photoelectron spectra (XPS) of oxygen 1s: (a); aVTO-N in the initial open circuit voltage (OCV) state, (b); aVTO-N after lithiation down to 0.8 V.

lattice (bulk) oxygens. The reduced amount of those impurities can be observed from the thermogravimetric (TG) data in Figure 21. The only difference between two samples is the synthetic atmosphere; air and nitrogen.

4.1.3.5. Reasons for the reduced amount of surface hydroxyl groups on *a*VTO-N

It is curious how a larger amount of surface hydroxyl group forms in oxygen-excess condition. The following reaction is proposed. In oxygen-excess condition, molecular oxygen can be converted into the lattice oxygen, which is accompanied by a generation of metal vacancies and holes as described in Equation 4-3. In the presence of water, the lattice oxygen and holes further react with water to generate surface hydroxyl groups as shown in Equation 4-4.[82]

$$\frac{9}{2}O_2 \rightarrow 2V_{Ti}^{''''} + 2V_V^{''''} + 9O_O^{\times} + 18h^{\bullet} \qquad \textbf{Equation 4-3}$$

$$2V_{Ti}^{''''} + 2V_V^{''''} + 9O_O^{\times} + 18h^{\bullet} + 9H_2O \rightarrow 2V_{Ti}^{''''} + 2V_V^{''''} + 18OH_O^{\bullet} \qquad \textbf{Equation 4-4}$$

If this is the case, the reduced population of surface hydroxyl groups on *a*VTO-N, which was synthesized under N_2 atmosphere and thus was not contacted with oxygen, can be rationalized.

4.1.3.6. Increase in the initial Coulombic efficiency (ICE)

As shown in Figure 22a, the electrode performance of the Li/*a*VTO-N cell including reversible capacity and cycleability is also comparable to those of Li/*a*VTO. The notable difference is the irreversible capacity in the first cycle. The irreversible capacity appeared

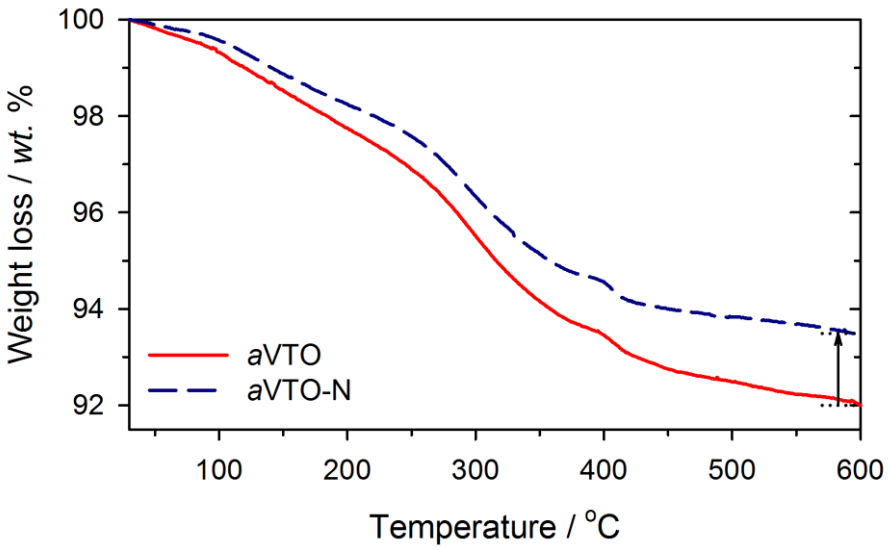

Figure 21. Thermogravimetric (TG) data of *a*VTO and *a*VTO-N under N_2 atmosphere.

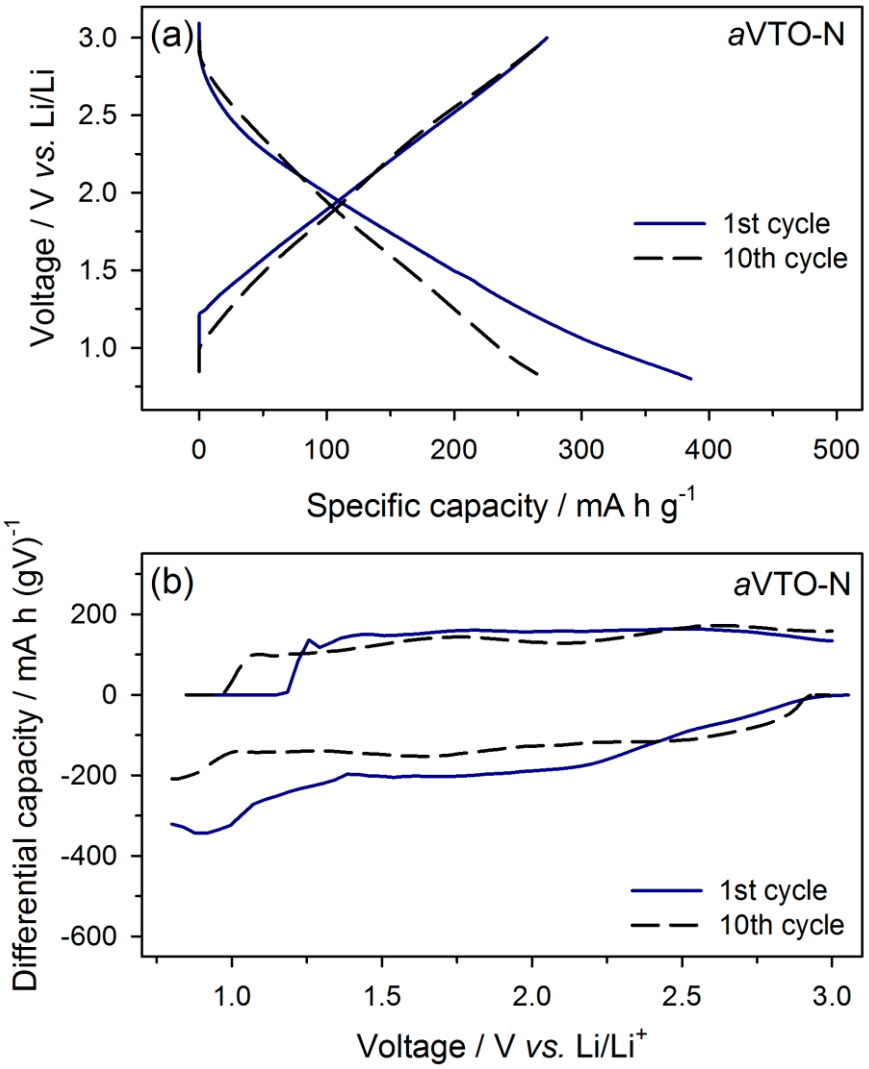

Figure 22. (a); The lithiation/de-lithiation voltage profile obtained from the Li/*a*VTO-N cell, (b): differential capacity plot derived from (a).

at < 2.0 V in the Li/*a*VTO cell (Figure 12) is notably diminished in the Li/*a*VTO-N (Figure 22b). As a result, the Coulombic efficiency of Li/aVTO-N cell was 70.7 % in the first cycle, which is higher than that for Li/*a*VTO cell (65.7%) as shown in Figure 23. Furthermore, the Li/aVTO-N cell shows higher Coulombic efficiency in the later cycles, indicating that the side reactions induced by the surface hydroxyl groups are diminished.

4.1.3.7. Enhanced rate capability

The Li/*a*VTO-N cell outperforms the Li/*a*VTO cell with respective to rate capability (Figure 24). As pointed out above, the only difference between two electrodes is the amount of surface hydroxyl groups, thus the difference in rate property should be explained on the basis of the amount of surface hydroxyl groups. As shown in Figure 20b, inorganic components such as Li_2O and LiOH, which are known to impede Li^+ diffusion,[83] are greatly diminished on the *a*VTO-N electrode. This must be due to the depletion of surface hydroxyl groups on *a*VTO-N. As a result, the formation of highly resistive inorganic compounds (Li_2O and LiOH) is greatly suppressed during the cell cycling. This result implies that, especially for the nano-sized materials which has a short Li^+ ion diffusion path, optimizing the surface characteristic to lower the interfacial resistance of Li^+ diffusion takes a crucial role in increasing the rate performance of the electrodes. In short, a lower population of surface hydroxyl groups on *a*VTO-N is responsible for the decrease of irreversible capacity and the enhanced rate capability for the Li/*a*VTO-N cell.

4.1.3.8. Significant advances of amorphous vanadium titanates

As presented in Table 2, *a*VTO-N have its superiority over other titanates or vanadates in its large specific capacity resulted from the novel structure.[84,85] Even though it

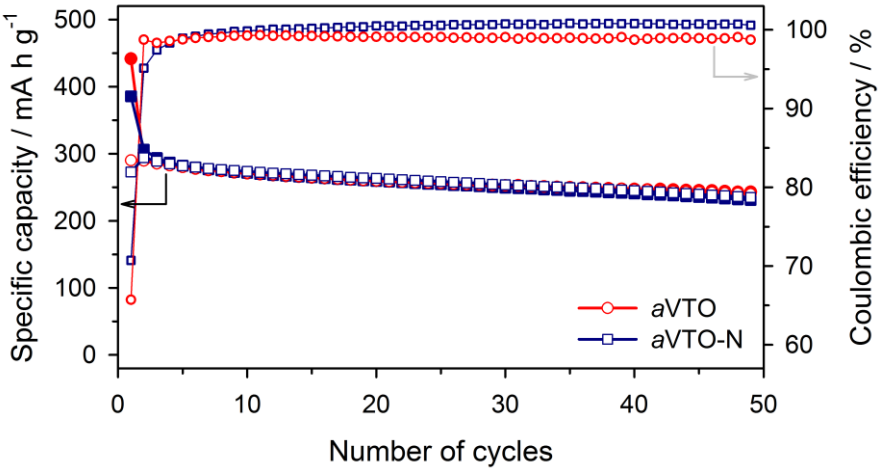

Figure 23. Comparison of the cycle data and Coulombic efficiency for Li/*a*VTO cell and Li/*a*VTO-N cell.

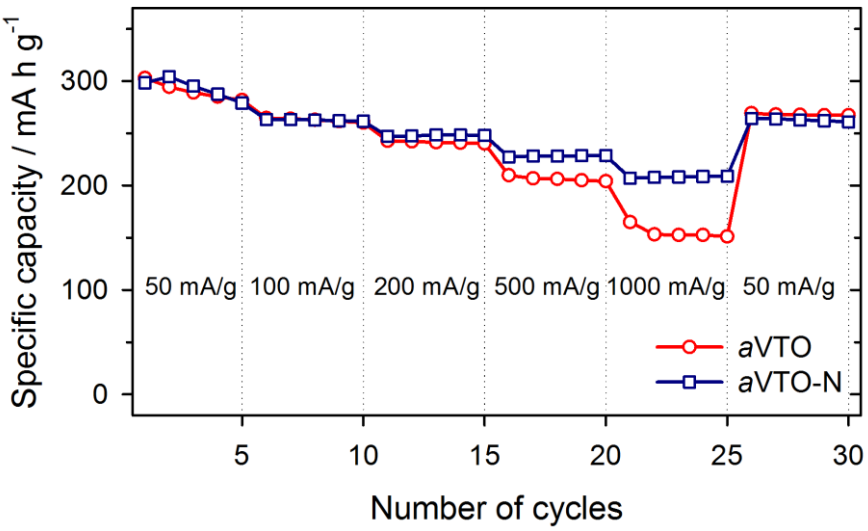

Figure 24. Comparison of the rate performance of Li/*a*VTO cell and Li/*a*VTO-N cell.

has a relatively higher working potential for negative electrodes, its large specific capacity can compensate the energy loss in full-cell configuration. Combined with positive electrodes such as $LiNi_{0.5}Mn_{1.5}O_4$ (LNMO) which has a high working potential of 4.7 V, the energy density of *a*VTO-N/LNMO full cell is 1.5 times larger than that of LTO/LNMO full cell as shown in Figure 25.

4.1.4. Summary of Section 4.1.

In Section 4.1, in order to increase the specific capacity of insertion-type electrode materials such as amorphous titanium dioxide ($a TiO_2$) electrode, V^{5+} ions are incorporated into the $a TiO_2$ matrix. The prepared amorphous vanadium titanate (*a*VTO) was not dispersed in atomic scale. As a result, the V^{5+} ions in *a*VTO were located at the four-coordination sites, which is contrasted by the five-coordinated V^{5+} ions in $a V_2O_5$. However, five-fold coordination of Ti^{4+} ions was not changed in *a*VTO. All those oxide electrodes showed a sloping charge/discharge voltage profile, which is a characteristic feature of amorphous electrodes. Li^+ storage at structural defects (vacancies, void spaces, cluster gaps, or interstitial sites) can thus be assumed. The reversible specific capacity of *a*VTO was increased compared to that of $a TiO_2$ due to the incorporation of V ions, which are more electron acceptable compared to Ti ions. The capacity of *a*VTO was even larger than that for the physically mixed ($a V_2O_5$ and $a TiO_2$ in the stoichiometric ratio) electrode. The extra capacity delivered by *a*VTO has thus been ascribed to the contribution from the homogenous mixing of V and Ti ions in *a*VTO. Two possibilities are proposed for this contribution. One is the modification of electronic structure in *a*VTO to cause a change in the redox behaviors of V ions in *a*VTO. The other is the creation of extra Li^+ storage sites (structural defects) by the incorporation of V^{5+} ions into the $a TiO_2$ matrix. a physical mixture of $a V_2O_5$ and $a TiO_2$. The V^{5+} and Ti^{4+} ions were homogeneously

Table 2. The potential range, average working potential and specific capacity of *a*VTO-N, titanate and vanadate materials for negative electrodes.

Materials	Potential range (Avg. working potential) (V vs. Li/Li^+)	Specific capacity* (mA h g^{-1})	References
$Li_4Ti_5O_{12}$	1.0 – 2.5 V (1.7 V)	175	Theoretical specific capacity
***a*VTO-N**	**0.8 – 3.0 V (2.0 V)**	**300**	**This work**
Li_3VO_4	0.1 – 2.0 V (1.2 V)	215	*Journal of Power Sources*, **244**, 557–560, (2013).
$Li_{1+x}V_{1-x}O_2$	0.01 – 2.0 V (0.4 V)	210	*Materials Chemistry and Physics*, **116**, 603–606, (2009).

* Specific capacity obtained upon cycling at 0.2 *C*-rate in the second cycle

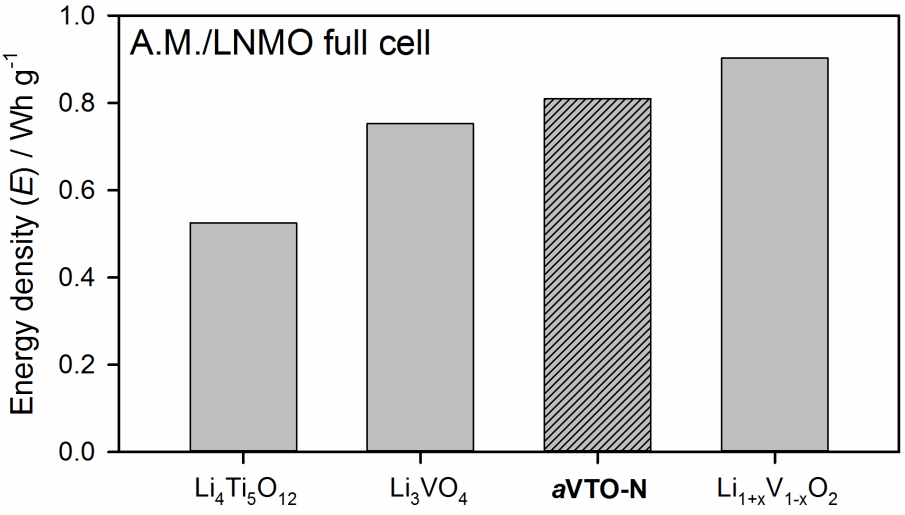

Figure 25. The energy density calculated for the full-cells fabricated with the $LiNi_{0.5}Mn_{1.5}O_4$ (LNMO) positive electrode.

The surface hydroxyl groups and residual water in *a*VTO, which cause a serious irreversible reaction and formation of highly resistive inorganic species, was greatly reduced by nitrogen purging during synthetic process. The amorphous vanadium titanate prepared under nitrogen (*a*VTO-N) outperforms the one prepared under air on the aspect of Coulombic efficiency and rate property.

4.2. Conversion-type lithium storage in lithium metavanadate ($LiVO_3$) and its performance improvements

Conversion reactions have not been observed for transition metal oxides in groups 4 and 5 (Ti and V in 3d transition metals). As can be observed in Figure 26, however, the full reduction of V_2O_5 to vanadium metal theoretically holds the promise of the highest capacity (1474 mA h g^{-1}; cf. MnO_2: 1233 mA h g^{-1}, MoO_3: 1117 mA h g^{-1}) because vanadium is lighter than other transition metal ions and have higher valence state of 5+. Moreover, if the conversion reaction of vanadium oxides occurs, it can potentially show its largest specific capacity at a lower potential near 0 V (*vs.* Li/Li^+) as shown in Figure 27, resulting in higher energy density compared to other conversion-type metal oxides. Vanadium pentoxide, V_2O_5, which has been studied for insertion-type electrode materials for LIBs,[61,86] is lithiated with conversion reaction showing long voltage plateau near 0.0 V (*vs.* Li/Li^+) only when it was cycled at elevated temperature (Figure 28 and Figure 29). This phenomenon implies that the conversion reaction of vanadium oxides is thermodynamically feasible above the Li plating potential but kinetically hindered.

This work finds that $LiVO_3$ is lithiated by a conversion reaction at ambient temperature, which is unusual for vanadium oxides as observed from the lithiation reactions of V_2O_5, $Li_{1+x}V_{1-x}O_2$ and Li_3VO_4.[85,87,88]. The major object of this work was to identify the reaction mechanism of $LiVO_3$ and the nature of the thermodynamics and kinetics in the conversion-type reactions of vanadium oxides. $LiVO_3$ delivers a large reversible capacity with a conversion reaction at room temperature near 0.0 V (*vs.* Li/Li^+). In addition to identifying the reaction mechanism of this material, electrochemical analysis, several *ex-situ* techniques and *ab-initio* calculations were used to investigate its structural changes upon Li^+ storage. Furthermore, to clarify the unexpected feature of

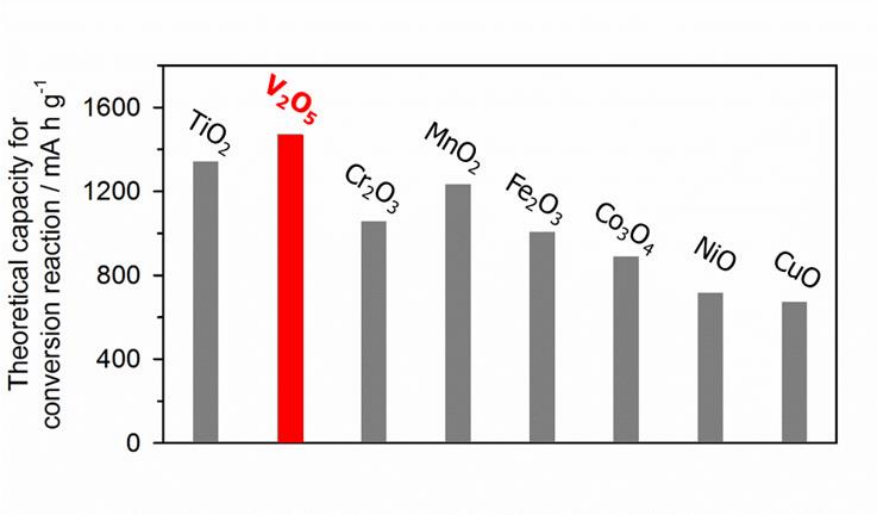

Figure 26. Theoretical specific capacities of conversion-type reaction of 3d transition metal oxides.

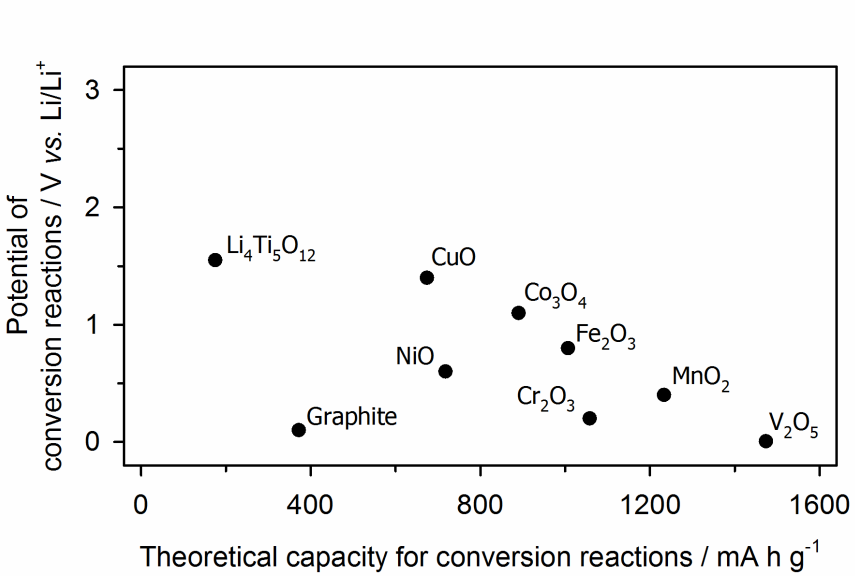

Figure 27. Plots of the empirical reaction potential and theoretical specific capacities for conversion-type lithiation in 3d transition metal oxides estimated from Figure 2 and Figure 26.

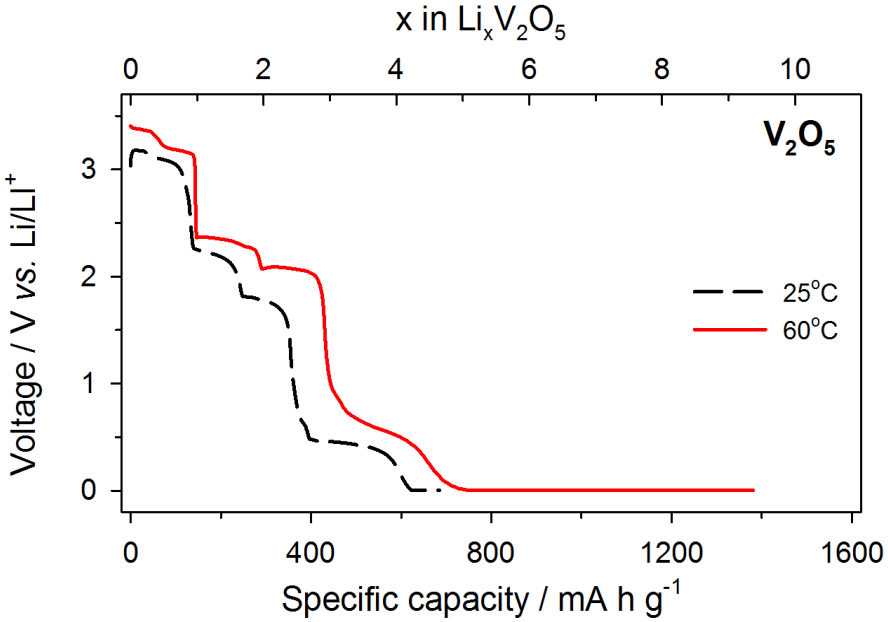

Figure 28. Galvanostatic lithiation voltage profiles of Li/V_2O_5 cell at 25°C and 60°C.

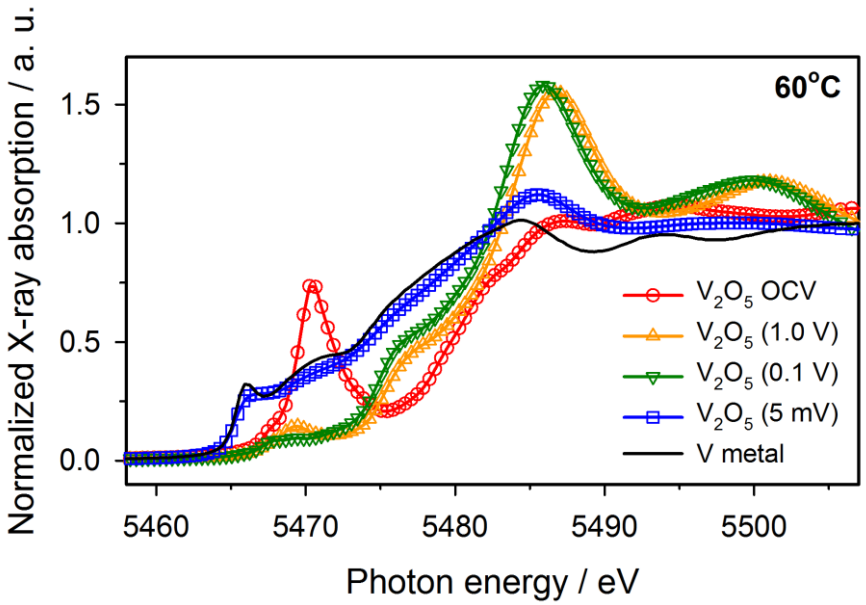

Figure 29. Normalized vanadium K-edge XANES spectra obtained from the V_2O_5 electrodes in the first lithiation period at 60°C.

$LiVO_3$, a comparative study was performed with vanadium pentoxide (V_2O_5). Note that $LiVO_3$ is lithiated by the conversion reaction at room temperature but V_2O_5 is not. From the comparative studies made for $LiVO_3$ and V_2O_5, the factors enabling the conversion reaction for $LiVO_3$ at ambient temperature have been extracted. Furthermore, from the quasi-open-circuit voltage (QOCV) obtained from the galvanostatic intermittent titration technique (GITT) and the resistance values obtained from electrochemical impedance spectroscopy (EIS) measurements, the thermodynamically determined quasi-equilibrium potential and kinetic barriers for the conversion reactions were derived and then compared for the two vanadium oxide electrodes. Another objective of this work is to further increase the performance of the $LiVO_3$ electrode by modifying the chemistry of the material. In order to do so, copper vanadate (CuV_2O_6) was introduced. CuV_2O_6 has been studied as a positive electrode materials because it produces metallic Cu, which is known for enhancing kinetic properties of electrodes, upon lithiation.[89–91] However, it was applied as a negative electrode material in this work, showing a novel electrochemistry which generates Cu/$LiVO_3$ nanocomposite upon the first cycle. The effects of *in-situ* generation of Cu/$LiVO_3$ nanocomposite on its cycle life were comprehensively examined.

4.2.1. Material characterization of lithium metavanadate ($LiVO_3$)

Figure 30 shows the FE-SEM images obtained from the synthesized $LiVO_3$ powder. As shown in Figure 30a, its size was larger than 10 microns, 1 h of ball-mill process was followed to make particles small and uniform in size. The XRD patterns in Figure 31 confirmed that the synthesized $LiVO_3$ powder is a monoclinic structure with *C*2/*c* space group (JCPDS No. 33-0835) and the crystal structure is maintained after ball-milling.

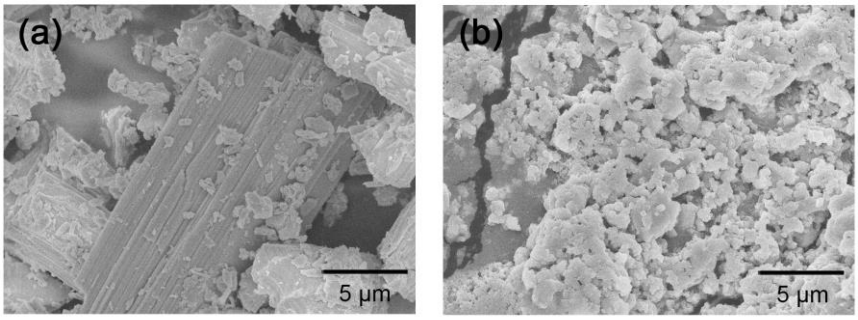

Figure 30. FE-SEM images of as-prepared $LiVO_3$ (a) and ball-milled $LiVO_3$ for 1 h (b).

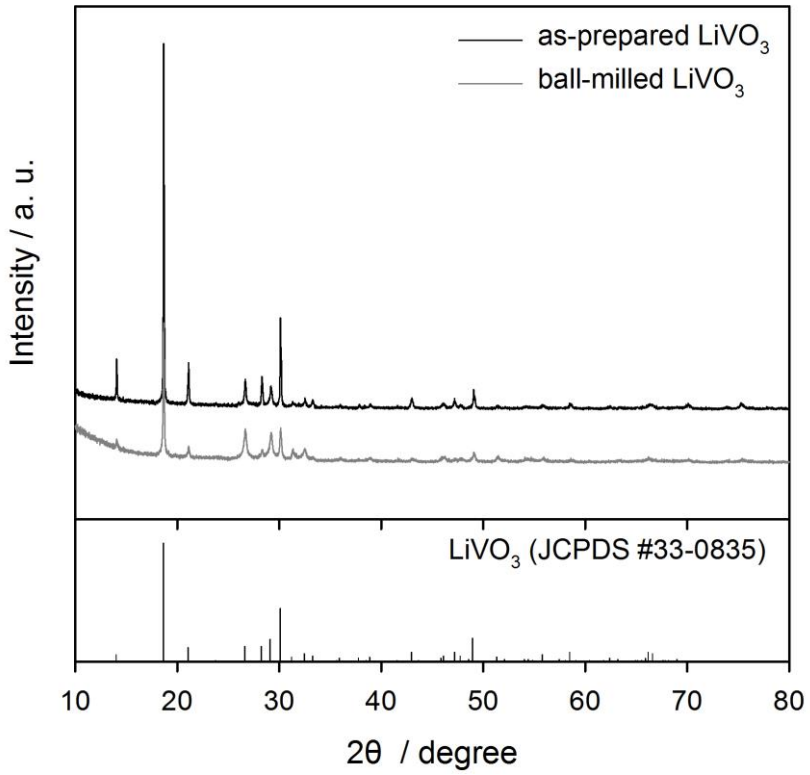

Figure 31. XRD patterns of as-prepared $LiVO_3$ (black) and ball-milled $LiVO_3$ for 1 h (grey).

4.2.2. Electrochemical properties and *ex-situ* analysis

4.2.2.1. Galvanostatic lithiation/delithiation

Figure 32 shows the galvanostatic lithiation and de-lithiation voltage profiles of $LiVO_3$ at room temperature. In the first cycle, $LiVO_3$ delivers a lithiation capacity up to 1300 mA h g^{-1}, which corresponds to lithiation of more than five Li^+ ions at roughly three different potential regions, and delithiation capacity of 1043 mA h g^{-1}. An apparent feature is that $LiVO_3$ takes about 3.5 Li^+ ions/electrons at the potential region of 0.005 V, which is hardly observed in other vanadium oxides. Moreover, a high reversible capacity is delivered continuously in the second cycle and thereafter. However, the specific capacity of the Li/$LiVO_3$ cell continuously decreases in early stage of cycling as can be seen in the inset of Figure 32. Failure mode of the $LiVO_3$ electrode will be further discussed in Section 4.2.6.1.

4.2.2.2. Electrochemical analysis on $LiVO_3$

The potential intermittent titration technique (PITT) and electrochemical voltage spectroscopy (EVS) were performed to examine the reactions occurring at the $LiVO_3$ electrodes more in detail. The chronoamperogram obtained from the successive potential step provides information whether the reaction is governed by single-phase diffusion or two-phase (nucleation and growth) reaction. According to the EVS profile derived from the PITT shown in Figure 33a, lithiation in $LiVO_3$ can be divided into three stages: A, B, and C. The current measured at stage A (1.5 – 1.8 V) shows a bell-shape transient, which suggests lithiation at this potential region proceeds by a two-phase reaction.[92] Stage B is related to the diffusion of Li^+ ions in the solid-solution phase, inferred from the sloping voltage profile and the current transient, which monotonically decays when a potential

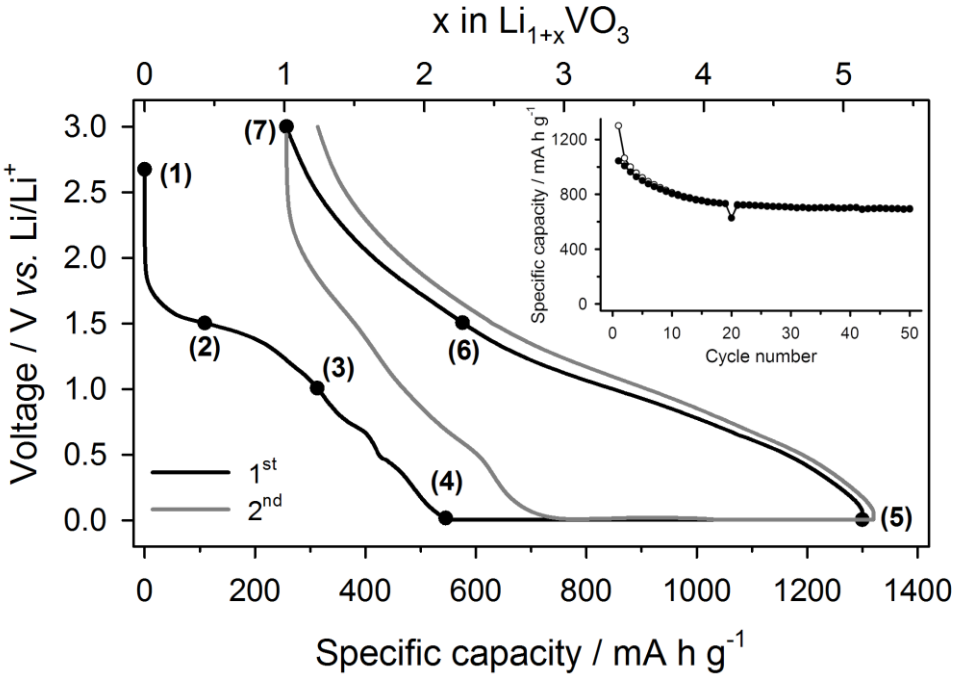

Figure 32. The galvanostatic lithiation/de-lithiation voltage profiles of Li/$LiVO_3$ cell. The numbers indicate the state of lithiation/de-lithiation where the *ex-situ* XANES experiments were performed. The inset shows the cycle performance.

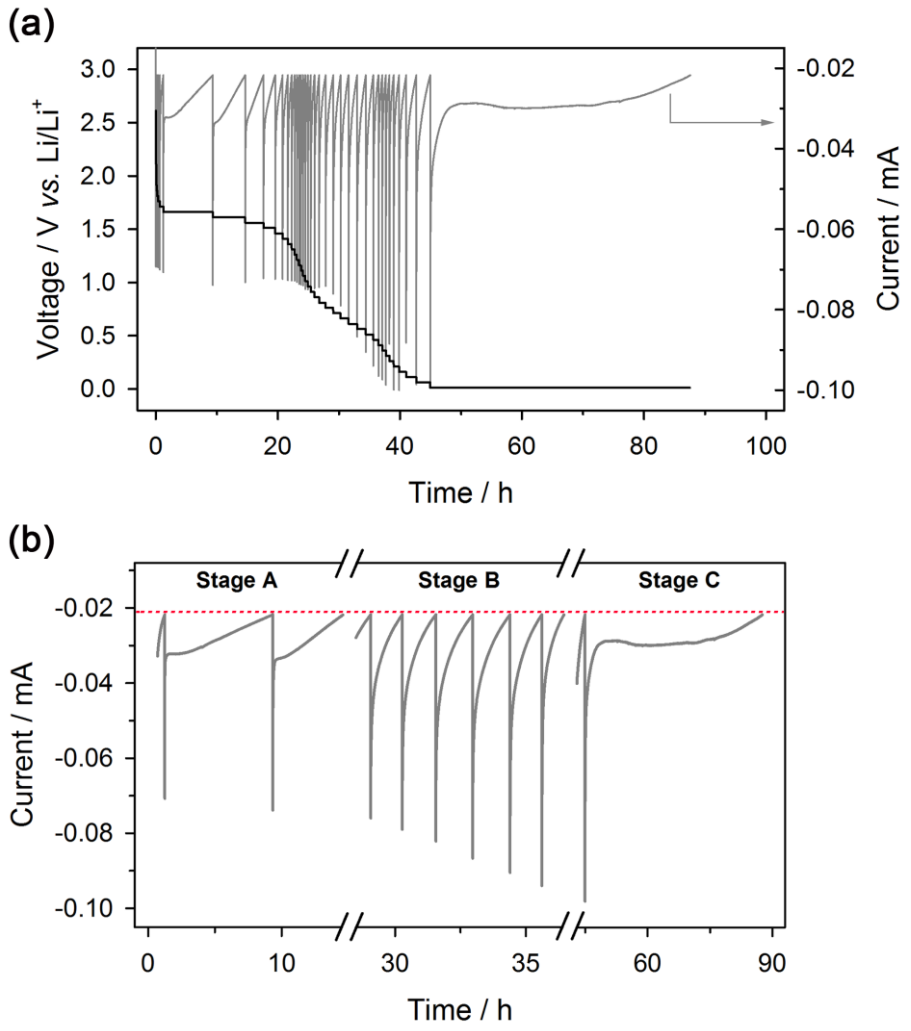

Figure 33. The potentiostatic intermittent titration technique (PITT) measurement obtained from Li/$LiVO_3$ cell in the first lithiation (a) and the enlarged views for the current transients at three stages (b). The voltage and current in (a) are in black and gray, respectively. Note that the current has a negative value because it is a reduction current.

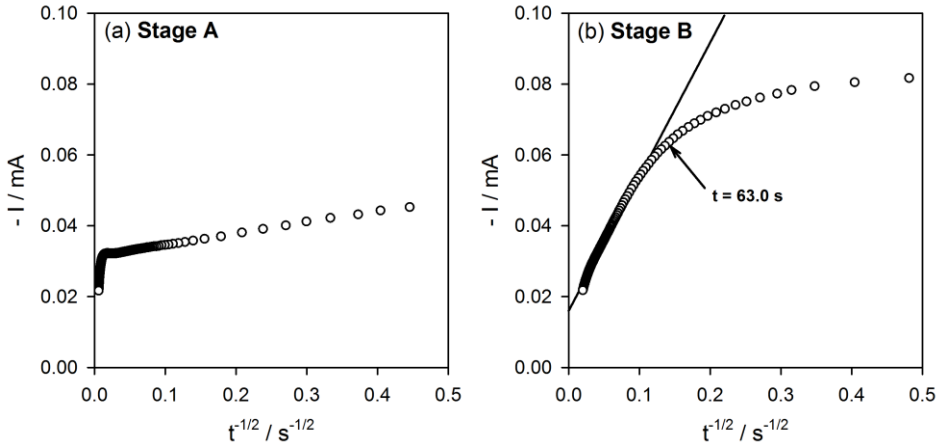

Figure 34. Current versus $t^{-1/2}$ plots for the current transient in stage *A* and *B* obtained from PITT measurement.

step is applied. The current decay in stage B has been fitted with the Cottrell equation (Equation 4-5) and compared to that for stage A to decide if the process is controlled by diffusion or not (Figure 34).[93]

$$I(t) = \frac{nFAD^{1/2}C}{\pi^{1/2}t^{1/2}} \qquad \textbf{Equation 4-5}$$

Unlike stage A, the current transient in stage B follows the Cottrell equation in the later period. The discrepancy in the early stage (Figure 34b) can be accounted for by the double-layer charging.[94] Based on all those aspects, Li^+ storage in stage B occurs with single-phase insertion-type reaction. The most remarkable feature here is stage C, in which most of Li^+ ions are lithiated at the long and distinct plateau near 0 V. From the PITT measurement showing a bell-shaped current transient as seen in stage A, Li^+ storage at stage C is a two-phase reaction as well.[92] Being kinetically unfavorable, this reaction is observed only when constant-voltage charging or constant-current charging is at an extremely low current density in the first cycle. However, the reaction at stage C can proceed even in constant-current charging mode at normal condition from the second cycle. This activation process, which has been reported in several previous studies on the conversion-type electrode materials,[95] suggests that the kinetics of this reaction is improved after the first cycle.

4.2.2.3. Structural analysis on $LiVO_3$ upon lithiation

Ex-situ XRD of $LiVO_3$ was measured to clarify the structural change during lithiation and de-lithiation. As shown in Figure 35, $LiVO_3$ is amorphized during stage A and maintain its amorphous structure in the succeeding cycles. This result is consistent with the preceding study which confirmed that $LiVO_3$ transforms from crystalline structure to a disordered Li_2VO_3 structure during lithiation.[96] Because no more crystalline diffraction

peaks appeared thereafter, detailed structural changes were examined with the synchrotron X-ray absorption spectroscopy (XAS).

4.2.2.4. Local geometry and valence state of vanadium in $LiVO_3$ electrode upon lithiation/delithiation

Figure 36 shows the vanadium K-edge XANES spectra which were collected during the first lithiation and de-lithiation to trace the valence and local structure of the vanadium in the $LiVO_3$. A strong pre-edge of the starting component, $LiVO_3$ (1), shows that the V^{5+} ion is located at a tetrahedral site of the monoclinic structure. After the insertion of one Li^+ ion (3), the intensity of the pre-edge decreases, indicating that vanadium ions move from a tetrahedral coordination to a more symmetric local structure. At the end of stage B (4), there is no significant change in the edge shape. Meanwhile, the main edge continuously shifts to a lower energy upon lithiation. The two-phase reaction at stage A and one-phase reaction at stage B can further be ascertained from the *in-situ* XAS measurement presented in Figure 37. The XAS results show a two-phase behavior between tetrahedral and octahedral vanadium at stage A, and single-phase behavior of vanadate structure at stage B. At the end of lithiation (5), the energy and shape of the vanadium K-edge come close to that ofmetallic V. In short, the vanadium ions are reduced to the elemental state after full lithiation. At the end of lithiation (5), the energy and shape of the vanadium K-edge become close to that for vanadium metal and V−V metallic bond is observed in the EXAFS spectra (Figure 36c). The formation of nano-sized metallic vanadium particles dispersed in the amorphous Li_2O matrix upon lithiation was ascertained from the HR-TEM images and SAED patterns (Figure 38).

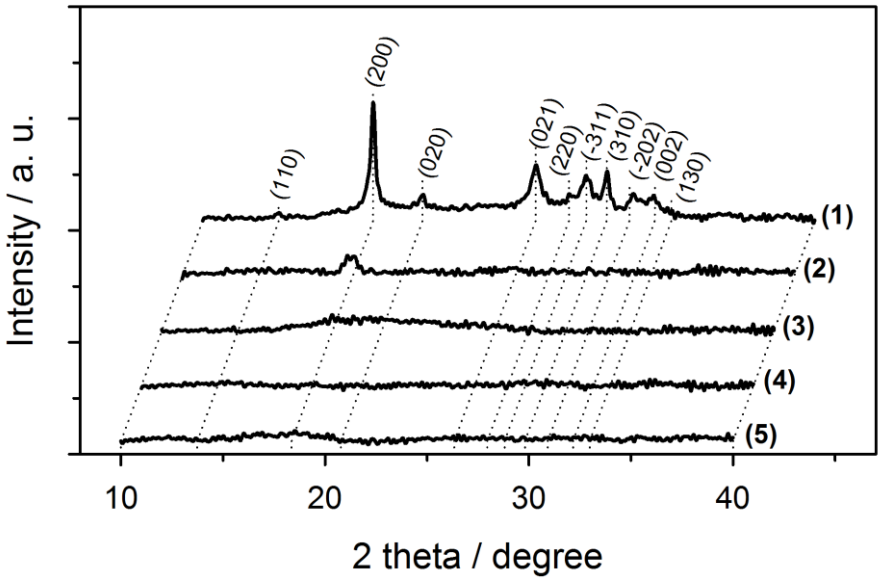

Figure 35. *Ex-situ* X-ray diffraction (XRD) of $LiVO_3$. The numbers indicate the points where the *ex-situ* XRD measurement were made in Figure 30.

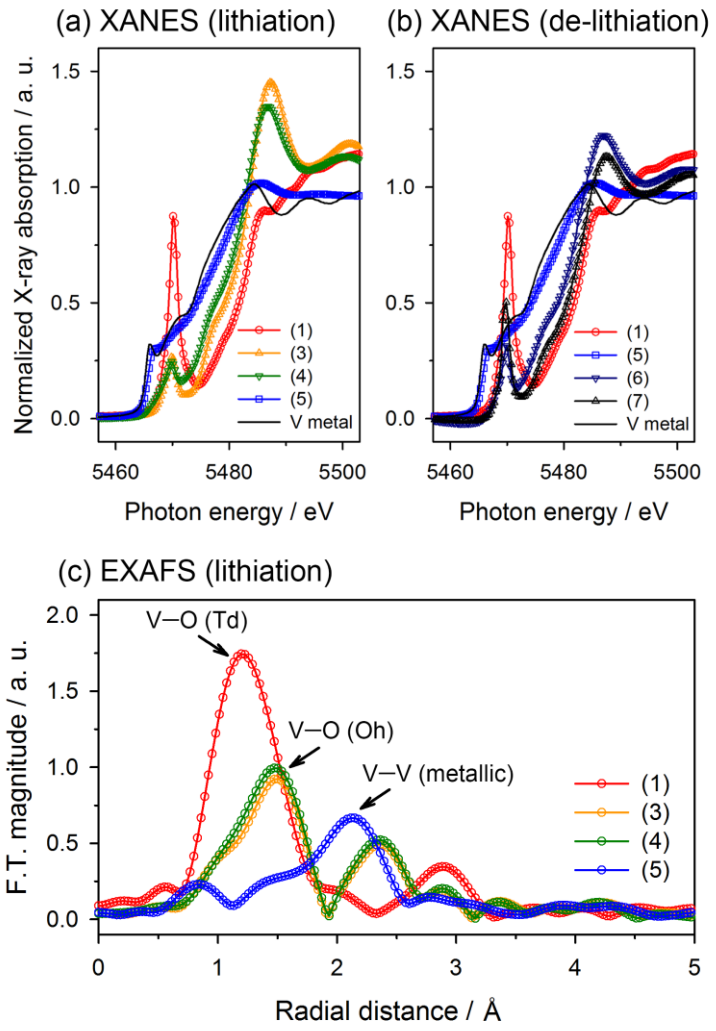

Figure 36. Normalized vanadium K-edge XANES spectra obtained during lithiation (a) and de-lithiation (b) and EXAFS spectra during lithiation (c) of $LiVO_3$ electrodes in the first cycle. The numbers indicate the points where the XAS measurements were made in Figure 30. Vanadium metal was used as a reference.

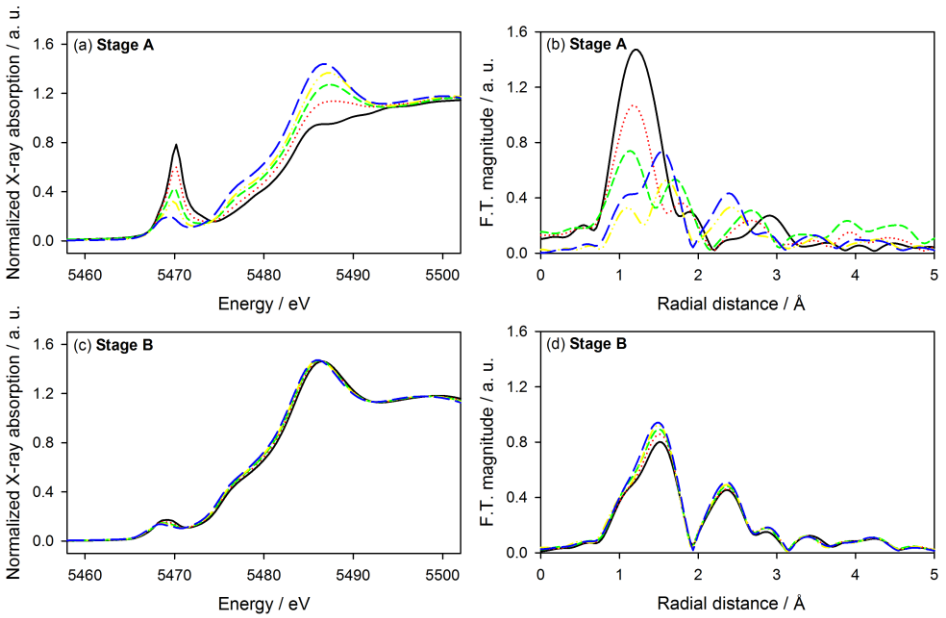

Figure 37. Normalized vanadium K-edge XANES spectra and Fourier-transformed EXAFS spectra of $LiVO_3$ electrodes in the first cycle obtained during stage A (a), (b) and stage B (c), (d), respectively.

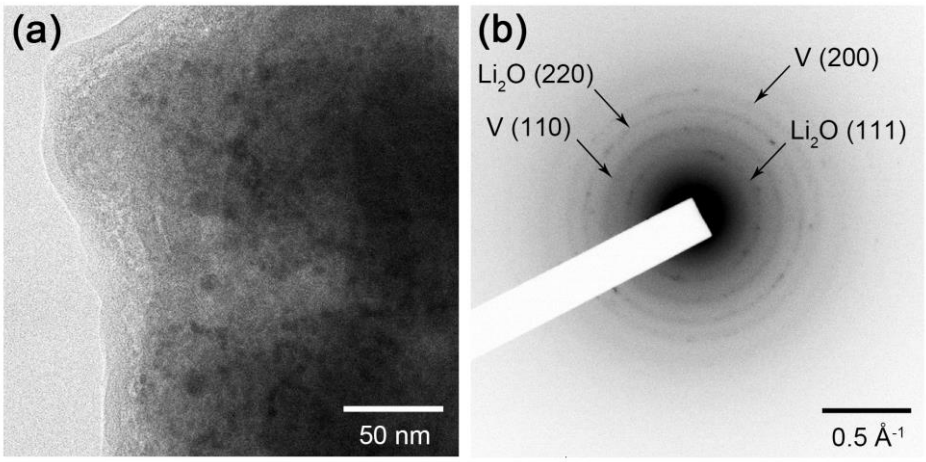

Figure 38. TEM image (a) and SAED pattern (b) obtained from the fully lithiated $LiVO_3$ electrode in the first cycle. The SAED pattern is shown in negative.

During delithiation, the vanadium ions continuously oxidize and recover their local structure which is a tetrahedral coordination. For the $LiVO_3$ electrode in this work, nano-sized vanadium metal cluster enclosed in Li_2O matrix is oxidized to form vanadium ions during delithiation. Here, the reverse reaction is quite feasible because the nano-sized metallic V results in high surface energy and the contact area between V and Li_2O facilitates the solid-state diffusion of Li^+, V^{n+} and O^{2-}.[14] The oxidized V^{n+}, Li^+ and O^{2-} ions diffuse in the matrix to generate Li−V−O structure.[97] In this particular circumstance, the stoichiometry of Li_2O and vanadium (3: 1 in mol ratio) in a confined domain seems to be the main cause for the re-conversion to initial state of $LiVO_3$. Indeed, a partial non-stoichiometry can lead to other phases of vanadium oxides, such as V_2O_5, as stated in equation below. However, the energy paths of possible re-conversion reactions calculated from the formation energies of the compounds show that the re-oxidation to $LiVO_3$ (Equation 4-7, E_r = 1.25 V (*vs.* Li/Li^+)) is thermodynamically favorable compared to the formation of V_2O_5 (Equation 4-8, E_r=1.44 V (*vs.* Li/Li^+)).[98]

$$E_r = -\frac{\Delta G_f}{nF} = -\frac{\sum G_f(\text{product}) - \sum G_f(\text{reactant})}{nF} \qquad \textbf{Equation 4-6}$$

$$3\,Li_2O + V \leftrightarrow LiVO_3 + 5\,Li \qquad \textbf{Equation 4-7}$$

$$3\,Li_2O + V \leftrightarrow \frac{1}{2}V_2O_5 + \frac{1}{2}Li_2O + 5\,Li \qquad \textbf{Equation 4-8}$$

The vanadium K-edge after full de-lithiation resembles its starting compound in shape, however, the intensity of the pre-edge and the energy shift of the main edge are

not completely recovered. This phenomenon could be somewhat related to the capacity fading in the early stage of the cycle.

4.2.3. Theoretical analysis

4.2.3.1. Detailed simulation methods

Li^+ storage sites in $LiVO_3$ were further studied by first-principle calculations. Density functional theory (DFT) studies on various metal oxide electrode materials have been well suited to prove the lithiation mechanism and to predict reaction potentials. $LiVO_3$ and Li_2VO_3 structures were extracted from ICSD database based on the experimental results and the rest of the structures were generated by inserting Li^+ ions in the basic structures. The detailed procedure is explained below.

As confirmed by XRD measurement (Figure 31), the resulting diffraction peaks show that the synthesized material is $LiVO_3$ (JCPDS No. 33-0835) which belongs to *C*2/*c* space group. The same structure was found in ICSD database (ICSD-68634) and geometric relaxation was performed. Since the $LiVO_3$ phase lose its long-range order during lithiation as it can be observed from the *ex-situ* XRD measurement (Figure 35), the intermediate phases were predicted based on the previous study by Pralong *et al.*[96] and the other experimental results including electrochemical and spectroscopic analysis. Since there are little information on the Li_2VO_3 structure in the previous studies and the databases, the possible structures were extracted from the structure which corresponds to Li_2MO_3 (M=transition metal ions) in the ICSD database and double checked by using crystal prediction module provided from Materials Project. Among the numerous number of candidates, the structures that suit to the experimental results (transition metal in octahedral coordination) were selected for the geometry relaxation. After all of the candidates

were relaxed using DFT calculation (Table 3), the most stable structure was chosen for Li_2VO_3 generated during lithiation of $LiVO_3$. The resulting Li_2VO_3 structure has a structure of Li_2MnO_3 structure (ICSD-46953) which is generally researched as a positive electrode material.

All the structure and reaction potential prediction were executed based on the experimental results. The modeling process of lithiation in the $LiVO_3$ (Stage A) was perfomed as follows. One Li^+ ion was added to the interstitial sites or vacancies existing in 2 × 1 × 1 cell of $LiVO_3$ (contains 8 Li^+ ions) and the structures were relaxed using DFT calculation to find the most stable structure. The same procedure was repeated to the resulting structures and the structures and formation energies during lithiation were obtained. (8 Li^+ ions were inserted into the 2 × 1 × 1 cell of $LiVO_3$ to form Li_2VO_3 structure.) The formation energy was calculated using the following equation:

$$\Delta E_f = E_f(\mathrm{Li}_y\mathrm{VO}_3) - [E_f(\mathrm{Li}_x\mathrm{VO}_3) + (y-x)E_f(\mathrm{Li})] \qquad \textbf{Equation 4-9}$$

The formation energies of $Li_{1+x}VO_3$ ($0 < x < 1$) structures were then compared to that of the two-phase reaction of $LiVO_3/Li_2VO_3$. As seen in Figure 39, the formation energies for the single-phase reaction show larger value than that of two-phase reaction, implying that the two-phase reaction is thermodynamically favored. The voltage plateaus obtained from the calculated formation energies were determined by convex hull theorem. The reaction potential during lithiation was calculated using the following equation:

$$V = -\frac{\Delta E_f}{(y-x)} \qquad \textbf{Equation 4-10}$$

The lithiation in Li_2VO_3 was performed in the same way. Li^+ ion was inserted into the interstitial sites or vacancies existing in 2 × 1 × 1 cell of Li_2VO_3 (contains 16 Li^+) and the geometry relaxation was performed. To simulate the amorphous structure of $Li_{2+x}VO_3$,

Table 3. Formation energies of iso-structures of Li_2VO_3 phases obtained from ICSD and Materials project.

Li_2VO_3	E_f/[eV/VO_3]	Li_2VO_3	E_f/[eV/VO_3]	Li_2VO_3	E_f/[eV/VO_3]
Crystal70319	-41.2764	Crystal70398	-40.3891	Crystal70522	-40.7022
Crystal70325	-41.4002	Crystal70441	-40.8925	Crystal70529	-32.9432
Crystal70327	**-41.4009**	Crystal70450	-40.9967	Crystal70530	-39.2849
Crystal70346	-41.2089	Crystal70452	-40.7132	Crystal70532	-40.7115
Crystal70357	-41.3070	Crystal70455	-40.8973	Crystal70536	-41.0670
Crystal70359	-40.9351	Crystal70457	-41.2703	Crystal70540	-40.3409
Crystal70361	-41.0142	Crystal70484	-41.1338	Crystal70543	-41.0273
Crystal70364	-41.2618	Crystal70488	-41.2083	Crystal70544	-41.0581
Crystal70371	-40.7777	Crystal70499	-41.1523	Crystal70548	-41.3003
Crystal70392	-41.2092	Crystal70521	-40.3065		

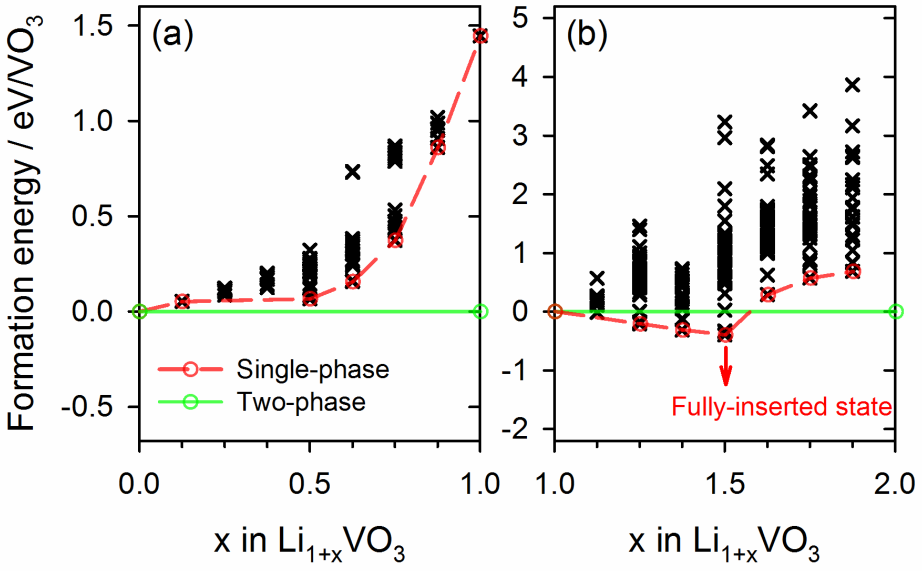

Figure 39. Formation energies of (a) single-phase reaction of $Li_{1+x}VO_3$ ($0 < x < 1$) compared with the two-phase reaction of $LiVO_3/Li_2VO_3$ and (b) single-phase reaction of $Li_{1+x}VO_3$ ($1 < x < 2$) compared with the two-phase reaction of Li_2VO_3/Li_3VO_3.

Molecular Dynamics (MD) simulation (T = 1200 K) was performed. The layered structure of Li_2VO_3 maintains until the 8 Li+ addition. However, the layered structure starts to collapse after $Li_{2.5}VO_3$ (x = 1.5); after all the possible interstitial site are occupied by Li^+ ions. Further lithiation was simulated by continuously adding Li^+ ions into the largest void space by Delaunay triangulation method. The structures were then MD simulated and relaxed repeatedly. Finally, after 5 Li^+ addition into $LiVO_3$, the vanadium metal cluster and Li–O cluster can be obtained from the geometry relaxation and MD simulation.

Here, U parameter was not utilized during DFT-GGA calculations. The reasons for not considering the U parameter are as follows. First of all, the U values are affected by the electronic states of vanadium. Therefore, it is difficult to determine the appropriate U value since the vanadium valence changes: V^{5+} in $LiVO_3$ reduces to its elemental state during lithiation. The simulation performed with U parameter gives significantly overestimated reduction potential values as shown in Figure 40. Furthermore, the DFT-GGA calculation without U parameter predicts adequate reaction potentials for the lithiation and de-lithiation of V_2O_5.[87] Hence, the authors decided not to utilize U parameter in the calculation and more focus on the crystallinity and the intermediated structures of $Li_{1+x}VO_3$ during lithiation.

4.2.3.2. Lithiation in $LiVO_3$ analyzed by density functional theory (DFT)

Figure 41 shows the theoretical prediction of the reaction potential and their resulting structures of lithiated $LiVO_3$. $LiVO_3$ belongs to the space group of *C*2/*c* and it has been reported that its structure has a unidimensional characteristic built up of chains of corner sharing VO_4 tetrahedra, interconnected through LiO_6 octahedra.[99] After the first intercalation, it transforms into Li_2VO_3, a Li-rich rock-salt structure with cation planes that are alternatively occupied by Li^+ and Li^+/V^{4+} mixed layers, which have the same

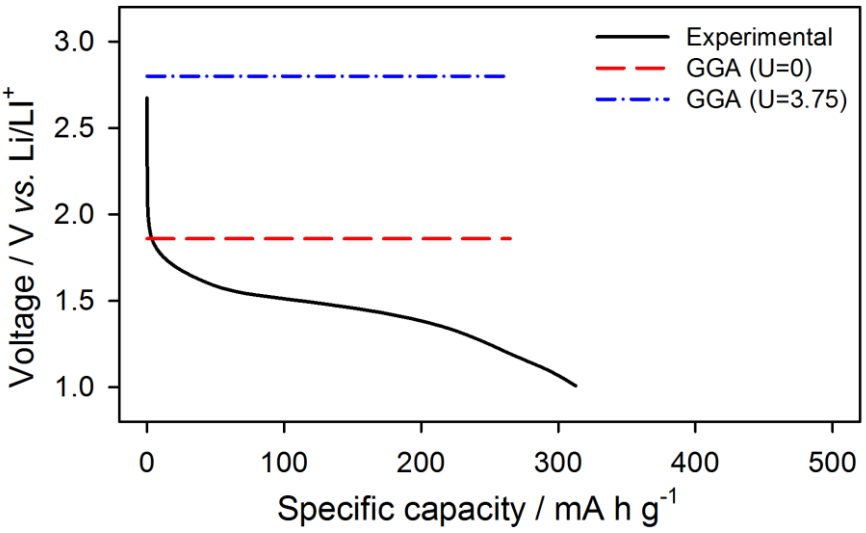

Figure 40. Estimated reduction potentials of $LiVO_3$ during stage A depending on the U values.

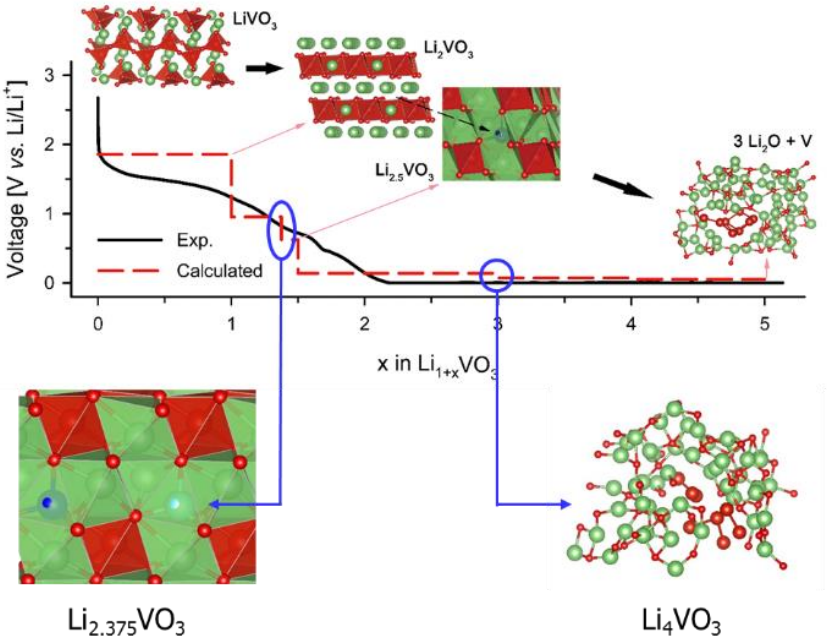

Figure 41. Calculated lithiation voltage profile and the experimentally observed one for $LiVO_3$ electrode. The structural evolution is depicted in the inset.

anionic framework as monoclinic Li_2MnO_3 (space group: *C*2/*m*).[100] The calculated formation energy confirmed that this Li_2VO_3 structure is the most stable structure compared to other iso-structure of lithiated $Li_{1+x}VO_3$ (x = 1). The calculated formation energies within the intermediated phases of $Li_{1+x}VO_3$ (0 < x < 1) were significantly higher than the tie line of the formation energies between $LiVO_3$ and Li_2VO_3, implying the occurrence of a two-phase reaction with a single voltage step. The predicted reaction potential, 1.859 V, is well-matched with the experimental value, considering the electrode polarization during the transient galvanostatic lithiation. This result is consistent with the XANES data that showed that vanadium ions transfer from tetrahedral sites to octahedral sites.

The simulation also provides important structural information that can hardly be observed from experimental data. It is commonly known that Li^+ insertion in a rock-salt structure is difficult because no interstitial sites are energetically stable for Li^+ ions. However, further lithiation in a Li_2VO_3 structure can proceed at 0.955 V and 0.623 V. According to the simulation, the Li^+ ions are inserted into the tetrahedral sites in the Li^+ layer, especially the sites adjacent to Li^+ ion located in the Li^+/V^{4+} mixed layer (a white sphere in Figure 41). This feature has also been described in the study by Bruce *et al.*[101] in which Li^+ insertion into the $Li_{1+x}V_{1-x}O_2$ layered oxide is feasible only when the Li^+ ions are substituted within the vanadium layer. The Li^+ ions inserted during stage B trigger large distortions on the $Li_{2+x}VO_3$ structure, thereby causing the breakdown of the structure at a potential of 0.139 V which is in good agreement with the experimental data. After the collapse of the structure, lithiation proceeds until the oxidation state of the vanadium reaches its elemental state. As presented in the Figure 41, $Li_{1+x}VO_3$ (x = 3) shows a similar structure to $Li_{1+x}VO_3$ (x = 5), which is an amorphous phase containing Li_2O and vanadium metal clusters.

4.2.4. Lithium storage mechanism of $LiVO_3$

As predicted from the experimental and computational analysis, the Li^+ storage reaction of $LiVO_3$ can be summarized as follows:

$$LiVO_3 + Li^+ + e^- \rightarrow Li_2VO_3$$

(Two-phase insertion) **Equation 4-11**

$$Li_2VO_3 + 0.5\,Li^+ + 0.5\,e^- \rightarrow Li_{2.5}VO_3$$

(Single-phase insertion) **Equation 4-12**

$$Li_{2.5}VO_3 + 3.5\,Li^+ + 3.5\,e^- \rightarrow V + 3\,Li_2O$$

(Two-phase conversion) **Equation 4-13**

$$LiVO_3 + 5\,Li^+ + 5\,e^- \rightarrow V + 3\,Li_2O$$

Equation 4-14

4.2.5. Comparative study on the conversion reaction of vanadium oxides ($LiVO_3$ and V_2O_5)

4.2.5.1. Electrochemical analysis

It was demonstrated that Li^+ ions could be stored with a conversion-type reaction even in an early-transition metal oxide. However, there have been no reports on vanadium oxides (for example, V_2O_5) that are lithiated by the conversion reaction at ambient temperature. V_2O_5 is a well-known electrode material that is lithiated by the insertion reaction with a limited specific capacity.[61,86,87] At an elevated temperature (60°C), however, V_2O_5 shows a long plateau near 0 V which can be inferred as conversion-type lithiation as

shown in Figure 28. At the end of lithiation of V_2O_5 at the elevated temperature, V reduces to its elemental state as observed from $LiVO_3$, implying that the conversion reaction is also possible in other vanadium oxides (Figure 29).

This interesting feature shows that the conversion reaction of V_2O_5 is thermodynamically possible but prohibited at ambient temperature due to kinetic reasons. To determine the difference that affects the feasibility of conversion reactions in vanadium oxides, both thermodynamic and kinetic studies were performed on vanadium pentoxide (V_2O_5) and $LiVO_3$. By measuring the quasi-open-circuit voltage (QOCV) for V_2O_5 and $LiVO_3$ with the galvanostatic intermittent titration technique (GITT) at an elevated temperature, the quasi-equilibrium potential for conversion reaction (thermodynamic values) was derived. Also, the electrochemical impedance spectroscopy (EIS) were performed for the cell in the same state-of-charge (SOC).

In general, GITT data is not quite reliable for the conversion reaction because the quasi-equilibrium potentials are difficult to be measured. Hence, there exists some uncertainty in the measured values. The relaxation potentials (quasi-equilibrium potentials) are inaccurate for the conversion-type metal oxide electrodes because the potentials are not stabilized due to numerous interfering reactions. This feature was observed as shown in Figure 42. As is seen in Figure 42a, the OCV keeps increasing and the vanadium is oxidized with an increase in the rest time at 60ºC. Many possibilities exist for this. One of them is the degradation of surface film (maybe dissolution at high temperature). Due to the loss of passivating ability of the surface film, electrolyte is reductively decomposed on the newly exposed electrode surface, which leads to an increase in both OCV and oxidation state of vanadium because of removal of Li^+/electrons from the vanadium oxide electrode. A similar behavior was observed in graphite electrode.[102] In order to obtain stable relaxation potentials, the resting temperature were lowered from 60ºC to 25ºC with

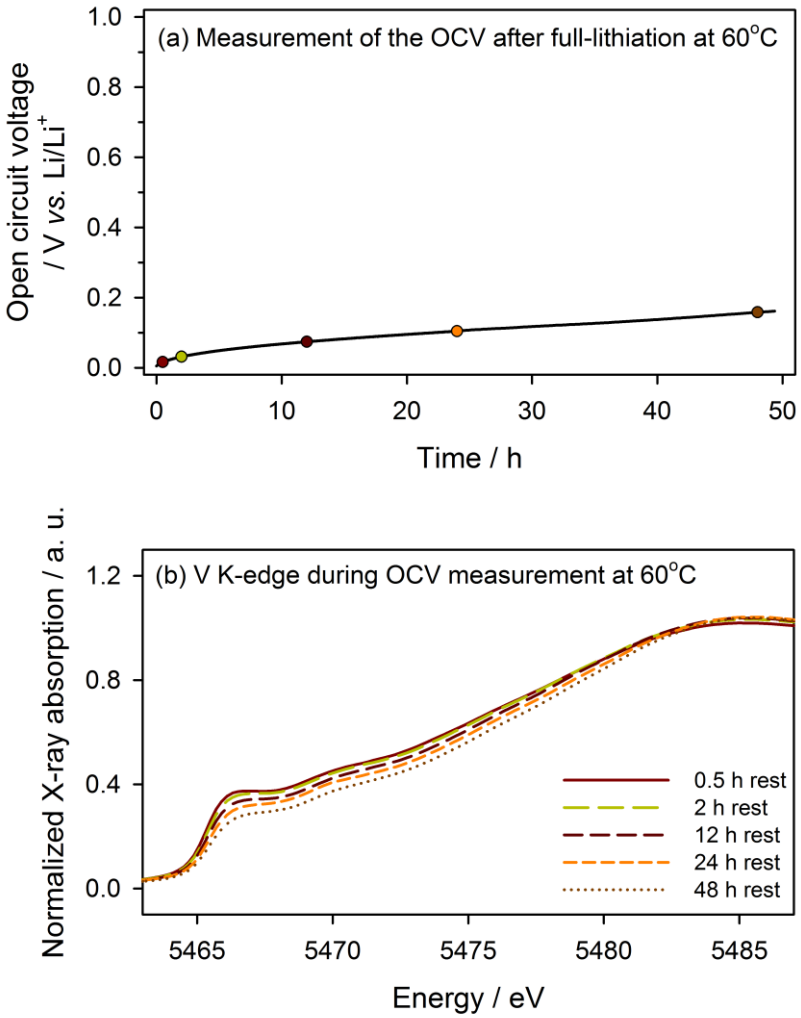

Figure 42. Self-discharge phenomena observed during high-temperature (60°C) storage of fully-lithiated $LiVO_3$. (a); measurement of the open-circuit-voltage (OCV) and (b); normalized vanadium K-edge XANES spectra obtained during storage.

an expectation that unwanted parasitic reactions, one of which may be the surface film degradation and electrolyte decomposition as mentioned above, can be mitigated by lowering the resting temperature. The OCVs were measured while the cells being stored at 25ºC for 24 h (the inset of Figure 43). This measurement was performed five times, and the resting time was enlarged up to 10 days in the final measurement. As is seen in the insets, even if the relaxation potentials are drifting, there appears a meaningful difference in the quasi-equilibrium potentials for two electrodes. The values taken by averaging the six quasi-equilibrium potential values are 0.12 V (vs. Li/Li^+) for $LiVO_3$ and 0.07 V for V_2O_5. The higher quasi-equilibrium potential value (0.12 V) for $LiVO_3$ suggests that the conversion reaction is thermodynamically favored for $LiVO_3$.

Figure 44 displays the Nyquist plots, which are composed of two semicircles, during the conversion-type lithiation period. The semicircle at the high-frequency region can be assigned to the parallel combination of SEI resistance (R_{SEI}) and CPE components (capacitors) of the surface film, whereas the semicircle at the middle-frequency region is the combination of the charge transfer resistance (R_{CT}) and double-layer capacitance (CPE_{dl}). The impedance parameters obtained by fitting the spectra shows a remarkable difference; $Li_{2x}V_2O_5$ (x = 3) electrode shows a larger R_{CT} value; 3.34 Ω g vs. 1.26 Ω g for $Li_{1+x}VO_3$ (x = 3) electrode, whereas the similar RSEI values of two electrodes were observed; 1.58 Ω g for $Li_{2x}V_2O_5$ (x = 3) and 1.57 Ω g for $Li_{1+x}VO_3$ (x = 3). Considering that the charge transfer process in conversion reaction is governed by the mass transfer of mobile species,[47] the solid-state diffusion of Li^+, V^{n+} and O^{2-} ions in $Li_{2x}V_2O_5$ structure to generate metallic vanadium and Li_2O seems to be the main cause of larger kinetic barrier.

To summarize, the evolution of conversion reaction in $LiVO_3$ at ambient temperature can be accounted for by the higher electrode potential (thermodynamic consideration)

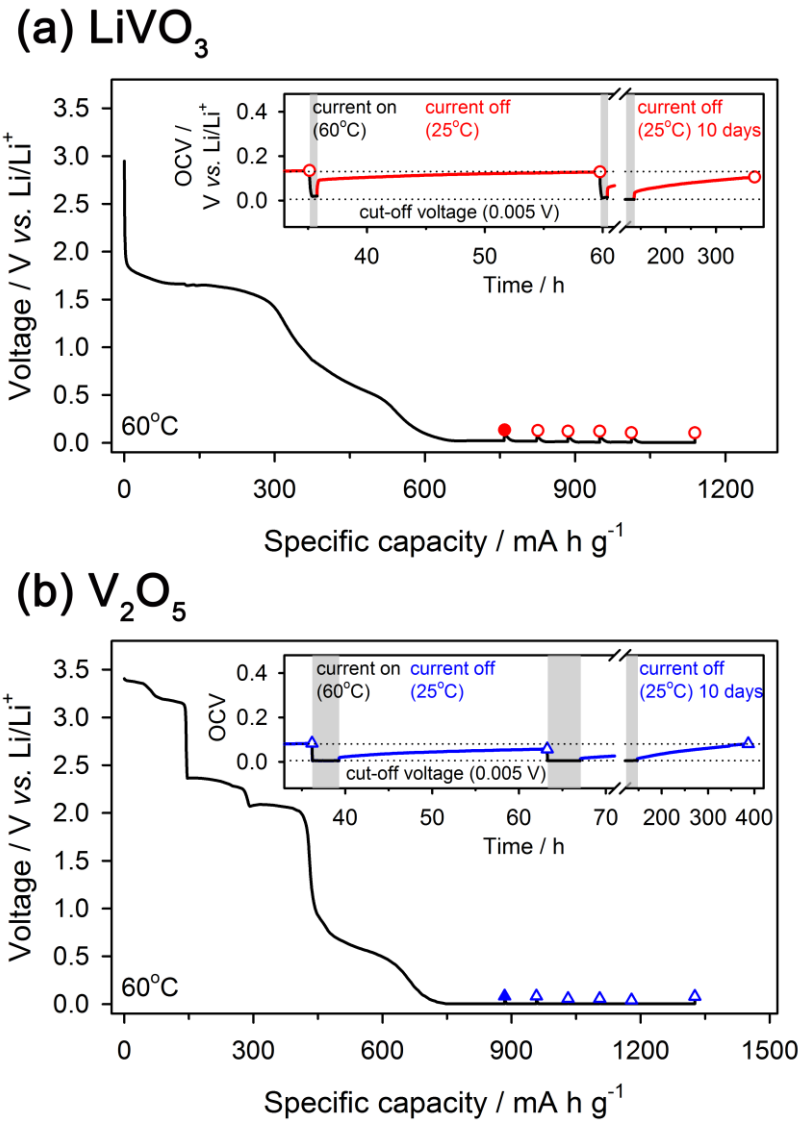

Figure 43. The transient voltage profiles of $LiVO_3$ (a) and V_2O_5 (b) at 60°C overlapped with GITT data The GITT experiment was performed by resting cells for 24 h at 25°C.

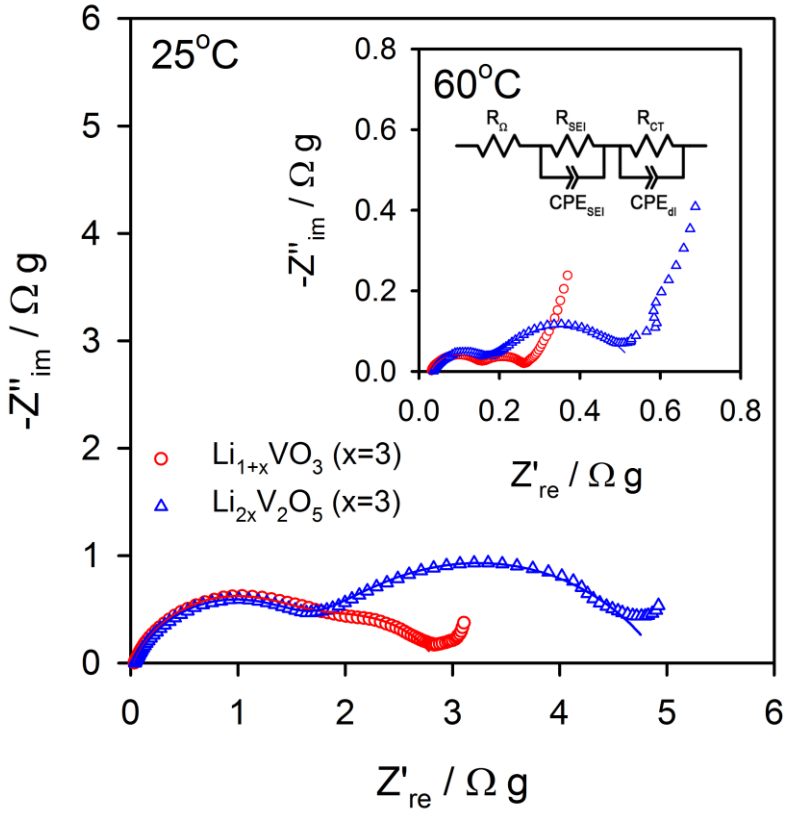

Figure 44. Nyquist plots of $LiVO_3$ and V_2O_5 after OCV stablization (closed circle and triangle in (a) and (b), respectively).

and lower internal resistance (kinetic consideration). The conversion reaction of V_2O_5 is unfavorable in both the thermodynamic and kinetic aspect, such that it is allowed only at elevated temperatures.

4.2.5.2. Theoretical analysis

There are several factors that can affect the kinetic barrier of the conversion reaction for metal oxides. Especially, M–O bond cleavage and the diffusion of Li^+, M^{n+} and O^{2-} in the solid state are the key factors that can determine the kinetics of nucleation and growth during the conversion reaction. To rationalize those factors and thus elucidate the crystallographic difference affecting the kinetics, the defect formation energy of vanadium ions and Li^+ ion exchange activation energy were compared for the lithiated vanadium oxides ($Li_{2.5}VO_3$ and ω-$Li_3V_2O_5$[60]) with the nudged elastic band (NEB) method in quantum mechanics calculations. From the calculation results, the V–O bond strength and the kinetic barrier for ionic diffusion could be predicted for each solid phase. We first compared the vanadium defect formation energies. The formation energy E_f of the lithiated vanadium oxides with vanadium ion defect may be written as:

$$E_f = E(\mathrm{V}_d\mathrm{LVO}) - [E(\mathrm{LVO}) - E(\mathrm{V})] \qquad \textbf{Equation 4-15}$$

where $E(\mathrm{V}_d\mathrm{LVO})$ is the energy of a supercell containing one vanadium ion defect. E(LVO) and E(V) are the energies of lithiated vanadium oxides and vanadium, respectively. The calculated defect formation energies of the vanadium ions for $Li_{2.5}VO_3$ was 0.71 eV and that for $Li_3V_2O_5$ was 2.10 eV, which supports that vanadium ions in $Li_3V_2O_5$ are strongly bonded to the surrounding oxygens.

The activation energy for Li^+ ion site exchange, which reflects the barrier for the Li^+ ions to diffuse in the fully-inserted oxides, was calculated by using the nudged elastic

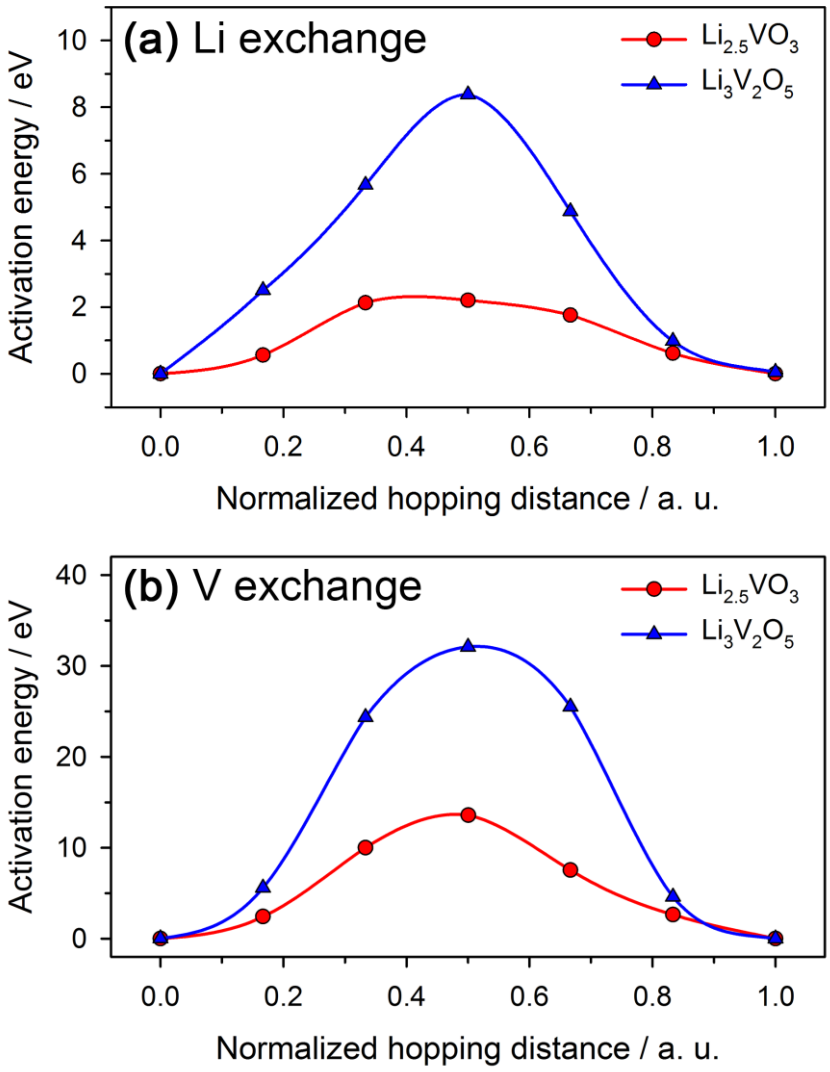

Figure 45. Activation energy for (a) Li^+ ion site exchange and (b) V ion site exchange in $Li_{2.5}VO_3$ and $Li_3V_2O_5$.

band (NEB) method, from which the Li^+ mobility during conversion and structure flexibility can be compared for $Li_{2.5}VO_3$ and $Li_3V_2O_5$, where the insertion of Li^+ ions was terminated. As is seen in Figure 45a, the activation energy for Li^+ ions hopping to the first nearest neighbor sites in $Li_{2.5}VO_3$ is smaller than that in $Li_3V_2O_5$. The similar result can be observed in V ion diffusion as can be noticed from the NEB calculation of V ion exchange activation barrier in Figure 45b, implying that V−O bond breakage and Li^+ and V ion diffusion, which strongly affect the kinetics of con version reaction, is more feasible in the $Li_{2.5}VO_3$ structure. From those observations, the lower internal resistance of $LiVO_3$ during the conversion reaction is related to the activation energy required for V–O bond cleavage and the diffusion of mobile species within the structure.

4.2.6. Performance improvements of $LiVO_3$ via modification of the material's chemistry

4.2.6.1. Failure mode of $LiVO_3$ electrode

In the previous sections, it was demonstrated that $LiVO_3$, which shows a large reversible capacity utilized by conversion-type lithiation in the first cycle, is a promising candidate for the negative electrode material for LIBs. There exists a major drawback of $LiVO_3$ electrodes, however, which is the poor reversibility at the early stage of cycles. As can be seen in Figure 46, Li/$LiVO_3$ cell shows a large specific capacity over 1,000 mA h g^{-1} at the first cycle, however, the capacity drops dramatically to ~750 mA h g^{-1} within the 15th cycle and its Coulombic efficiency is also poor in this period.

To investigate the reasons for the poor cycle retention, the electrochemical data of the Li/$LiVO_3$ cell were further examined. As seen in the voltage profiles and the differential capacity (dQ/dV) plots of Li/$LiVO_3$ cell (Figure 47), their shape rarely

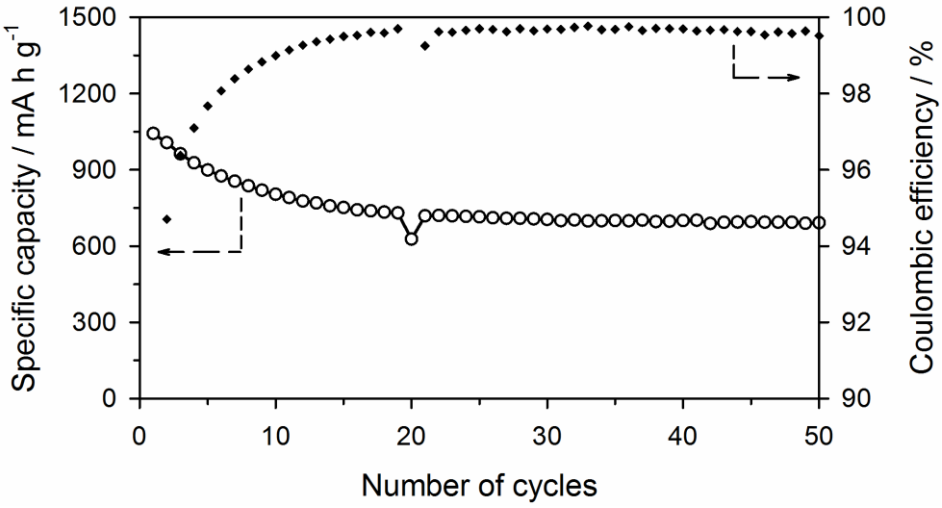

Figure 46. Cycle performance and Coulombic efficiency of the Li/$LiVO_3$ cell.

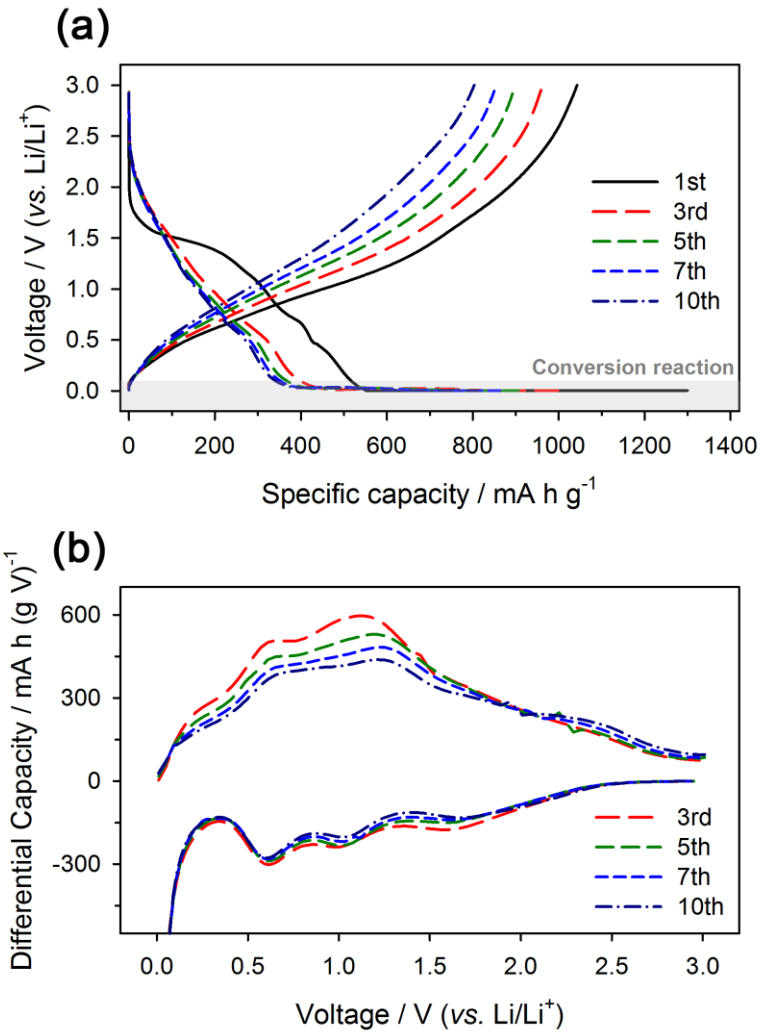

Figure 47. (a) Voltage profiles of $LiVO_3$ during cycle. Lithiation below 0.1 V can be considered as a conversion reaction. (b) Differential capacity (dQ/dV) plots of $LiVO_3$ during cycle.

changes, but the specific capacity and redox peaks gradually decrease in the early stage of cycles. However, there exists a different behavior during lithiation and delithiation of $LiVO_3$. No overpotential can be observed during lithiation, whereas overpotential occurs during delithiation. This phenomenon is resulted from the volume change of the active material, $LiVO_3$, during cycles. Upon lithiation, when the volume of $LiVO_3$ expands, the contact of composite electrode is further enhanced. During delithiation, on the other hand, the volume of $LiVO_3$ shrinks down to loosen the contact between the each particles. The quasi-open-circuit-potential observed after lithiation and delithiation (Figure 48) also shows the similar behavior that is resulted from the reasons mentioned above. As shown in Figure 48, the state-of-charge (SOC) after lithiation gets higher along with cycles, whereas the depth-of-discharge (DOD) after delithiation gets lower.

To clarify the main cause of capacity fading, lithiation in $LiVO_3$ was divided into two parts: insertion-type lithiation above 0.1 V and conversion-type lithiation below 0.1 V as illustrated in Figure 47a. The amount of stored Li^+ ions in each parts were separated and their capacity and ratio were plotted in Figure 49. As can be observed in Figure 48, during the period where the capacity fade significantly, ratio of specific capacity delivered from the conversion reaction over total specific capacity rarely changes. It implies that the amount of active materials that participate Li^+ storage is decreased resulted from the deteroration of composite electrodes during the early stage of cycles. This failure can be stem from the volume change during cycles, which is commonly considered as main cause of electrode failure in the conversion-type metal oxides and Li-alloying materials. From the cross-sectional image of $LiVO_3$ electrode in Figure 50, it can be observed that the composites on the current collector completely detached after 10^{th} cycle. To sum up, the schematic diagram of capacity fading in $LiVO_3$ electrode can be illustrated as

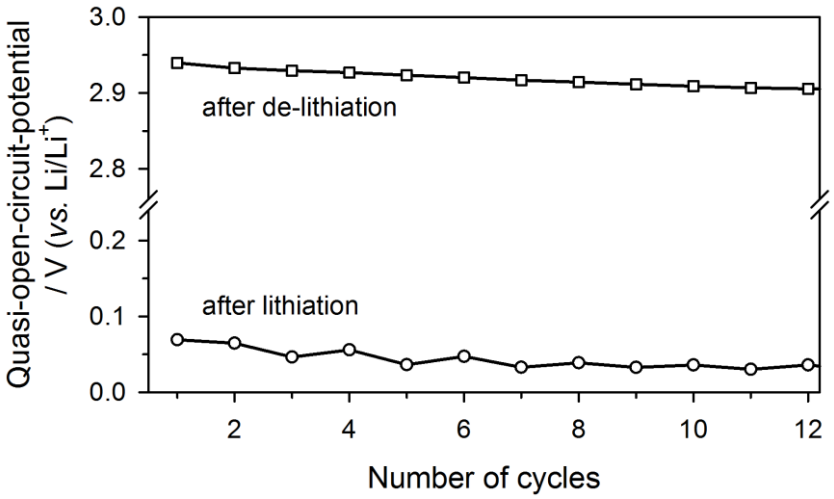

Figure 48. Quasi-open-circuit-potential after lithiation and de-lithiation of $LiVO_3$ during cycles.

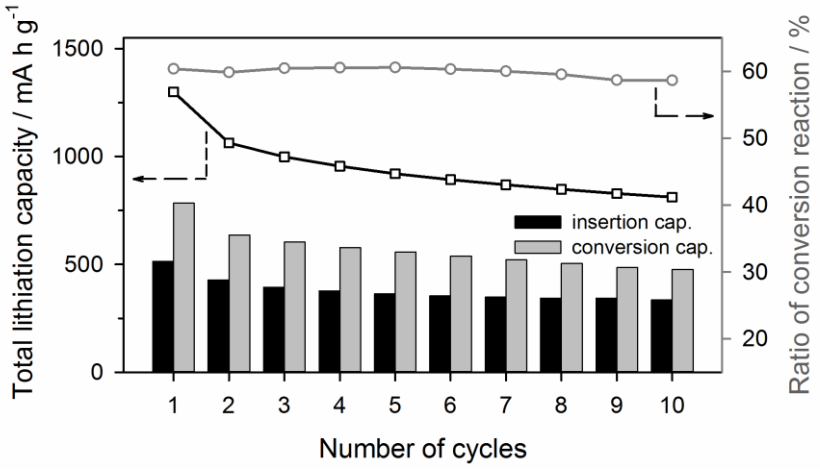

Figure 49. Failure mode analysis on $LiVO_3$ electrode. Black square dots refer to lithiation specific capacity and grey circle dots refer to the ratio of capacity delivered from conversion reaction over total capacity.

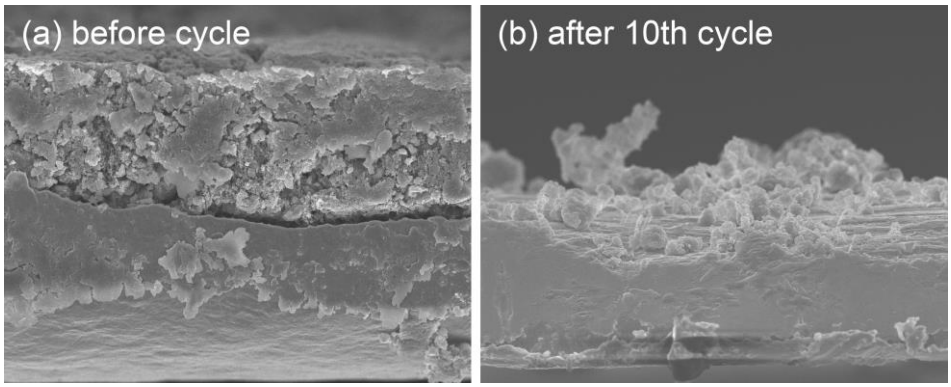

Figure 50. Cross-sectional views of $LiVO_3$ electrodes; (a) before cycle and (b) after 10^{th} cycle.

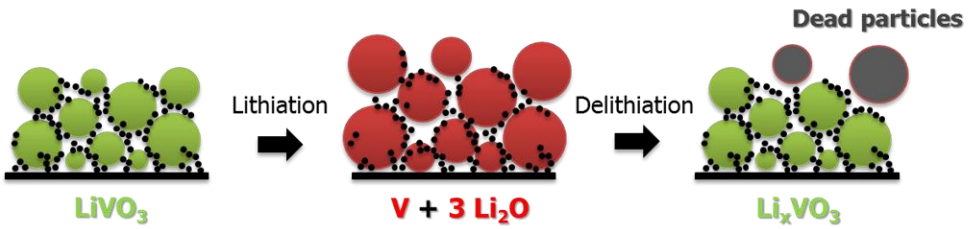

Figure 51. Schematic diagram of capacity fading in $LiVO_3$ electrode.

Figure 51. After the lithiation which accompanies volume expansion of the electrode, the polymeric binder (PVdF) lose its binding ability upon delithiation (volume shrinkage) and produce overpotential during delithiation and dead particles which are resulted from poor electrical contact in the composite electrode.

4.2.6.2. Solutions to improve cycleability

In order to overcome these intrinsic drawbacks of $LiVO_3$ above mentioned and further improve its cycle life, a new material chemistry to facilitate a stable conversion reaction of $LiVO_3$ was considered in this section.

Although the PVdF binder is the most frequently used in commercial electrodes, its adhesive property is insufficient to be applied in the negative electrodes that suffer from severe volume change during cycles. Recent studies have demonstrated that strong adhesive binders such as carboxymethyl cellulose (CMC), polyacrylic acid (PAA) and polyacrylate lithium salt (LiPAA) successfully suppress the degradation of electrodes. Unfortunately, these binders are not applicable in $LiVO_3$ electrode, because they are to be processed by dissolving in water but $LiVO_3$ is highly soluble in water. Therefore, in order to utilize the conversion-type reaction of $LiVO_3$ with good cycle performance, the chemistry of the starting materials has to be modified, which is appropriate for processing with strongly adhesive water-soluble binders.

Here, for the enhanced cycle life of $LiVO_3$ electrodes, a new chemistry was designed to build Cu/$LiVO_3$ nanocomposites electrochemically during galvanostatic charge/discharge using copper vanadate (CuV_2O_6). CuV_2O_6, which is often used as a photocatalyst for water splitting,[103] is insoluble in water and thus can be processed with strong water-soluble binders to fabricate electrodes which are highly resistive to the mechanical stress.

To implement this chemistry, the redox tendancy of 3d transition metals, which was introduced in Section 2.2.4.2.2, was used. As seen in Figure 2, which describes the empirical values for the reduction potential of 3d transition metals, Cu ions have a higher redox potential compared to V ions. Thus, Cu ions in the copper vanadate are reduced to its elemental states prior to the V ions which are then reduced to its elemental states to form metallic V and Li_2O in the lower potential upon lithiation. The extrusion of metallic Cu in copper vanadates is well known from the previous works of Tarascon *et al*.[104] In this work, the copper vanadates function as positive electrode materials, thus their operating potential is 1.5 – 3.5 V. The vanadate frameworks are not collapsed upon the repetitive cycles and Cu ions are inserted into the framework reversibly in this potential range. However, in the potential range of 0.005 – 3.0 V, which is the same potential range for $LiVO_3$ electrodes, they are expected to undergo different reaction path. As observed in $LiCuVO_4$ electrodes, Cu ions extruded to form metallic Cu during lithiation are not reversibly inserted into the framework.[105] The expected reaction path of CuV_2O_6 during lithiation and delithiation in the potential range of 0.005 – 3.0 V is illustrated in Figure 52 and its reaction paths are as follows:

$$CuV_2O_6 + 12\,Li^+ + 12\,e^- \rightarrow Cu + 2\,V + 6\,Li_2O \qquad \textbf{Equation 4-16}$$

$$Cu + 2\,V + 6\,Li_2O \leftrightarrow Cu + 2\,LiVO_3 + 10\,Li^+ + 10\,e^- \qquad \textbf{Equation 4-17}$$

Upon lithiation, both Cu and V cations are expected to fully reduce to their elemental states as described in Equation 4-16. Afterward, metallic Cu remains inactive in the electrode and metallic V and Li_2O, which are dispersed in 1: 3 mol ratio, oxidize to produce $LiVO_3$ (Equation 4-17).

There are two major advantages of using CuV_2O_6 from the beginning instead of $LiVO_3$. First, the $LiVO_3$ electrode can be fabricated with strongly adhesive water-soluble binders

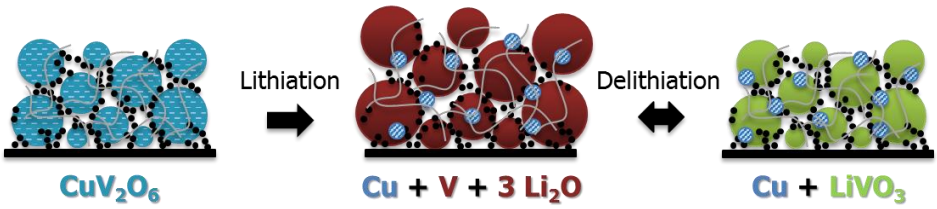

Figure 52. Schematic diagram of *in-situ* conversion process into $Cu/LiVO_3$ nanocomposite in CuV_2O_6 electrode.

and. Second, *in-situ* generated metallic Cu in the electrodes can works as an electronic conductive network and a buffer matrix and supports the $LiVO_3$ electrode to enhance its reversibility and cycleability. It has been widely studied that extra metallic Cu can behave as follows: (i) Cu strongly interact with active materials and thus alter their kinetic properties. (ii) well-dispersed Cu enhance the electronic conductivity by providing electronic conductive network in the electrodes. (iii) Cu can serve as a buffer matrix which can suppress the volume expansion.[105–109]

4.2.6.3. Material characterization of copper vanadate (CuV_2O_6)

The XRD pattern confirmed that the CuV_2O_6 was synthesized well (Figure 53, JCPDS No. 45-1054). Its size which was larger than 10 microns, were reduced by ball-milling process as shown in Figure 54.

4.2.6.4. Electrochemical properties and lithium storage mechanism of CuV_2O_6

As presented in Figure 55, CuV_2O_6 shows a different voltage curve with $LiVO_3$ in the first lithiation process. Regarding to the previous studies, the first plateau in CuV_2O_6 is reduction of Cu^{2+} to Cu^{+} and Cu^{+} is further reduced to its elemental state in the second plateau.[91] It is known that the metallic Cu is extruded from the vanadate structure and generates nano-sized particles during the reduction.[104] Along with formation of metallic Cu particles, Li^{+} ions are inserted into the vanadate structure and then the V^{5+} ions start to be reduced and the characteristic lithiation plateau near 0.0 V can be observed. Those lithiation process can be confirmed from the *ex-situ* XANES spectra shown in Figure 56 and Figure 57. As shown in Figure 56, upon the lithiation of 0.5 Li^{+}, Cu ions are slightly reduced but metallic Cu−Cu does not appear. After then the Cu−Cu metallic bonds can

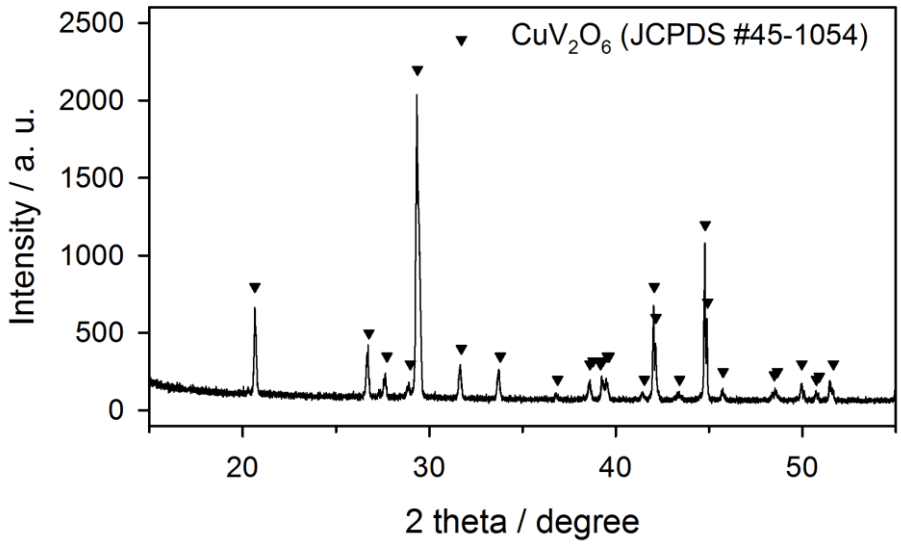

Figure 53. XRD pattern of as-prepared CuV_2O_6 powder.

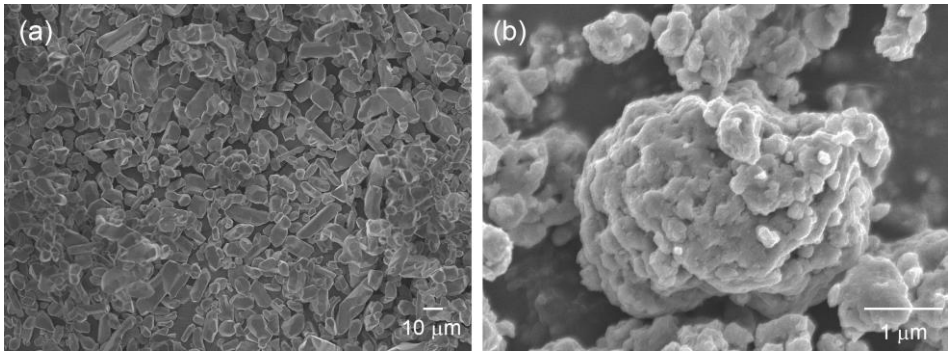

Figure 54. FE-SEM images of (a) as-prepared CuV_2O_6 and (b) ball-milled CuV_2O_6.

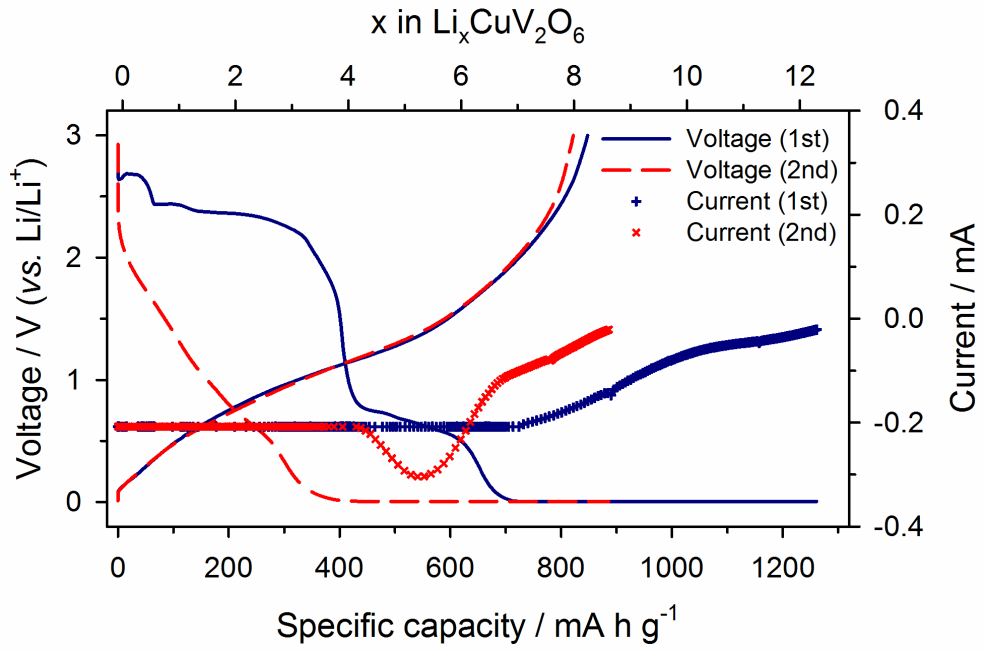

Figure 55. The galvanostatic lithiation/de-lithiation voltage profiles and current transient of Li/CuV_2O_6 cell. Solid lines indicate the voltage curves and plus and cross symbols indicate the current transients.

be clearly observed and V ions start to be reduced. After the lithiation of 3 Li^+, the reduction of Cu is completed to generate metallic Cu particles in the electrode. The insertion reaction continues until the storage of 6 to 8 Li^+ in CuV_2O_6 formula and afterward V−O bonds disappear and metallic V−V bonds are generated, proving the occurrence of conversion reaction at the 5 mV plateau. The current was measured in this region, at which the lithiation proceeds with constant-voltage charging. It showed bell-shaped transient as observed in the stage C of $LiVO_3$, which notifies the two-phase conversion reaction of vanadate structure (Figure 55).[92]

After the first cycle, however, voltage curve of CuV_2O_6 becomes similar to that of $LiVO_3$. It can be confirmed from the differential capacity plots of CuV_2O_6 and $LiVO_3$ presented in Figure 58. *Ex-situ* vanadium K-edge XANES spectra, shown in Figure 59a, also show that metallic V oxidizes to form $LiVO_3$. This similarity in the voltage curves and XANES spectra signifies that the reversible Li^+ storage in CuV_2O_6 follows the schematic diagram depicted in Figure 52. As observed in *ex-situ* copper K-edge XANES spectra (Figure 59b), Cu maintain its elemental state even in the delithiated state. Thus, it can be concluded that the completely reduced metallic Cu does not engage in the redox reaction in the electrode and remains inactive.

Fabricated with the LiPAA binder, which is known for its superior adhesive property, CuV_2O_6 shows remarkable cycle performance as shown in Figure 60. This increment in cycle life could be implemented because of the reasons discussed earlier. First of all, strong water-soluble binder (LiPAA) could be utilized in fabrication of electrode by changing starting active material from $LiVO_3$ to CuV_2O_6. Inactive Cu particles produced upon cycling worked as a buffer matrix and electron conducting networks, which supported reversible Li^+ storage in the $LiVO_3$ electrode.

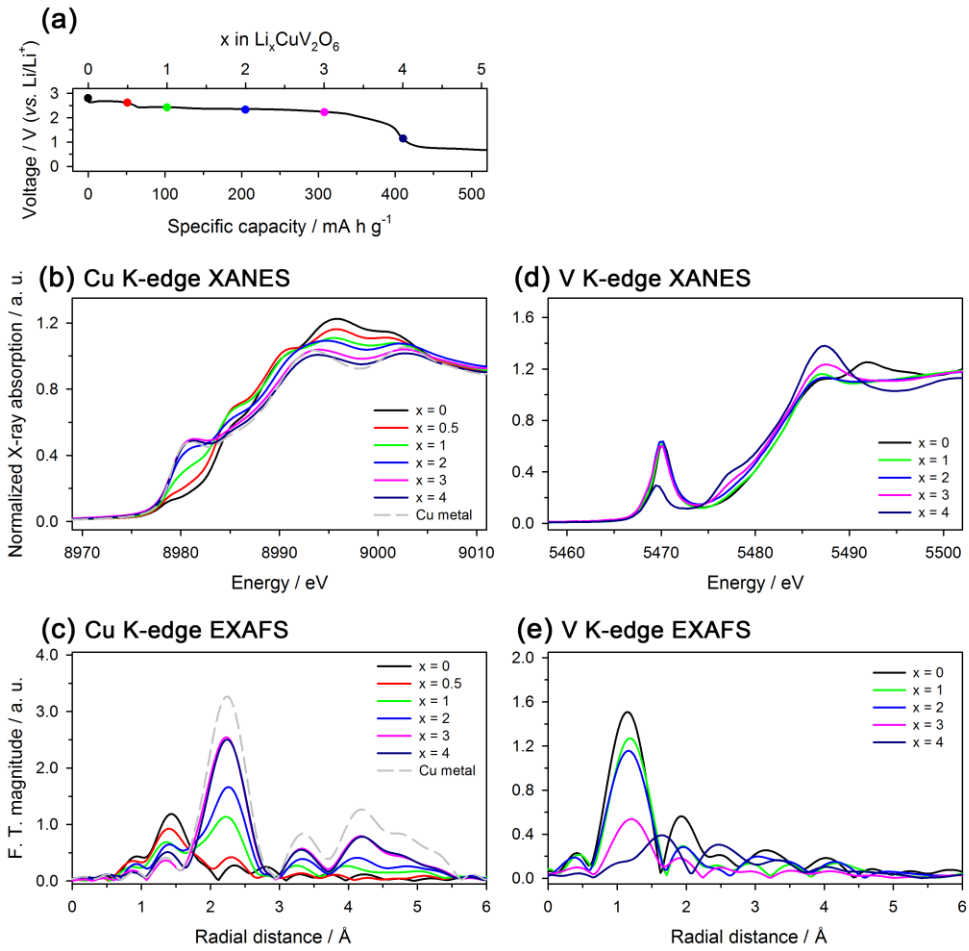

Figure 56. (a); The lithiation/de-lithiation voltage profiles of Li/CuV_2O_6 cell. *Ex-situ* XANES spectra and Fourier transformed EXAFS spectra of (b) and (c); copper K-edge and (d) and (e); vanadium K-edge for CuV_2O_6 electrode, respectively.

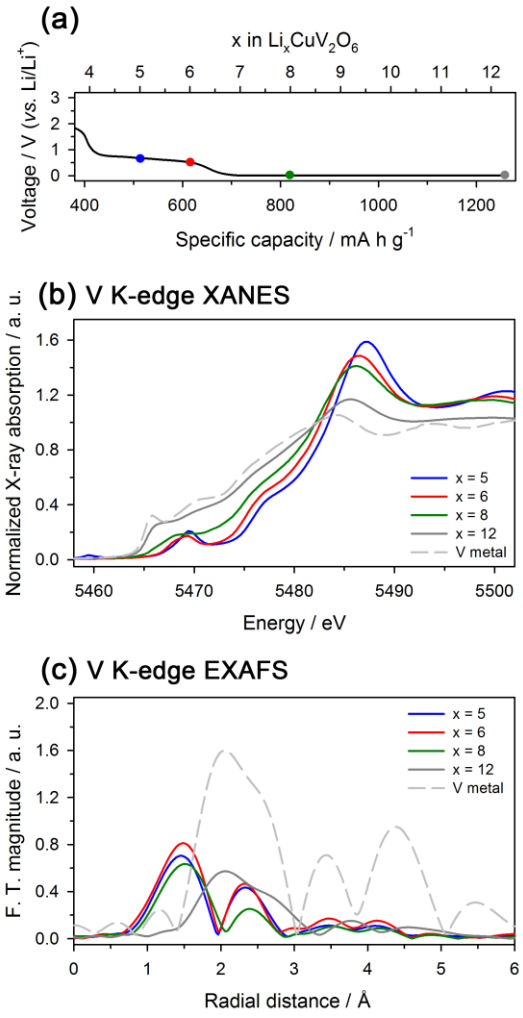

Figure 57. (a); The lithiation/de-lithiation voltage profiles of Li/CuV_2O_6 cell. *Ex-situ* XANES spectra and Fourier transformed EXAFS spectra of (b) and (c); vanadium K-edge for CuV_2O_6 electrode, respectively.

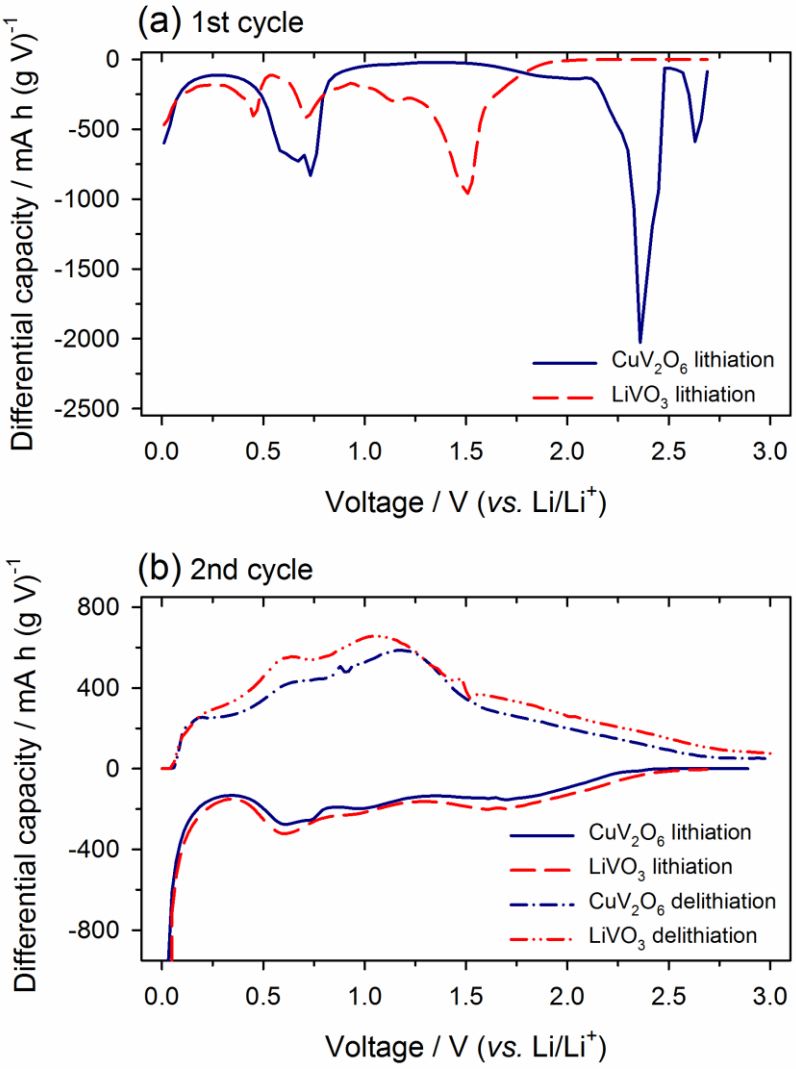

Figure 58. Differential capacity (dQ/dV) plots of Li/CuV_2O_6 and Li/$LiVO_3$ cells (a) at the first cycle and (b) at the second cycle.

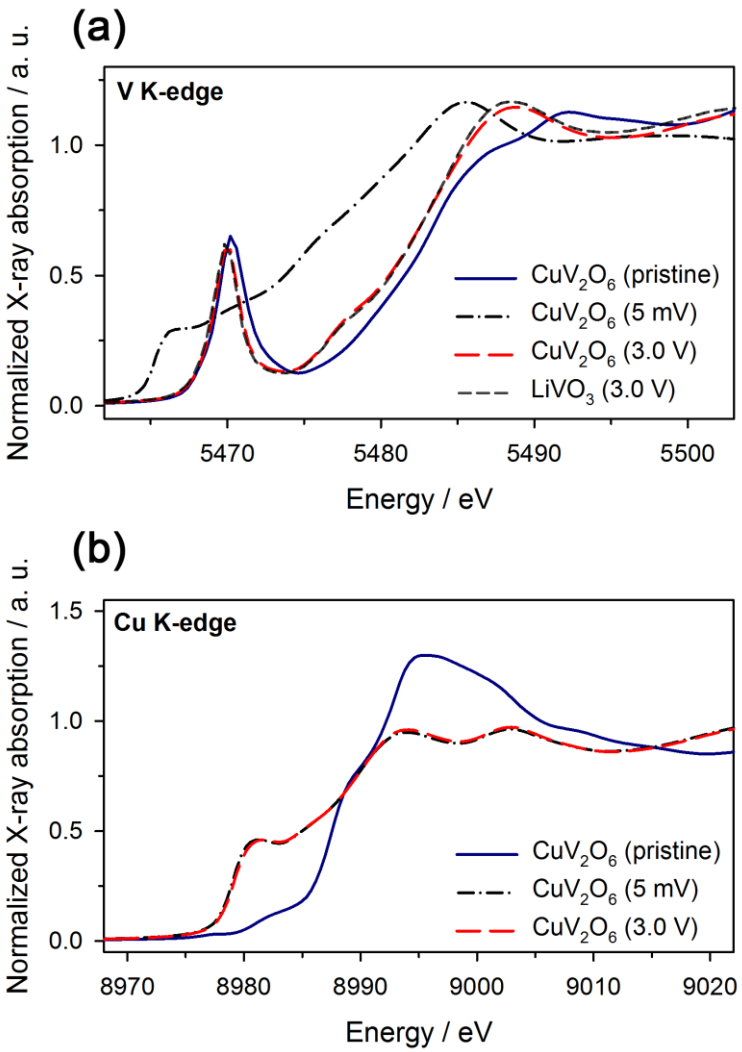

Figure 59. (a) and (b); the V and Cu K-edge X-ray absorption near edge structure (XANES) obtained from the cycled CuV_2O_6 electrodes**;** pristine CuV_2O_6 (blue solid line), fully lithiated state (black dash-dot line) and de-lithiated state (dash line). The grey dash line is obtained from de-lithiated $LiVO_3$.

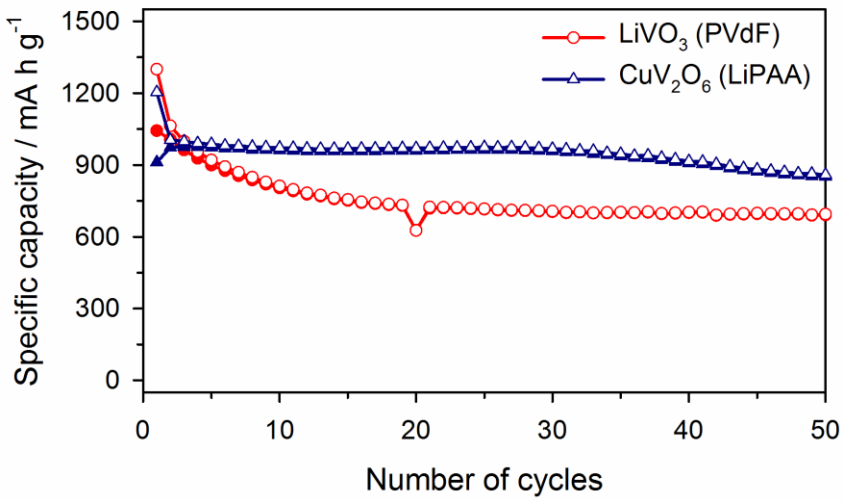

Figure 60. Cycle performance of the Li/CuV_2O_6 (triangle) and Li/$LiVO_3$ (circle) cells.

4.2.6.5. Significant advances of lithium metavanadate ($LiVO_3$)

As presented in Table 4, $LiVO_3$ and CuV_2O_6 present their advanced features over other conversion-type metal oxides in their lower redox potential and large specific capacity. Combined with conventional positive electrodes such as $LiCoO_2$ (LCO) which has a working potential of 3.9 V, the energy density of $LiVO_3$/LCO full cell is two times larger and CuV_2O_6/LCO full cell is 1.7 times larger than that of CoO/LCO full cell as shown in Figure 61.

4.2.7. Summary of Section 4.2.

In Section 4.2, lithium metavanadate ($LiVO_3$) was prepared and its electrode performances including structural change during lithiation was comprehensively examined. Furthermore, the factors that enable the conversion reaction of this material were thoroughly analyzed with electrochemical and computational methods. $LiVO_3$ initially uptakes one Li^+ and electron to transform to Li_2VO_3 becoming a Li-rich layered rock-salt structure (stage A, 1.0 – 3.0 V). Additional Li^+ ions are then inserted into the tetrahedral sites neighboring the Li^+ ions in the vanadium layer (stage B, 0.3 – 1.0 V), inducing the distortion of the Li–V–O structure. At the last lithiation period (stage C, 0.005 – 0.3 V), *ex-situ* XANES and TEM showed that the lithiation proceeds by the conversion reaction, in which the bonds between the vanadium and oxygen are broken to result in the formation of metallic vanadium and the Li_2O matrix. It shows that conversion reaction of vanadium oxides are thermodynamically feasible at room temperature. This unexpected feature accounts for the decrease in the kinetic barrier for the conversion reaction, which is due to the enhanced solid-state diffusion of mobile species in the lithiated $Li_{2+x}VO_3$ structure. A weaker V – O bond strength in the structure compared to that of other lithiated vanadium oxides such as $Li_3V_2O_5$ can also explain the higher conversion

Table 4. The potential range, average working potential and specific capacity of $LiVO_3$, CuV_2O_6 and other conversion-type metal oxides (Co_3O_4, Fe_2O_3 and MnO_2) for negative electrodes.

Materials	Potential range (Avg. working potential) (V vs. Li/Li^+)	Specific capacity (mA h g^{-1})	References
$LiVO_3$	**0.005 – 3.0 V (1.2 V)**	**1043**	**This work**
CuV_2O_6	**0.005 – 3.0 V (1.2 V)**	**911**	**This work**
Co_3O_4	0.01 – 3.0 V (2.0 V)	750	*Electrochim. Acta* **2005**, *50* (18), 3667.
Fe_2O_3	0.5 – 3.0 V (1.7 V)	730	*J. Power Sources* **2005**, *146* (1–2), 315.
MnO_2	0.01 – 3.0 V (1.8 V)	1160	*Electrochem. commun.* **2006**, *8* (3), 383.

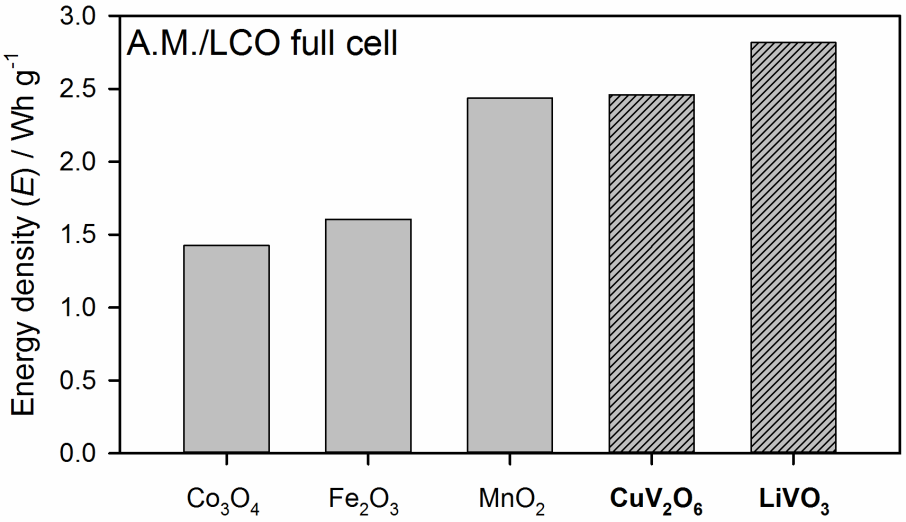

Figure 61. The energy density calculated for the full-cells fabricated with the $LiCoO_2$ (LCO) positive electrode.

reaction activity for $LiVO_3$. Copper vanadate (CuV_2O_6) was also studied in this section as a countermeasure for poor cycle retention of $LiVO_3$ electrodes caused by volume expansion during cycles. Contrasted to $LiVO_3$, CuV_2O_6 is insoluble in water, thus can be fabricated with strong water soluble binders. Moreover, CuV_2O_6 generates $Cu/LiVO_3$ nanocomposites after the first cycle. The generated Cu nanoparticles are inactive afterward and work as a buffer matrix to alleviate volume expansion and provide electronic conductive networks in the electrode to increase the reversibility. Owing to those reasons, the CuV_2O_6 electrode showed increased reversibility over the $LiVO_3$ electrode.

CHAPTER 5. CONCLUSIONS

In this work, novel vanadium-based metal oxides for negative electrode materials were proposed, studied and further improved to increase the energy density of lithium-ion batteries. The significance of research in Part I lies in overcoming the limited specific capacity of insertion-type metal oxides such as lithium titanate ($Li_4Ti_5O_{12}$, LTO) and titanium dioxide (TiO_2) by synergetic effects of atomic scale mixing of vanadium ions with titanium ions in amorphous structure. In Part II, the energy density of the cells adopting conversion-type metal oxides as a negative electrode was enhanced by facilitating conversion reaction of vanadium oxides, which have a lower redox potential compared to other transition metal oxides. The detailed achievements in each parts are as follows:

(i) The newly synthesized amorphous vanadium titanate (*a*VTO) showed reversible specific capacity of 295 mA h g^{-1} at the current density of 100 mA g^{-1}, which is a superior amount of capacity compared to other insertion-type metal oxide electrode materials that operate within the electrochemical stability window of electrolytes (0.8 – 3.0 V). It can be concluded that the extra capacity of the *a*VTO was delivered from its unique structure. As studied with synchrotron X-ray absorption spectroscopy (XAS), it was found that the change in local geometry caused by homogeneous mixing of Ti and V altered the chemical potential of Li storage sites in *a*VTO and further increased the charge (Li^+ and electrons) storage capability. This phenomenon could be explained based on two possibilities; electronic structure (electron accepting ability) and atomic structure (extra Li^+ storage sites).

The other important features of this work are to elucidate the reasons for the irreversible capacity loss of amorphous metal oxides during the first lithiation and to provide appropriate solutions to deal with this problem. One of the most important features that should be satisfied in order for the electrode materials to be applied in the industry is the Coulombic efficiency. Practically, it is important to reduce the irreversible Li^+ consumption on the negative electrodes, which can possibly lead to cell failure in the full cell system. The amorphous vanadium titanate showed enhanced performance not only in Coulombic efficiency but also the rate performance when it was synthesized under nitrogen gas flow, which reduces the population surface hydroxyl groups. This result indicates the necessity of optimizing the surface properties in amorphous materials.

(ii) $LiVO_3$ was prepared and its electrode performances including structural change during lithiation were examined. $LiVO_3$ initially uptakes one Li^+ and electron to transform into Li_2VO_3, a Li-rich layered rock-salt structure. Additional Li^+ ions are then inserted into the tetrahedral sites neighboring the Li^+ ions in the vanadium layer to be $Li_{2.5}VO_3$. Due to the structural distortion in $Li_{2.5}VO_3$, the V–O bonds are easily broken to trigger the conversion reaction to generate metallic V and lithium oxide (Li_2O) with stoichiometric ratio of 1: 3. The stored Li^+ ions reversibly released during delithiation, showing specific capacity over 1,000 mA h g^{-1}. Furthermore, the factors enabling the conversion reaction of this material were quantitatively analyzed with combined electrochemical and computational methods. The comparative studies made on $LiVO_3$ and V_2O_5 revealed that the conversion reaction is thermodynamically more feasible for $LiVO_3$; the quasi-equilibrium potential for conversion reaction is more positive. Moreover, the conversion reaction of this vanadium oxide is kinetically more facilitated compared to V_2O_5. The kinetically favorable features in the former have been identified as the enhanced

solid-state ion diffusion. All these observations explain the occurrence of conversion reaction in $LiVO_3$ but the absence of conversion reaction in V_2O_5 at ambient temperature.

Copper vanadate (CuV_2O_6) was suggested and examined as a way to improve the cycle life of $LiVO_3$ electrode, which suffers from severe volume change during cycles. CuV_2O_6 uptakes two Li^+ and electrons to generate metallic Cu and 10 more Li^+/electrons to reduce V into its elemental state and produce Li_2O. Because of the higher oxidation potential of metallic Cu compared to that of V, V and Li_2O, which were generated with the stoichiometric ratio of 1: 3, is oxidized to form $LiVO_3$ structure and metallic Cu nanoparticles remain inactive during delithiation. There are two advantages of using CuV_2O_6 as an active material for utilizing conversion reaction of vanadium oxides. Unlike $LiVO_3$, which absorbs water from the air (deliquescence) and CuV_2O_6 hardly dissolved in water and thus suits for strongly adhesive water-based binders including polyacrylate lithium salt (LiPAA). Inactive metallic Cu works as a buffer matrix and electron conducting network to improve reversibility of the electrode. As a result, CuV_2O_6 electrode shows increased cycle retention over $LiVO_3$ electrode.

REFERENCES

(1) Cox, P. M.; Betts, R. A.; Jones, C. D.; Spall, S. A.; Totterdell, I. J. *Nature* **2000**, *408* (6809), 184.

(2) Delworth, T. L.; Knutson, T. R. *Science (80-.).* **2000**, *287*, 2246.

(3) Carrasco, J. M.; Franquelo, L. G.; Bialasiewicz, J. T.; Member, S.; Galván, E.; Guisado, R. C. P.; Member, S.; Ángeles, M.; Prats, M.; León, J. I.; Moreno-alfonso, N. *IEEE Trans. Ind. Electron.* **2006**, *53* (4), 1002.

(4) Dunn, B.; Kamath, H.; Tarascon, J.-M. *Science (80-.).* **2011**, *334* (6058), 928.

(5) Tarascon, J.-M.; Armand, M. *Nature* **2001**, *414* (6861), 359.

(6) Park, J.-K. *Principles and Applications of Lithium Secondary Batteries*; John Wiley & Sons, 2012.

(7) Dahn, J.; Zheng, T.; Liu, Y.; Xue, J. *Science (80-.).* **1995**, *270*, 590.

(8) Yazami, R. *Nanomaterials for Lithium-Ion Batteries : Fundamentals and Applications*; 2013.

(9) Winter, M.; Besenhard, J. O.; Spahr, M. E.; Novák, P. *Adv. Mater.* **1998**, *10* (10), 725.

(10) Colbow, K. M.; Dahn, J. R.; Haering, R. R. *J. Power Sources* **1989**, *26*, 397.

(11) Ku, J. H.; Ryu, J. H.; Kim, S. H.; Han, O. H.; Oh, S. M. *Adv. Funct. Mater.* **2012**, *22* (17), 3658.

(12) Poizot, P.; Laruelle, S.; Grugeon, S.; Dupont, L.; Tarascon, J. M. *Nature* **2000**, *407* (6803), 496.

(13) Li, H.; Balaya, P.; Maier, J. *J. Electrochem. Soc.* **2004**, *151* (11), A1878.

(14) Cabana, J.; Monconduit, L.; Larcher, D.; Palacín, M. R. *Adv. Mater.* **2010**, *22* (35), E170.

(15) Scrosati, B. *J. Electrochem. Soc.* **1992**, *139* (10), 2776.

(16) Mizushima, K.; Jones, P. C.; Wiseman, P. J.; Goodenough, J. B. *Mater. Res. Bull.* **1980**, *15*, 783.

(17) Liu, Z.; Yu, A.; Lee, J. Y. *J. Power Sources* **1999**, *81–82*, 416.

(18) Yoshio, M.; Noguchi, H.; Itoh, J. ichi; Okada, M.; Mouri, T. *J. Power Sources* **2000**, *90* (2), 176.

(19) Thackeray, M. M.; Division, C. T.; Program, E. T. *Prog. Solid State Chem.* **1997**, *25* (1–2), 1.

(20) Talyosef, Y.; Markovsky, B.; Salitra, G.; Aurbach, D.; Kim, H. J.; Choi, S. *J. Power Sources* **2005**, *146* (1–2), 664.

(21) Padhi, A. K.; Nanjundaswamy, K. S.; Goodenough, J. B. *J. Electrochem. Soc.* **1997**, *144* (4), 1188.

(22) Fong, R.; Sacken, U. von; Dahn, J. R. *J. Electrochem. Soc.* **1990**, *137* (7), 2009.

(23) Peled, E. *J. Electrochem. Soc.* **1979**, *126* (12), 2047.

(24) Aurbach, D.; Ein-Eli, Y.; Chusid, O.; Carmeli, Y.; Babai, M.; Yamin, H. *J. Electrochem. Soc.* **1994**, *141* (3), 603.

(25) Aurbach, D.; Gamolsky, K.; Markovsky, B.; Gofer, Y.; Schmidt, M.; Heider, U. *Electrochim. Acta* **2002**, *47* (9), 1423.

(26) Choi, N. S.; Yew, K. H.; Lee, K. Y.; Sung, M.; Kim, H.; Kim, S. S. *J. Power Sources* **2006**, *161* (2), 1254.

(27) Kim, H.; Jeong, G.; Kim, Y.-U.; Kim, J.-H.; Park, C.-M.; Sohn, H.-J. *Chem. Soc. Rev.* **2013**, *42* (23), 9011.

(28) Besenhard, J. O.; Fritz, H. P. *Angew. Chemie-International Ed. English* **1983**, *22* (12), 950.

(29) Dahn, J. R.; Sleigh, A. K.; Shi, H.; Reimers, J. N.; Zhong, Q.; Way, B. M. *Electrochim. Acta* **1993**, *38* (9), 1179.

(30) Dey, A. N. *J. Electrochem. Soc.* **1971**, *118* (10), 1547.

(31) Kwon, J. Y.; Ryu, J. H.; Oh, S. M. *Electrochim. Acta* **2010**, *55* (27), 8051.

(32) Bruce, P. G. G.; Scrosati, B.; Tarascon, J.-M. *Angew. Chem. Int. Ed. Engl.* **2008**, *47* (16), 2930.

(33) Chan, C. K.; McIlwrath, K.; Huggins, R. A. *Nat. Nanotechnol.* **2008**, *3* (1), 31.

(34) Kepler, K. D.; Vaughey, J. T.; Thackeray, M. M. *J. Power Sources* **1999**, *81–82*, 383.

(35) Kwon, J. Y.; Ryu, J. H.; Jung, Y. S.; Oh, S. M. *J. Alloys Compd.* **2011**, *509* (28), 7595.

(36) Li, J.; Lewis, R. B.; Dahn, J. R. *Electrochem. Solid-State Lett.* **2007**, *10* (2), A17.

(37) Hochgatterer, N. S.; Schweiger, M. R.; Koller, S.; Raimann, P. R.; Wöhrle, T.; Wurm, C.; Winter, M. *Electrochem. Solid-State Lett.* **2008**, *11* (5), A76.

(38) Ohzuku, T. *J. Electrochem. Soc.* **1995**, *142* (5), 1431.

(39) Inada, R.; Shibukawa, K.; Masada, C.; Nakanishi, Y.; Sakurai, Y. *J. Power Sources* **2014**, *253*, 181.

(40) Ohzuku, T.; Kodama, T.; Hirai, T. *J. Power Sources* **1985**, *14* (1–3), 153.

(41) Kavan, L.; Kratochvilová, K.; Grätzel, M. *J. Electroanal. Chem.* **1995**, *394* (1–2), 93.

(42) Kavan, L.; Grätzel, M.; Rathouskýb, J.; Zukalba, A. *J. Electrochem. Soc.* **1996**, *143* (2), 394.

(43) Lafont, U.; D., C.; Mountjoy, G.; Chadwick, A. V.; Kelder, E. M. *J. Phys. Chem. C* **2010**, *114* (2), 1372.

(44) Kang, Y. M.; Song, M. S.; Kim, J. H.; Kim, H. S.; Park, M. S.; Lee, J. Y.; Liu, H. K.; Dou, S. X. *Electrochim. Acta* **2005**, *50* (18), 3667.

(45) Poizot, P.; Laruelle, S.; Grugeon, S.; Tarascon, J.-M. *J. Electrochem. Soc.* **2002**, *149* (9), A1212.

(46) Speight, J. G. *Lange's Handbook of chemistry*, 16th ed. .; New York : McGraw-Hill: New York, 2005.

(47) Taberna, P. L.; Mitra, S.; Poizot, P.; Simon, P.; Tarascon, J.-M. *Nat. Mater.* **2006**, *5* (7), 567.

(48) Kang, Y.-M.; Kim, K.-T.; Lee, K.-Y.; Lee, S.-J.; Jung, J.-H.; Lee, J.-Y. *J. Electrochem. Soc.* **2003**, *150* (11), A1538.

(49) Morimoto, H.; Tobishima, S. I.; Iizuka, Y. *J. Power Sources* **2005**, *146* (1–2), 315.

(50) Wu, M.-S.; Chiang, P.-C. J. *Electrochem. commun.* **2006**, *8* (3), 383.

(51) Pizzio, L. R. *Mater. Lett.* **2005**, *59* (8–9), 994.

(52) Wagemaker, M.; Borghols, W. J. H.; Van Eck, E. R. H.; Kentgens, A. P. M.; Kearley, G. J.; Mulder, F. M. *Chem. - A Eur. J.* **2007**, *13* (7), 2023.

(53) Chen, J. S.; Lou, X. W. *J. Power Sources* **2010**, *195* (9), 2905.

(54) Park, C. W.; Yoon, S.-H.; Oh, S. M. *Carbon N. Y.* **2000**, *38* (9), 1261.

(55) Xiong, H.; Slater, M. *J. Phys. Chem. Lett.* **2011**, *2*, 2560.

(56) Fang, Y.; Xiao, L.; Qian, J.; Ai, X.; Yang, H.; Cao, Y. *Nano Lett.* **2014**, *14* (6), 3539.

(57) Borghols, W. J. H.; Lützenkirchen-Hecht, D.; Haake, U.; Chan, W.; Lafont, U.; Kelder, E. M.; van Eck, E. R. H.; Kentgens, A. P. M.; Mulder, F. M.; Wagemaker, M. *J. Electrochem. Soc.* **2010**, *157* (5), A582.

(58) Hamaguchi, S.; Yoshitake, H. *Electrochemistry* **2009**, *5*, 373.

(59) Hibino, M.; Abe, K.; Mochizuki, M.; Miyayama, M. *J. Power Sources* **2004**, *126* (1–2), 139.

(60) Delmas, C.; Brethes, S. *J. Power Sources* **1991**, *34*, 113.

(61) Delmas, C.; Cocciantelli, J. M.; Doumerc, J. P. *Solid State Ionics* **1994**, *69*, 257.

(62) Hirashima, H.; Kamimura, S.; Muratake, R.; Yoshida, T. *J. Non. Cryst. Solids* **1988**, *100* (1–3), 394.

(63) Wei, Y.; Zhou, J.; Zheng, J.; Xu, C. *Electrochim. Acta* **2015**, *166*, 277.

(64) Södergren, S.; Siegbahn, H.; Rensmo, H.; Lindström, H.; Hagfeldt, A.; Lindquist, S.-E. *J. Phys. Chem. B* **1997**, *101* (16), 3087.

(65) Tasaki, K.; Goldberg, A.; Lian, J.-J.; Walker, M.; Timmons, A.; Harris, S. J. *J. Electrochem. Soc.* **2009**, *156* (12), A1019.

(66) Ren, Y.; Liu, Z.; Pourpoint, F.; Armstrong, A. R.; Grey, C. P.; Bruce, P. G. *Angew. Chemie - Int. Ed.* **2012**, *51* (9), 2164.

(67) Wu, Q.; Xu, J.; Yang, X.; Lu, F.; He, S.; Yang, J.; Fan, H. J.; Wu, M. *Adv. Energy Mater.* **2014**, *5* (7), 1401756.

(68) Li, W.; Wang, F.; Liu, Y.; Wang, J.; Yang, J.; Zhang, L.; Elzatahry, A. A.; Al-Dahyan, D.; Xia, Y.; Zhao, D. *Nano Lett.* **2015**, *15* (3), 2186.

(69) Wong, J.; Lytle, F.; Messmer, R. *Phys. Rev. B* **1984**, *30* (10), 5596.

(70) Giorgetti, M.; Passerini, S.; Smyrl, W. H.; Mukerjee, S.; Yang, X. Q.; Mcbreen, J. *J. Electrochem. Soc.* **1999**, *146* (7), 2387.

(71) Tsunehiro Tanaka; Yamashita, H.; Tsuchitani, R.; Funabiki, T.; Yoshida, S. *J. Chem. Soc. Faraday Trans.* **1988**, *84* (9), 2987.

(72) Jie, H.; Park, H.; Lee, K.-B.; Chang, H.-J.; Ahn, J.-P.; Park, J.-K. *Surf. Interface Anal.* **2012**, *44*, 1449.

(73) Wu, Z. Y.; Ouvrard, G.; Gressier, P.; Natoli, C. R. *Phys. Rev. B* **1997**, *55* (16), 10382.

(74) Farges, F.; Brown, G.; Rehr, J. *Phys. Rev. B* **1997**, *56* (4), 1809.

(75) Yoshitake, H.; Sugihara, T.; Tatsumi, T. *Phys. Chem. Chem. Phys.* **2003**, *5* (4), 767.

(76) Kawai, H.; Nagata, M.; Kageyama, H.; Tukamoto, H.; West, A. R. *Electrochim. Acta* **1999**, *45* (1–2), 315.

(77) Klosek, S.; Raftery, D. *J. Phys. Chem. B* **2001**, *105*, 2815.

(78) Salek, G.; Bellanger, B.; Mjejri, I.; Gaudon, M.; Rougier, A. *Inorg. Chem.* **2016**, *55* (19), 9838.

(79) Siemensmeyer, B.; Schultze, J. *Surf. Interface Anal.* **1990**, *16*, 1.

(80) Verma, P.; Maire, P.; Novák, P. *Electrochim. Acta* **2010**, *55* (22), 6332.

(81) Dedryvère, R.; Laruelle, S.; Grugeon, S.; Gireaud, L.; Tarascon, J.-M.; Gonbeau, D. *J. Electrochem. Soc.* **2005**, *152* (4), A689.

(82) Swider-Lyons, K. E.; Love, C. T.; Rolison, D. R. *Solid State Ionics* **2002**, *152–153*, 99.

(83) Wang, F.-M.; Rick, J. *Solid State Ionics* **2014**, *268*, 31.

(84) Kim, W. T.; Jeong, Y. U.; Lee, Y. J.; Kim, Y. J.; Song, J. H. *J. Power Sources* **2013**, *244*, 557.

(85) Choi, N.-S.; Kim, J.-S.; Yin, R.-Z.; Kim, S.-S. *Mater. Chem. Phys.* **2009**, *116* (2–3), 603.

(86) Cocciantelli, J. M.; Doumerc, J. P.; Pouchard, M.; Broussely, M.; Labat, J. *J. Power Sources* **1991**, *34* (2), 103.

(87) Chae, O. B.; Kim, J.; Park, I.; Jeong, H.; Ku, J. H.; Ryu, J. H.; Kang, K.; Oh, S. M. *Chem. Mater.* **2014**, *26* (20), 5874.

(88) Song, J. H.; Park, H. J.; Kim, K. J.; Jo, Y. N.; Kim, J.-S.; Jeong, Y. U.; Kim, Y. J. *J. Power Sources* **2010**, *195* (18), 6157.

(89) Eguchi, M.; Iwamoto, T.; Miura, T.; Kishi, T. *Solid State Ionics* **1996**, *89* (1–2), 109.

(90) Cao, X.; Xie, J.; Zhan, H.; Zhou, Y. *Mater. Chem. Phys.* **2006**, *98* (1), 71.

(91) Ma, H.; Zhang, S.; Ji, W.; Tao, Z.; Chen, J. *J. Am. Chem. Soc.* **2008**, *130* (15), 5361.

(92) Débart, A.; Dupont, L.; Poizot, P.; Leriche, J.-B.; Tarascon, J. M. *J. Electrochem. Soc.* **2001**, *148* (11), A1266.

(93) Levi, M. D.; Levi, E. a.; Aurbach, D. *J. Electroanal. Chem.* **1997**, *421* (1–2), 89.

(94) Bard, A. J.; Faulkner, L. R. *ELECTROCHEMICAL METHODS: Fundamentals and applications*; John Wiley & Sons, 2001.

(95) Ku, J. H.; Jung, Y. S.; Lee, K. T.; Kim, C. H.; Oh, S. M. *J. Electrochem. Soc.* **2009**, *156* (8), A688.

(96) Pralong, V.; Gopal, V.; Caignaert, V. *Chem. Mater.* **2012**, *24*, 12.

(97) Boesenberg, U.; Marcus, M. A.; Shukla, A. K.; Yi, T.; McDermott, E.; Teh, P. F.; Srinivasan, M.; Moewes, A.; Cabana, J. *Sci. Rep.* **2014**, *4*, 7133.

(98) B. de. Darent. *National Standard Reference Data Series: National Bureau of Standards No. 31*; National Bureau of Standards, 1970.

(99) Shannon, R.; Calvo, C. *Can. J. Chem.* **1973**, *206* (11), 265.

(100) Strobel, P.; Lambert-Andron, B. *J. Solid State Chem.* **1988**, *75* (1), 90.

(101) Armstrong, A. R.; Lyness, C.; Panchmatia, P. M.; Islam, M. S.; Bruce, P. G. *Nat. Mater.* **2011**, *10* (3), 223.

(102) Park, H.; Yoon, T.; Kim, Y.; Lee, J. G.; Kim, J.; Kim, H.; Ryu, J. H.; Kim, J. J.; Oh, S. M. *J. Electrochem. Soc.* **2015**, *162* (6), A892.

(103) Guo, W.; Chemelewski, W. D.; Mabayoje, O.; Xiao, P.; Zhang, Y.; Mullins, C. B. *J. Phys. Chem. C* **2015**, *119* (49), 27220.

(104) Morcrette, M.; Rozier, P.; Dupont, L.; Mugnier, E.; Sannier, L.; Galy, J.; Tarascon, J.-M. *Nat. Mater.* **2003**, *2* (November), 755.

(105) Li, M.; Yang, X.; Wang, C.; Chen, N.; Hu, F.; Bie, X.; Wei, Y.; Du, F.; Chen, G. *J. Mater. Chem. A* **2015**, *3* (2), 586.

(106) Kepler, K. D.; Vaughey, J. T.; Thackeray, M. M. *Electrochem. Solid State Lett.* **1999**, *2* (7), 307.

(107) Larcher, D.; Beaulieu, L. Y.; MacNeil, D. D.; Dahn, J. R. *J. Electrochem. Soc.* **2000**, *147* (5), 1658.

(108) Lee, K. T.; Jung, Y. S.; Kwon, J. Y.; Kim, J. H.; Oh, S. M. *Chem. Mater.* **2008**, *20* (2), 447.

(109) Jung, Y. S.; Lee, K. T.; Kim, J. H.; Kwon, J. Y.; Oh, S. M. *Adv. Funct. Mater.* **2008**, *18* (19), 3010.

국문초록

리튬 이온 전지용 바나듐계 금속 산화물 전극의 리튬 저장 메커니즘 및 성능 향상

이 정 범

서울대학교 대학원

화학생물공학부

리튬 이온 전지는 현시대에 없어서는 안될 중요한 전기 에너지 저장 장치로서 큰 각광을 받고 있다. 이러한 리튬 이온 전지의 사용처가 점차 다변화 됨에 따라 더욱 향상된 에너지 밀도 또는 높은 출력 특성을 가진 전지의 개발이 진행되고 있다. 기존에 주로 사용되던 흑연계 음극재로는 리튬 이온 전지의 에너지 밀도와 출력 특성을 향상시키기에 어려움이 있기 때문에 새로운 금속 산화물 음극재가 연구되고 있다. 금속 산화물 음극재의 리튬 저장 메커니즘은 삽입반응과 전환반응 두 가지로 분류할 수 있다. 삽입반응의 경우에는 충전 시에 리튬 이온이 정해진 격자 내 공극에 저장되고 방전 시에는 가역적으로 빠져나오기 때문에 반응이 매우 안정적이라는 장점이 있으나, 공극 수의 제한으로 인해 용량이 작다는 단점을 가지고 있다. 반면 전환반응의 경우에는 삽입반응과 달리 리튬 이온이 저장되는 사이트가 정해져 있지 않아 용량이 매우

크다는 장점이 있다. 하지만 리튬 충전 시에 금속과 산소 사이의 결합이 끊어지고 방전 시에 그 결합이 다시 이어져야 하기 때문에 큰 과전압이 발생할 뿐만 아니라, 방전반응이 일어나는 전압이 상대적으로 높기 때문에 양극과 함께 셀을 구성하였을 때 에너지 밀도를 충분히 향상시킬 수 없다는 단점을 가지고 있다.

따라서 본 연구에서는 바나듐 이온을 포함한 금속 산화물을 이용하여 위에 서술한 금속 산화물 음극재의 단점을 개선하였다. 먼저 대표적인 삽입반응 금속 산화물인 티타늄 산화물의 용량을 향상시키기 위해 비정질 구조를 도입하고 바나듐 이온을 추가함으로써 비정질 바나듐 티타네이트 (*a*VTO) 음극재를 합성하여 그 전기화학 특성을 분석하였다. 졸겔법을 통해 합성한 비정질 바나듐 티타네이트는 100 nm 이하의 크기를 가진 일차입자가 뭉쳐져 있는 입자형상을 가지고 있는 것을 확인할 수 있었으며, 0.8 – 3.0 V (*vs.* Li/Li^+) 영역에서 충방전 했을 때 295 mA h g^{-1} 에 해당하는 높은 용량을 발현하였다. 이는 원자단위로 고르게 섞인 티타늄과 바나듐 이온이 비정질상 내에서 새로운 국소구조를 형성함으로써 구조 내에 추가적인 리튬 저장 공간을 형성하고 구조의 전자 구조를 변형시켰기 때문이라 해석할 수 있다. 또한 합성 조건의 최적화를 통해 비정질 바나듐 티타네이트의 표면을 개질함으로써 음극재의 초기 효율 특성과 속도 특성을 보다 개선하였다. 두번째로는 전환반응 금속 산화물의 높은 반응 전압을 보다 낮추기 위해 0.0 V 근처의 낮은 전압에서 전환반응을 통해 리튬을 저장하는 메타바나듐산 리튬염 ($LiVO_3$)을 제안하였다. 음극재로서 처음 제시된 메타바나듐산 리튬염의 리튬 저장 메커니즘을 전기화학, 분광학 실험 및 제일원리계산법을 통해 자세히 분석한 결과 1.5 개의 리튬 이온이 삽입반응으로 저장된 후 3.5 개의 리튬이 전환반응을 통해 메타바나듐산 리튬염 내에 저장된다는 것을 확인하였다. 이는 바나듐 산화물 중에서 처음 보고되는 전환반응으로서 메타바나듐산 리튬염에서 전환반응이 일어나는 원인을 바나듐 오산화물과의 비교를 통해 분석한 결과, 리튬, 바나듐, 산소 이온이 메타바나듐산

리튬염 내부에서 보다 쉽게 이동할 수 있기 때문이라 해석할 수 있다. 또한 충방전 과정 중에 구리 금속 입자와 메타바나듐산 리튬염으로 상변이 하는 메타바나듐산 구리를 적용함으로써 메타바나듐산 리튬염을 활물질로 사용한 전극의 수명 성능을 개선하였다. 이러한 성능 향상은 충방전 과정 중에 생성된 금속 구리 입자가 전극 내에서 메타바나듐산 리튬염의 부피 변화를 완충해 주는 역할을 해줄 뿐 아니라 전극 내 전기전도 특성을 향상시키기 때문이다.

주요어 : 리튬 이온 전지, 음극, 전이금속 산화물, 비정질 바나듐 티타네이트, 메타바나듐산 리튬염, 메타바나듐산 구리

학번 : 2011-22929 **성명** : 이정범